

# AN IMPROVED TURBINE DISK DESIGN TO INCREASE RELIABILITY OF AIRCRAFT JET ENGINES

(NASA-CR-135033) AN IMPROVED TURBINE DISK  
DESIGN TO INCREASE RELIABILITY OF AIRCRAFT  
JET ENGINES (General Electric Co.) 142 p HC  
CSCL 21E

N76-26201

Unclas  
44510 -

G3/07

W.N. Barack and P.A. Domas

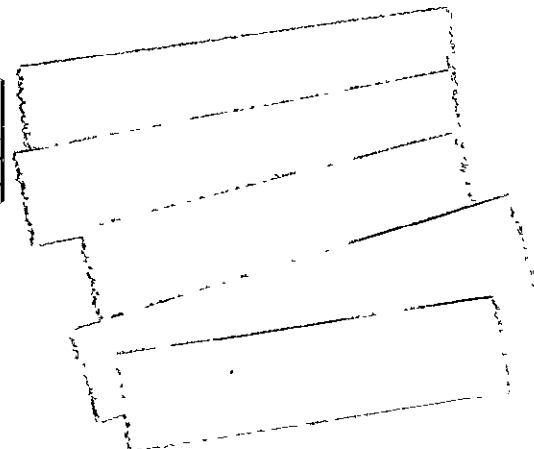
GENERAL ELECTRIC COMPANY

Prepared For

**National Aeronautics and Space Administration**

REPRODUCED BY  
**NATIONAL TECHNICAL  
INFORMATION SERVICE**  
U. S. DEPARTMENT OF COMMERCE  
SPRINGFIELD, VA. 22161

NASA Lewis Research Center  
Contract NAS3-18564



1. Report No. NASA CR-135033		2. Government Accession No.		3. Recipient's Catalog No.	
4. Title and Subtitle AN IMPROVED TURBINE DISK DESIGN TO INCREASE RELIABILITY OF AIRCRAFT JET ENGINES				5. Report Date July 1976	
				6. Performing Organization Code	
7. Author(s) W.N. Barack and P.A. Domas				8. Performing Organization Report No. R76AEG324	
9. Performing Organization Name and Address  General Electric Company Aircraft Engine Group Cincinnati, Ohio 45215				10. Work Unit No.	
				11. Contract or Grant No. NAS3-18564	
				13. Type of Report and Period Covered Contractor Report	
12. Sponsoring Agency Name and Address  National Aeronautics and Space Administration Washington, D.C. 20546				14. Sponsoring Agency Code	
15. Supplementary Notes  Project Manager, Albert Kaufman, NASA-Lewis Research Center, Cleveland, Ohio 44135					
16. Abstract  An analytical study was performed on a novel disk design to replace the existing high-pressure turbine, stage 1 disk on the CF6-50 turbofan engine. Preliminary studies were conducted on seven candidate disk design concepts. An integral multidisk design with bore entry of the turbine blade cooling air was selected as the improved disk design. This disk has the unique feature of being redundant such that if one portion of the disk would fail, the remaining portion would prevent the release of large disk fragments from the turbine system.  Low cycle fatigue lives, initial defect propagation lives, burst speed, and the kinetic energies of probable disk fragment configurations were calculated, and comparisons were made with the existing disk, both in its current material, IN 718, and with the substitution of an advanced alloy, René 95.  The design for redundancy approach which necessitated the addition of approximately 44.5 kg (98 lb) to the design disk substantially improved the life of the disk. The life to crack initiation was increased from 30,000 cycles to more than 100,000 cycles. The cycles to failure from initial defect propagation were increased from 380 cycles to 1564 cycles. Burst speed was increased from 126 percent overspeed to 149 percent overspeed. Additionally, the maximum fragment energies associated with a failure were decreased by an order of magnitude.					
17. Key Words (Suggested by Author(s)) Turbine disk      Flaw propagation Disk life          Disk fragment patterns Low cycle fatigue      Disk burst energies Fracture mechanics      Redundant disks				18. Distribution Statement  Unclassified - Unlimited	
19. Security Classif. (of this report) UNCLASSIFIED		20. Security Classif. (of this page) UNCLASSIFIED			

**PRICES SUBJECT TO CHANGE**

## TABLE OF CONTENTS

<u>Section</u>		<u>Page</u>
I.	INTRODUCTION	1
II.	SUMMARY	2
III.	METHOD OF ANALYSIS	3
	A. Scope	3
	1. Disk Design	3
	2. Disk Life/Failure Analysis	6
	B. CF6-50 Turbofan Engine	6
	1. HPT Stage 1 Disk	8
	2. Blade Cooling Air Entry	9
	3. Flight Cycle	9
	C. Disk Analysis	16
	1. Disk Temperatures	16
	a. Analysis	16
	b. THTD Computer Program	18
	2. Disk Stresses	19
	a. Analysis	19
	b. Computer Program	19
	3. Disk Life	21
	a. Crack Initiation Analysis	24
	b. Crack Propagation	26
	4. Disk Failure	28
	a. Burst Speed Analysis	28
	b. Fragment Energy Analysis	29
IV.	STANDARD DISK	32
	A. Standard Disk Temperature Distribution	32
	B. Standard Disk Stress Distribution	32
	C. Standard Disk Weight	32
	D. Standard Disk Life	32
	1. Low Cycle Fatigue Life	32
	2. Residual Life	48

TABLE OF CONTENTS (Continued)

<u>Section</u>	<u>Page</u>
E. Standard Disk Failure	48
1. Burst Speed	48
2. Fragment Patterns and Energies	48
V. ADVANCED STANDARD DISK	51
A. Advanced Standard Disk Temperature Distribution	51
B. Advanced Standard Disk Stress Distribution	51
C. Advanced Standard Disk Weight	51
D. Advanced Standard Disk Life	51
1. Low Cycle Fatigue Life	63
2. Residual Life	63
E. Advanced Standard Disk Failure	66
1. Burst Speed	66
2. Fragment Patterns and Energies	66
VI. ALTERNATE DISK DESIGN CONCEPTS	67
A. Link Disk	67
B. Laminated Disk	70
C. Multibore Disk	73
D. Composite Disk	75
E. Multidisks	79
1. Bolted Multidisk	79
2. Splined Multidisk	81
3. Integral Multidisk	84
F. Redundant Disk Versus Strengthened Standard Disks	87
VII. DESIGN DISK	89
A. Design Disk Temperature Distribution	89
B. Design Disk Stress Distribution	93
C. Design Disk Weight	93
D. Fail-Safe Capabilities	114

TABLE OF CONTENTS (Concluded)

<u>Section</u>		<u>Page</u>
	E. Design Disk Life	118
	1. Low Cycle Fatigue Life	119
	2. Residual Life	119
	F. Design Disk Failure	123
	1. Burst Speed	123
	2. Fragment Patterns and Energies	123
VIII.	RESULTS AND CONCLUSIONS	129
IX.	RECOMMENDATIONS	130
	REFERENCES	131

## LIST OF ILLUSTRATIONS

<u>Figure</u>		<u>Page</u>
1.	Program Flow Diagram.	4
2.	Flowpath for Detailed Disk Analysis.	5
3.	The General Electric CF6-50 Engine Cross Section.	7
4.	CF6-50 High Pressure Turbine.	10
5.	CF6-50 High Pressure Turbine Stage 1 Disk Detail Design.	11
6.	CF6-50 High Pressure Turbine Stage 1 Disk.	13
7.	CF6-50 High Pressure Turbine Rotor Cross Section Showing Blade Cooling Air Entry.	14
8.	CF6-50 Engine Flight Cycle Showing Six Points of Analysis.	15
9.	Typical Disk ELADI Model and Results.	20
10.	Typical ROTOR Disk Model.	22
11.	Typical ROTOR Stress Concentration Study.	23
12.	Simplified CF6-50 Engine Duty Cycles.	25
13.	Graphical Representation of Residual Cyclic Life Calculation Procedure.	27
14.	Kinetic Energy of a Fragment.	30
15.	CF6-50C HPT Rotor Metal Temperatures at Takeoff 1 Conditions.	33
16.	CF6-50C HPT Rotor Metal Temperatures at Takeoff 2 Conditions.	34
17.	CF6-50C HPT Rotor Metal Temperatures at Maximum Climb Conditions.	35
18.	CF6-50C HPT Rotor Metal Temperatures at Cruise Conditions.	36
19.	CF6-50C HPT Rotor Metal Temperatures at Flight Idle Conditions.	37

LIST OF ILLUSTRATIONS (Continued)

<u>Figure</u>		<u>Page</u>
20.	CF6-50C HPT Rotor Metal Temperatures at Thrust Reverse Conditions.	38
21.	Standard Disk Stress and Deflection Locations.	39
22.	Standard Disk Dovetail Stresses at Takeoff 2 Conditions.	46
23.	Standard Disk Dovetail Loading and Stress Calculation Positions at Takeoff 2 Conditions.	47
24.	Standard Disk Fragment Patterns.	49
25.	Advanced Standard Disk Temperature Distribution at Takeoff 1 Conditions.	53
26.	Advanced Standard Disk Temperature Distribution at Takeoff 2 Conditions.	54
27.	Advanced Standard Disk Temperature Distribution at Maximum Climb Conditions.	55
28.	Advanced Standard Disk Temperature Distribution at Cruise Condition.	56
29.	Advanced Standard Disk Temperature Distribution at Flight Idle Condition.	57
30.	Advanced Standard Disk Temperature Distribution at Thrust Reverse Condition.	58
31.	René 95 and Inco 718 Cyclic Crack Growth Rate Schematic Curves at Maximum Climb Condition.	64
32.	René 95/Inco 718 Crack Propagation Life Ratio Vs. Assumed Initial Defect Size.	65
33.	Link Disk Cross Section in CF6-50 Turbine.	68
34.	Typical Layer of Links for Dovetail Blade Attachment.	69
35.	Laminated Disk.	71
36.	Laminated Disk Normalized Effective Stress Vs. Normalized Weight.	72

LIST OF ILLUSTRATIONS (Continued)

<u>Figure</u>		<u>Page</u>
37.	Multibore Disk.	74
38.	Multibore Transient Stress Distribution.	76
39.	Composite Disk.	77
40.	Composite Disk Material Candidates.	78
41.	Three-Element Bolted Multidisk.	80
42.	Splined Multidisk.	82
43.	Splined Multidisk - Interlocking Spline Concept.	83
44.	Integral Multidisk.	85
45.	Advanced Standard Disk, Bore Stress Variation with Weight.	86
46.	Advanced Standard Disk Critical Crack Size Vs. Bore Stress.	88
47.	Schematic of Failed Design Disk Configuration.	90
48.	Initial Design Disk Configuration - Integral Twin Multidisk.	91
49.	Design Disk Preliminary Stress Distribution.	92
50.	Design Disk Metal Temperatures at Takeoff 1 Conditions.	94
51.	Design Disk Metal Temperatures at Takeoff 2 Conditions.	95
52.	Design Disk Metal Temperatures at Maximum Climb Conditions.	96
53.	Design Disk Metal Temperatures at Cruise Conditions.	97
54.	Design Disk Metal Temperatures at Flight Idle Conditions.	98
55.	Design Disk Metal Temperatures at Thrust Reverse Conditions.	99
56.	Initial Design Disk ROTOR Model.	101

LIST OF ILLUSTRATIONS (Concluded)

<u>Figure</u>		<u>Page</u>
57.	Initial Design Disk Stress and Deflection Locations.	102
58.	Design Disk Final Configuration.	109
59.	Improved (High Rig) Design Disk Stress and Deflection Locations.	111
60.	Blade Cooling Air System Comparison - Bore Entry Vs. Inducer.	115
61.	Design Disk Tangential Stress Distribution in Good Half with One Half Failed.	116
62.	Rib Energy Calculation Methods.	117
63.	Design Disk Critical Locations.	120
64.	Design Disk Critical Locations and Fragment Patterns.	121
65.	Design Disk High Rib Design.	124
66.	Finite Element Model of Rib-Disk Intersection Fillet.	125
67.	Design Disk Fragment Patterns.	127

LIST OF TABLES

<u>Table</u>		<u>Page</u>
I.	CF6-50C Engine Flight Cycle Operating Conditions.	17
II.	Standard Disk Stress and Deflection Distribution at Takeoff 1 Conditions.	40
III.	Standard Disk Stress and Deflection Distribution at Takeoff 2 Conditions.	41
IV.	Standard Disk Stress and Deflection Distribution at Maximum Climb Conditions.	42
V.	Standard Disk Stress and Deflection Distribution at Cruise Conditions.	43
VI.	Standard Disk Stress and Deflection Distribution at Flight Idle Conditions.	44
VII.	Standard Disk Stress and Deflection Distribution at Thrust Reverse Conditions.	45
VIII.	Kinetic Energy Available for Structural Penetration - Standard Disk.	50
IX.	Properties of Candidate Disk Materials.	52
X.	Temperature Comparison: Standard Disk Versus Advanced Standard Disk.	59
XI.	Advanced Standard Disk Stress and Deflection Distribution at Maximum Climb Conditions.	60
XII.	Advanced Standard Disk Stress and Deflection Distribution at Thrust Reverse Conditions.	61
XIII.	Stress Comparison at Maximum Climb Conditions: Standard Disk Versus Advanced Standard Disk.	62
XIV.	Disk Life Comparison - Standard and Advanced Standard Disks.	63
XV.	Kinetic Energy Available for Structural Penetration - Advanced Structural Disk.	66
XVI.	Splined Disk Stress Analysis Results.	81

LIST OF TABLES (Concluded)

<u>Table</u>		<u>Page</u>
XVII.	Temperature Comparison: Standard Disk Versus Advanced Standard Disk Versus Design Disk.	100
XVIII.	Initial Design Disk Stress and Deflection Distribution at Takeoff 1 Conditions.	103
XIX.	Initial Design Disk Stress and Deflection Distribution at Takeoff 2 Conditions.	104
XX.	Initial Design Disk Stress and Deflection Distribution at Maximum Climb Conditions.	105
XXI.	Initial Design Disk Stress and Deflection Distribution at Cruise Conditions.	106
XXII.	Initial Design Disk Stress and Deflection Distribution at Flight Idle Conditions.	107
XXIII.	Initial Design Disk Stress and Deflection Distribution at Thrust Reverse Conditions.	108
XXIV.	Improved (High Rib) Design Disk Stress and Deflection Distribution at Maximum Climb Conditions.	112
XXV.	Improved (High Rib) Design Disk Stress and Deflection Distribution at Thrust Reverse Conditions.	113
XXVI.	Low Cycle Fatigue Comparison.	122
XXVII.	Initial Defect Residual Life Comparison.	122
XXVIII.	Burst Speed Comparison.	122
XXIX.	Fragment Energy Comparison: Standard Disk Versus Advanced Standard Disk Versus Design Disk.	128

## SECTION I

### INTRODUCTION

The purpose of this program was to provide an improved turbine disk design which would increase the reliability of aircraft engines. The primary objective of the program was to make an analytical study of a novel approach in structural disk design which would improve the life of the first-stage high-pressure turbine (HPT) disk of an existing engine used for passenger jet aircraft. The General Electric CF6-50 turbofan engine was used for this study. This engine is currently being used in the McDonnell Douglas DC-10, the Airbus Industrie A-300B, and the Boeing 747-300 aircraft. It is also scheduled for the Air Force Airborne Command Post and the USAF/Boeing AMST transport.

A secondary design objective was to reduce the energy of any fragments which could be produced during a disk failure. An important consideration remaining in focus throughout this study was that the disk design shall have the potential to be economically competitive in mass production as compared to present disk designs.

The technical effort to provide a disk design with improved life and increased reliability consisted of two major tasks. Task I consisted of designing a new disk to replace the existing CF6-50 HPT Stage 1 disk using the novel approach evolved under this program. This novel approach evolved from the consideration of various alternative disk designs, such as laminated or composite disk designs. The new disk was designed using CF6-50 engine conditions, and the design analysis included the effects of transient and steady-state temperatures, blade loading, creep, and low cycle fatigue.

Task II consisted of determining the improvements in life of the newly designed disk, and the standard disk with improved material, over the standard disk for both unflawed and initially flawed conditions. Comparisons were made on the basis of cycles to crack initiation and overspeed capability for an initially unflawed disk, and on the basis of cycles of crack propagation for an initially flawed disk. Also, comparisons were made of the energy content of any possible shed fragments.

## SECTION II

### SUMMARY

An analytical study was performed on a novel disk design to replace the existing high-pressure turbine Stage 1 disk on the CF6-50 engine. Preliminary studies were conducted on seven candidate disk design concepts. An integral multidisk design with bore entry of the blade cooling air was selected as the "Design Disk". This disk has the unique feature of being redundant such that if one portion of the disk would fail, the remaining portion would prevent the release of large disk fragments from the turbine system.

Low cycle fatigue lives, initial defect propagation lives, burst speed, and the kinetic energies of probable disk fragment configurations were calculated, and comparisons were made with the existing disk both in its current material, IN718, and with the substitution of an advanced alloy, René 95.

The design for redundancy approach which necessitated the addition of approximately 44.5 kg (98 lb) to the design disk substantially improved the life of the disk. The life to crack initiation was increased from 30,000 cycles to more than 100,000 cycles. The cycles to failure from initial defect propagation was increased from 380 cycles to 1564 cycles. Burst speed increased from 126 percent overspeed to 149 percent overspeed. Additionally, the maximum fragment energies associated with a failure were decreased by an order of magnitude.

## SECTION III

### METHOD OF ANALYSIS

The General Electric CF6-50 commercial turbofan engine was used in this program to define the flight cycle and the appropriate turbine operating conditions at various cycle points. These environments were then used in the analyses of the various high pressure turbine, Stage 1 disk designs. Standard methods of disk analysis were used throughout.

#### A. Scope

A flow diagram presenting the sequence of events of this program is shown in Figure 1.

##### 1. Disk Design

In the disk design effort performed in Task I, three different turbine disks were examined, as follows:

- Standard Disk - The current CF6-50 HPT Stage 1 disk.
- Advanced Standard Disk - The current CF6-50 HPT Stage 1 disk with the substitution of an advanced disk material, René 95.
- Design Disk - A newly designed CF6-50 HPT Stage 1 disk.

A flow diagram outlining the analysis steps used in the disk design is shown in Figure 2.

The design conditions adhered to in conducting this disk design were the following. The Design Disk would in no way deleteriously affect the engine performance obtained with the Standard Disk. The turbine blade airfoil would not be changed, and the amount of the blade and disk coolants in the present engine would not be increased. The attachment would be changed as required. Provision would be made in the design for channeling coolant to the blades. All material properties used in the disk design would be minus-three-sigma properties, which are the statistical minimum guaranteed property levels for the alloys.

A simplified engine ("duty") cycle was used in the design analysis of these disks. This engine cycle included acceleration and deceleration transients, as well as the climb and cruise conditions of the engine. In the analysis of the three disks, the analytical techniques were carefully scrutinized to ensure that no subtle change in the analysis procedure occurred that would mask the objective results when completed. Detailed design analyses were performed for the Standard and the Design Disks, and the same analytical methods were used to calculate temperatures, stresses, and lives of these disks. Transient and steady-state temperatures in each disk were determined.

IMPROVED TURBINE DISK DESIGN

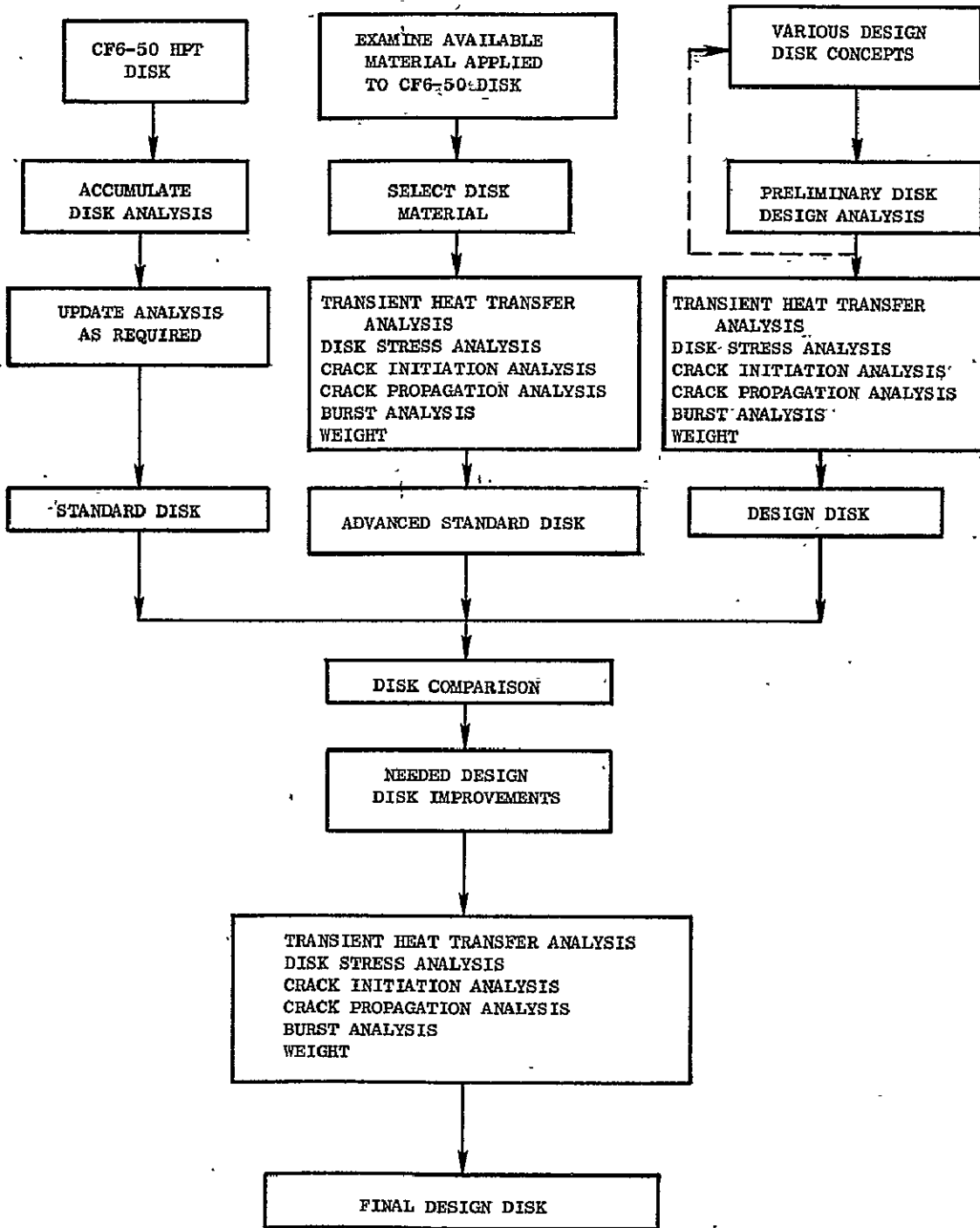


Figure 1. Program Flow Diagram.

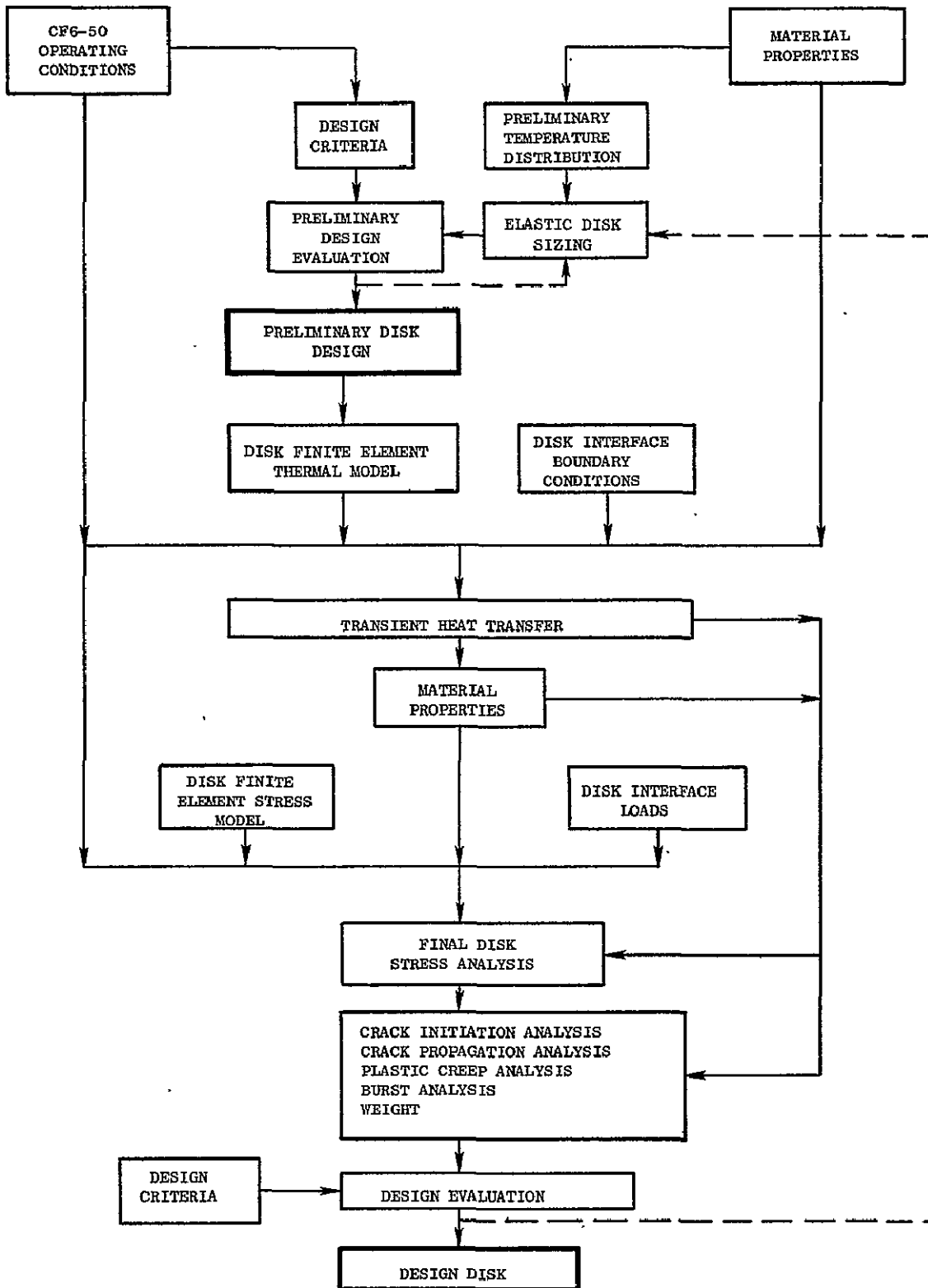


Figure 2. Flowpath for Detailed Disk Analysis.

The stress analysis included the effects of blade loads, blade-to-disk attachments, thermal stresses, elasticity, creep, acceleration and deceleration transients, transfer of loads among redundant elements with slightly varying properties and tolerances, and any other elements with slightly varying properties and tolerances, and any other conditions which were considered in the best current disk design practice.

## 2. Disk Life/Failure Analysis

To assess the relative improvement in disk life over the current design, each of the three disk designs was subjected to extensive failure analyses. These included analysis of crack initiation, crack propagation from an assumed initial defect, burst characteristics, fragmentation patterns, and fragment energies.

Criteria were established to determine the relative merits of the three disk designs with respect to the particular failure mode being investigated:

<u>Mode</u>	<u>Criterion</u>
Initiation	Flight Cycles to Crack Initiation
Initial Defect	Flight Cycles to Failure
Burst	Burst Speed Margin
Fragment Patterns	Number and Size of Fragments
Fragment Energy	Fragment Kinetic Energy Available For Penetration

Using these criteria, the benefits of material changes and basic design concepts employed in the Design Disk were established.

### B. CF6-50 Turbofan Engine

General Electric's CF6-50 commercial turbofan engine is an advanced technology, twin-spool, high-bypass-ratio turbofan (Figure 3) producing in excess of 50,000 pounds of thrust at takeoff. Major engine components include a 14-stage, variable-stator compressor; an annular combustor; a 2-stage, film-cooled, high-pressure turbine which drives the compressor; and a 4-stage, low-pressure turbine which drives the fan and low-pressure compressor. This General Electric-developed, high-bypass turbofan produces a high thrust-to-weight ratio and a 25 percent improvement in fuel economy over earlier generation engines. The CF6 compressor provides very high efficiency with excellent stall margin. Innovations in the combustor design include General Electric's axial swirler enabling CF6's to operate virtually smoke-free. The advanced CF6 turbine cooling system permits high operating temperatures which reduce overall engine size and weight. CF6 engines are quiet due to the low-noise fan design and the sound suppression techniques developed by General Electric.

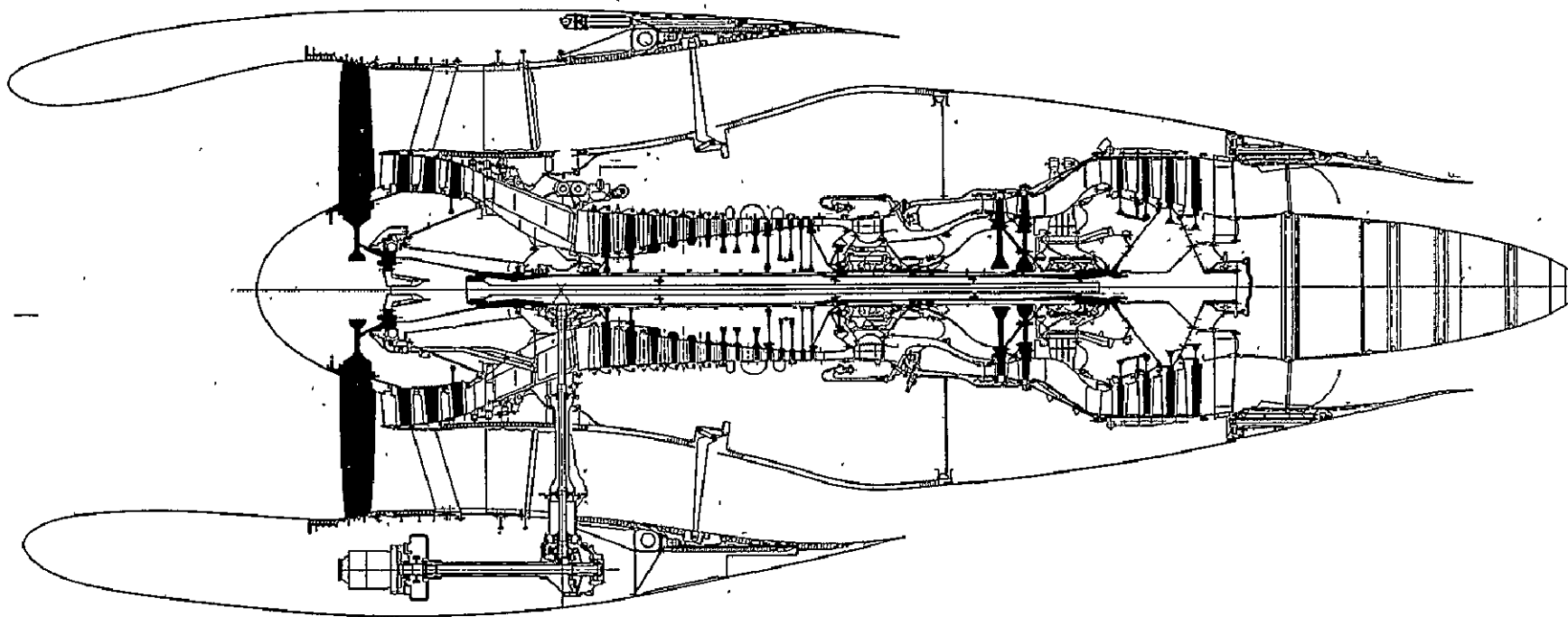


Figure 3. The General Electric CF6-50 Engine Cross Section.

General Electric designed the CF6 to achieve high reliability in commercial airline service. A comprehensive factory test program including many thousands of hours of component tests was carried out on both the CF6-6 and CF6-50 models prior to FAA certification. Further, General Electric maintains a "Fleet Leader" program whereby severe cyclic factory testing is conducted to simulate airline service long before such cycles are encountered in service. The CF6-50 engine has achieved a high level of reliability even in its first years of airline service. Engine reliability rates have been competitive with more mature engines. Operational and maintainability qualities have won the praises of operating airlines. Fuel economy is unequaled by any other aircraft jet or turbofan engine except the CF6-6.

The design philosophy of the CF6-50 builds on the CF6-6 and TF39 programs, where extensive development of the individual components in these engines resulted in production engines that met or exceeded design objectives. The design and configuration of the CF6 engine family are based on obtaining long life, low noise levels, high reliability, and easy access for line maintenance. The engine has the capability of being disassembled by major modules; on-wing borescope and radiographic inspections are also facilitated. These capabilities have proved to be practical and beneficial to CF6 operators.

The highly advanced CF6-50 is the highest thrust turbofan engine in service. With an overall pressure ratio of 30 to 1, it is also the world's highest pressure-ratio turbofan, resulting in rigorous demands on the turbine disk due to high operating levels of compressor discharge temperature, turbine rotor inlet temperature, and engine speed (rpm).

#### 1. HPT Stage 1 Disk

The CF6-50 high-pressure turbine (HPT) is shown in Figure 4. It is a two-stage, moderately loaded, high performance, air-cooled turbine. The Stage 1 disk, selected as the Standard Disk in this study, supports 80 turbine blades by means of individual three-tang dovetail attachments. Torque is transmitted to the compressor by means of a torque cone which is bolted to the forward side of the disk at the rim. The torque from the second stage is transmitted forward to Stage 1 through a thermal shield and cone spacer which also delivers cooling air to the blades and is bolted to the rim of the Stage 1 disk.

The HPT Stage 1 disc, Figures 5 and 6, is produced from a one-piece, integral IN 718 forging. Machining of the disk includes both conventional and nonconventional methods on a highly automated basis. The disk rim incorporates local bosses around the rim bolt holes on both sides to improve the radial load path and increase the low cycle fatigue (LCF) capability of the disk. Cooling air surrounds the dovetail and rim bolts, reducing the effects of temperature on disk life. The cooling air temperature is as high as 1135° F, placing extreme demands on disk quality. The high-temperature cooling air is an inherent result of the high-pressure-ratio cycle essential for good fuel economy.

## 2. Blade Cooling Air Entry

Cooling air for the Stage 1 blades (Figure 7) is drawn from holes in the turbine nozzle support. It is brought through holes in the forward shaft and under the Stage 1 disk bore. The air enters an impeller/spacer cone at the Stage 2 disk inner bolt circle and is pumped to a cavity formed by the Stage 1 disk and the catenary thermal shield between the Stage 1 and Stage 2 disks. Flowing around the local bolt holes on the aft face of the disk, the air enters the dovetail area under the Stage 1 blade and enters the blade through holes in the blade dovetail.

## 3. Flight Cycle

During the lifetime of the CF6-50 engine, it is expected that several different basic flight profiles will be encountered, as well as variations of the same basic profile. The typical flight profile (Figure 8) expected to be encountered in service was developed by study of: (1) airline predictions of projected aircraft usage, (2) actual usage of similar engines in similar aircraft applications, (3) actual ratings of the CF6-50 engine, and (4) statistical analysis of airline practices and power management histories. A typical engine cycle derived from this flight profile was identified, and specific points for design analysis were chosen that include acceleration and deceleration transients as well as the climb and cruise conditions.

In order to best determine which points on the flight profile warranted complete rotor stress analyses, the time history of rotor temperature during the flight cycle and the rotational speed history during the cycle, gained from study of the engine cycle data, were investigated. From this study, six separate flight conditions were identified for complete rotor stress analyses. They are:

1. At a time 11.42 minutes into the flight cycle (Figure 8), when the aircraft is at takeoff power at rotation. This condition was selected because the most significant rotor stress-inducing function, engine speed, is at its maximum.
2. At a time 12.5 minutes into the flight, when the aircraft is about 1600 feet above the runway. This is the last instant of takeoff power. Although the engine speed is not quite as high as the above condition, the metal temperatures are greater because the engine has been at takeoff power longer.
3. At a time 20.5 minutes into the flight, when a typical aircraft is 13,400 feet above the runway during maximum climb. This condition represents the time when the disk rim areas reach their maximum metal temperatures.
4. During steady-state cruise, 58.5 minutes into the flight. This flight condition represents the longest time exposure of the HPT rotor components at any one condition during the entire flight cycle.

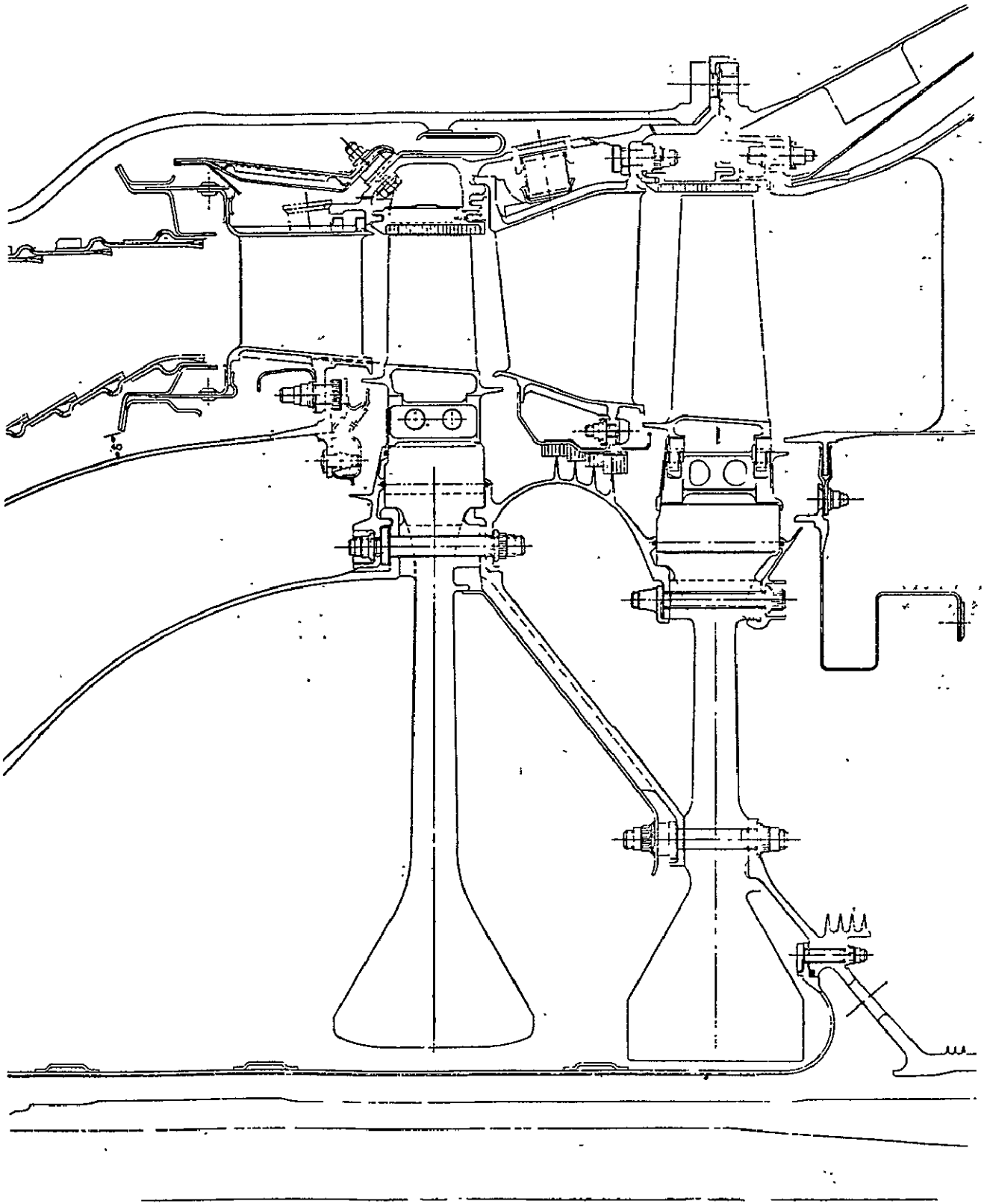


Figure 4. CF6-50 High Pressure Turbine.





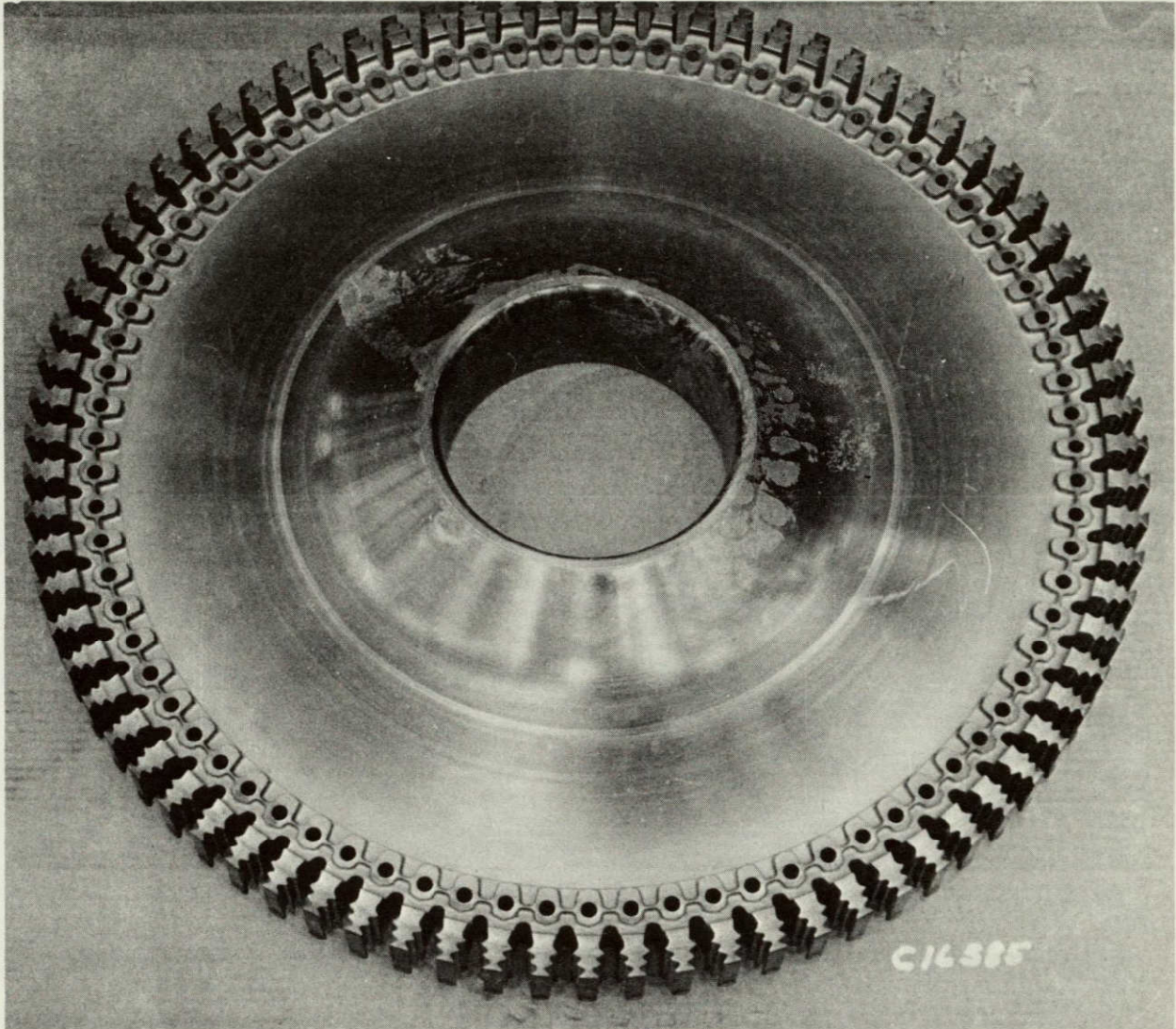


Figure 6. CF6-50 High Pressure Turbine Stage 1 Disk.

ORIGINAL PAGE IS  
OF POOR QUALITY

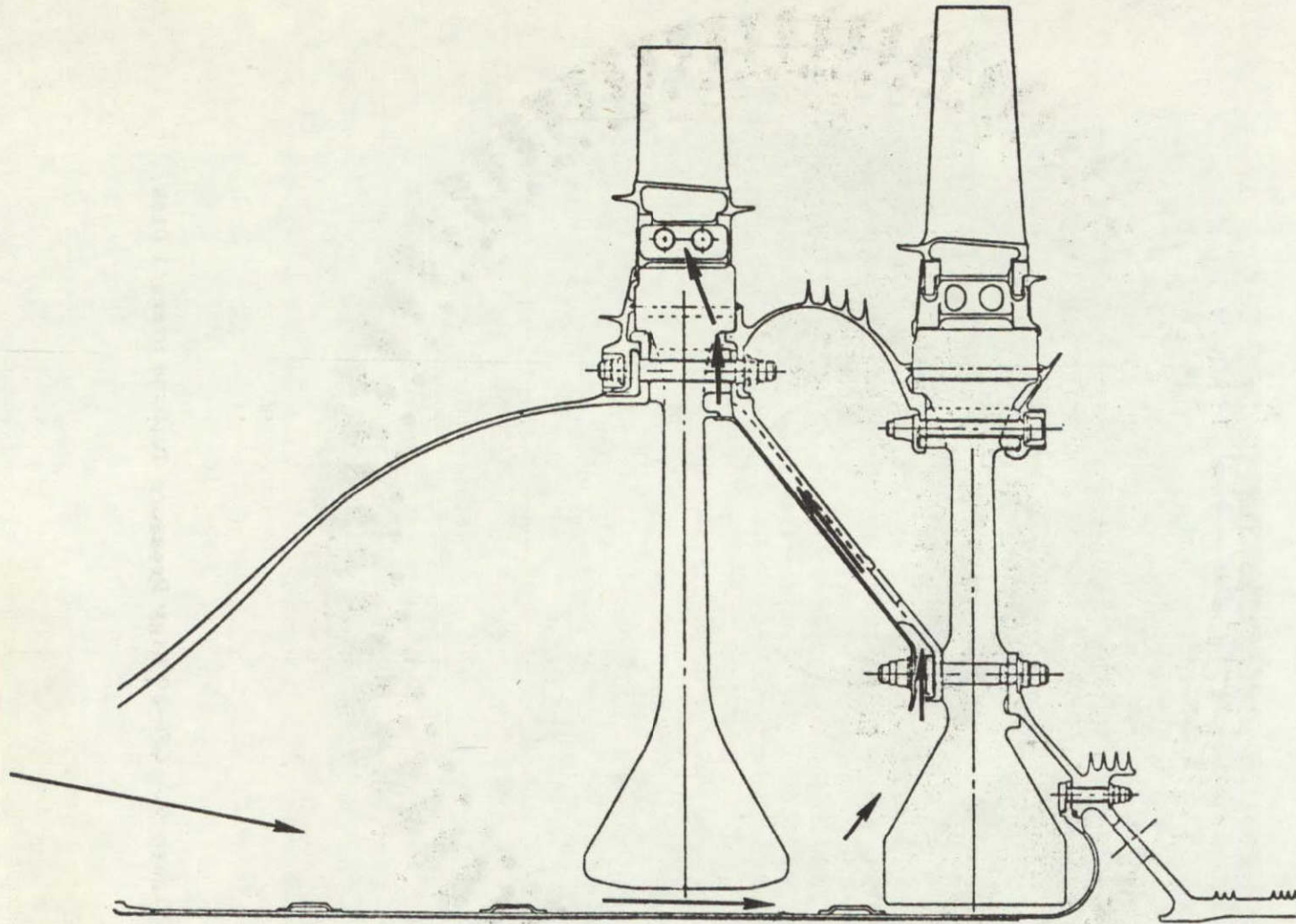


Figure 7. CF6-50 High Pressure Turbine Rotor Cross Section Showing Blade Cooling Air Entry.

(Numbers in Parentheses Indicate Time in Minutes)

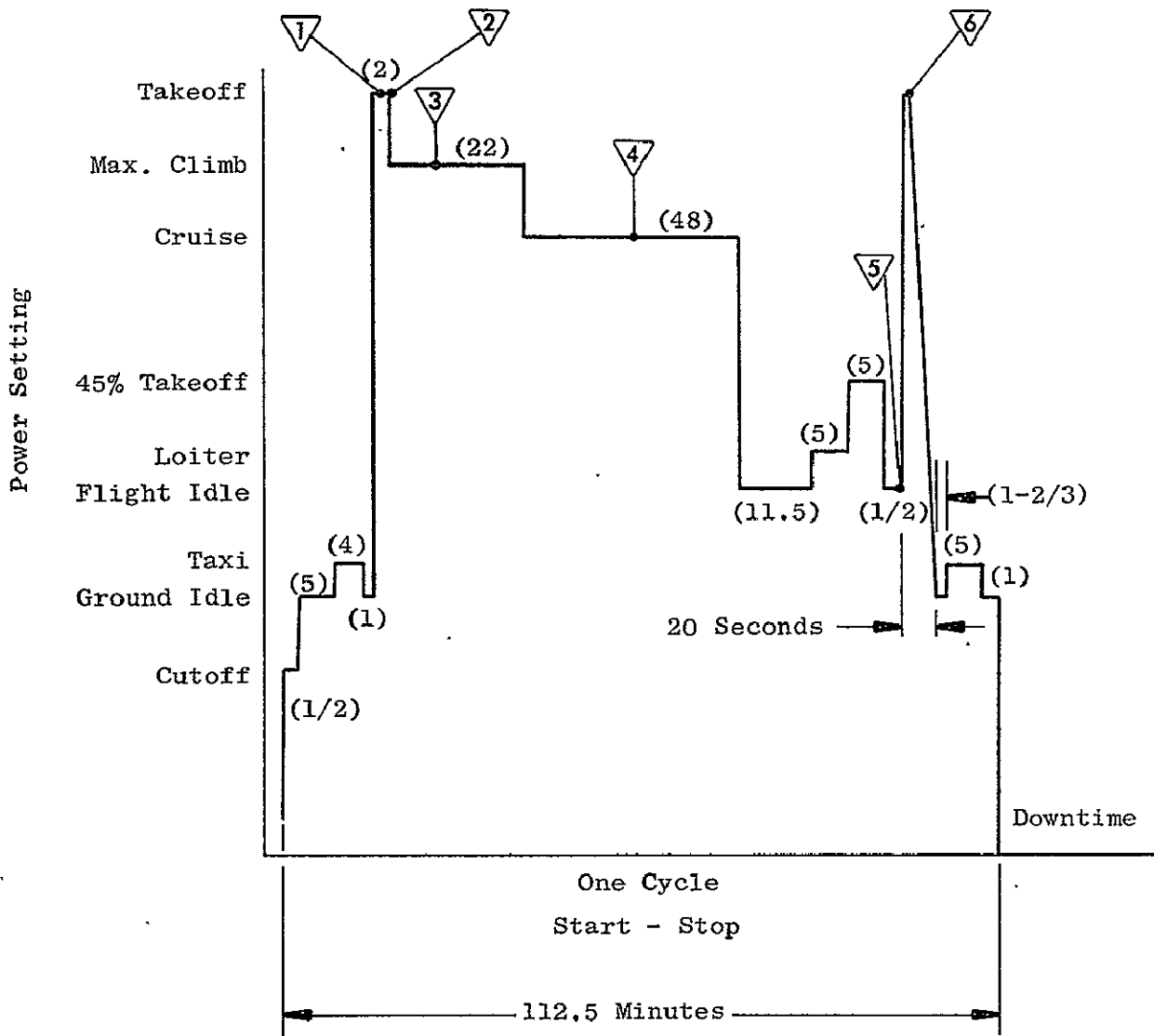


Figure 8. CF6-50 Engine Flight Cycle Showing Six Points of Analysis.

5. At 104.5 minutes from start of flight, at flight idle just prior to the transient to thrust reverse.
6. At 104.58 minutes from start of flight, at the peak of the thrust reverse power excursion. This condition represents the second excursion in the cycle to high rotor speeds, approaching those of takeoff.

The above six conditions henceforth will be referred to as Takeoff 1, Takeoff 2, Maximum Climb, Cruise, Flight Idle, and Thrust Reverse, respectively. The pertinent operating conditions for these six flight conditions are listed in Table I.

### C. Disk Analysis

Standard and thoroughly proven methods of nominal stress calibration were used throughout the disk analyses. The basic stress analysis programs used were General Electric-developed computer programs. Established textbook and handbook references were used to develop most of the concentrations applied to nominal stresses. In cases of complex geometries, the General Electric computer program ROTOR, a finite element program, was used to calculate local stresses and stress concentrations. Both engine test measurements and the General Electric computer program THTD (Transient Heat Transfer) were used to develop HPT rotor transient and steady-state metal temperatures.

#### 1. Disk Temperatures

##### a. Analysis

The disk temperature distributions for the six points of analysis are the result of a combination of analytical and experimental efforts.

The surface temperatures of components of the CF6-50 HPT rotor spool previously had been measured in actual engine operation by metal temperature thermocouples attached directly to the locations where measurements were required, while the engine was operated in both transient and steady-state modes.

The data collected were the metal temperatures as a function of time since establishment of the engine power setting, and the significant engine parameters. The latter were the compressor discharge temperature ( $T_3$ ); the turbine exhaust temperature ( $T_{5.4}$ ), from which the turbine inlet temperature ( $T_4$ ) could be calculated; the compressor discharge pressure ( $P_3$ ); and the HPT rotor speed ( $N_2$ ).

Because of its relatively large mass, the HPT Stage 1 disk metal temperatures could not be predicted directly by simply using the skin thermocouple data from engine test. Instead, the disk was analyzed using the General Electric computer program THTD (Transient Heat Transfer). This program was used to calculate the metal temperatures in the disk interior and surface by matching the skin-node calculated responses and the actual disk measured responses at engine thermocouple locations.

Table I. CF6-50C Engine Flight Cycle Operating Conditions.

Flight Condition	Altitude, Meters (Feet)	Inlet Mach No., $M_0$	Inlet Air Temp., $T_0$ , ° K (° F)	Compressor Discharge Temp., $T_3$ , ° K (° F)	Turbine Inlet Temp., $T_4$ , ° K (° F)	Engine Speed, $N_2$ (rpm)
Takeoff 1	15.2 (50)	0.273	289 (60)	826 (1026)	1516 (2268)	10,143
Takeoff 2	484.6 (1,590)	0.35	286 (55)	826 (1027)	1517 (2270)	10,146
Maximum Climb	4084.3 (13,400)	0.721	272 (30)	822 (1019)	1489 (2221)	10,061
Cruise	1066.8 (35,000)	0.85	220 (-64)	733 (860)	1362 (1991)	9,539
Flight Idle	0	0.377	289 (60)	533 (500)	858 (1084)	7,858
Thrust Reverse	0	0	289 (60)	777 (939)	1407 (2072)	9,753

By using the engine-measured temperature data and the calculated disk responses along with the significant engine parameters, calculations were developed to indicate how rapidly the metal temperatures of many points of the several components of the HPT rotor spool changed during transient accel and decel. These calculations indicated how long it took each of the many points to reach the stabilized temperatures which would be reached if the engine parameters were maintained at the achieved transient power setting, and the shape of the time-temperature curve involved.

The typical flight profile was used, along with these temperature response calculations, to calculate the metal temperatures as a function of time into the flight as the aircraft passed along the flight profile. Thus, in the analysis, the temperatures were calculated at ground idle early in the flight by assuming the rotor spool to have been at ground ambient. By using the ground idle engine parameters  $T_3$ ,  $T_4$ ,  $P_3$ , and  $N_2$ , the final stabilized temperature at ground idle was calculated. For some sections of the rotor, the time required to reach ground idle temperatures was small enough that the parts could reach stabilized temperatures in the flight profile ground idle time. For some parts of the rotor, the stabilization times were too great to reach equilibrium in the ground idle time. Thus, the temperatures had reached only some fraction of their stabilized temperature before the engine power setting was changed to taxi and a new set of engine parameters was forcing the rotor spool metal temperatures to different levels. By using the final temperature achieved at any power setting and adding the temperature achieved incrementally in the succeeding power setting, the time history of the HPT rotor spool was calculated during the typical flight profile.

For especially significant flight conditions, specifically takeoff, climb, and thrust reverse, intermediate power settings were introduced into the calculations within that flight condition to obtain the most accurate temperature history.

#### b. THTD Computer Program

The THTD (Transient Heat Transfer, Version D) program computes transient and steady-state temperature solutions for three-dimensional heat transfer problems. These solutions are obtained by iterative solution of simultaneous algebraic equations for node temperatures derived from finite difference analysis. The use of the implicit form of the heat balance equations permits a direct steady-state solution at any time, including solutions to serve as initial conditions for a transient.

Convergence is recognized when the maximum change in any node temperature is equal to or less than the stipulated tolerance between two successive iterations. An acceleration technique based on a modified method of secants is available to decrease the number of iterations to obtain a solution. The modes of heat transfer include: conduction, convection, mass transport, surface flux, internal generation, gray body radiation, and latent heat for isothermal phase change.

There are options available for computing transient heat transfer coefficients from steady-state values and for internally balancing flow networks.

## 2. Disk Stresses

### a. Analysis

The disk stress analysis was accomplished using a series of General Electric finite element stress analysis programs: SNAP, ELADI, ROTOR, and MULTIHOOK. These are briefly described in the program description section.

Since the shafting that is bolted to the disk is significantly thinner than the disk itself, it will have a faster thermal response. This gives rise to thermally induced load boundary conditions, as the shafting is essentially constrained by the slower disk thermal growths. To define these forces for use as boundary conditions on a disk finite element model, the SNAP program was used. A model of the two-stage turbine system was constructed and analyzed at the six flight cycle points with the appropriate system temperatures and load boundary conditions. The reaction forces at the shaft-disk interfaces were taken from the SNAP results and used as boundary conditions on both ELADI and ROTOR models of the Stage 1 disk.

The disk was first analyzed with ELADI treating the blade loading as a uniformly distributed load. This approach has been used at General Electric for more than 10 years, as the resulting axisymmetric solution yields correct stress levels for most regions of the disk. In certain areas, such as the dovetail slot bottom and the rim area bolt holes, a stress concentration analysis was performed on ROTOR. The model established for the analysis was one of the 80 symmetric pie-shaped sections formed by figuratively cutting up the disk with radial lines at each of the rim bolt hole centers. By comparing the concentrated stresses calculated by ROTOR with the unconcentrated stresses calculated under the same conditions by the ELADI program, the effective stress concentrations were derived for the bolt holes and the dovetail slot bottoms. Disk dovetail stresses were obtained by using the MULTIHOOK program.

### b. Computer Programs

#### ELADI

ELADI calculates the tangential and radial stresses and the radial deflection for a variable-thickness disk. Both uniform circumferential pressure loads at any radial location and radial temperature distributions are allowable boundary conditions. The basic element is a trapezoidal ring that includes the effect of body forces in any given centrifugal force field. These are typically assembled as shown in Figure 9 to form the disk model. Required input items for each element are the element radial coordinate, thickness, temperature, and applied load. Additionally, the material properties and rotational speed of the model are required.

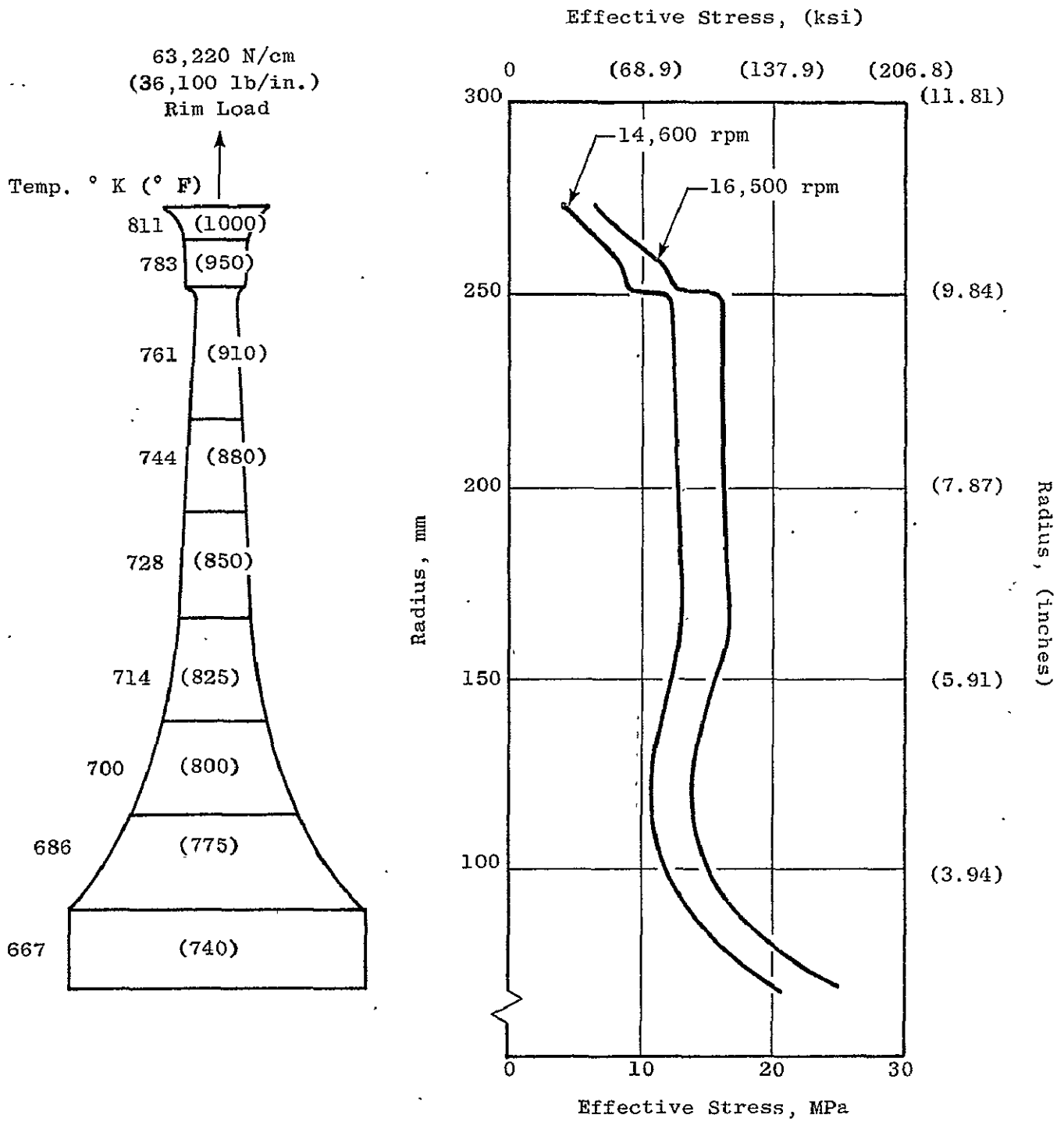


Figure 9. Typical Disk ELADI Model and Results.

## ROTOR

ROTOR is a general purpose, finite element program that is based on the work of Wilson (Reference 1). The basic elements are a constant-stress axisymmetric ring and a constant-stress triangular plate which can be used to analyze either plane stress or axisymmetric structures. In addition, the two types of structures can be used together to simulate an axisymmetric structure with ribs. A typical ROTOR model for a disk is shown in Figure 10. The application of ROTOR to a dovetail slot region in a stress concentration study is depicted in Figure 11. Basic input items include element coordinate definition and connectivity with appropriate temperatures, material constants, and force or deflection boundary conditions.

## SNAP

SNAP (Shell Network Analysis Program) calculates stresses and deflections of shell of revolution structures due to axisymmetric mechanical, pressure, centrifugal, and thermal loads. The structure in question must be modeled into axisymmetrical elements, i.e., cones, cylinders, rings, and disks. A finite element technique is employed, utilizing the automatically computed influence coefficients of these elements. Compatibility and equilibrium conditions are imposed along with the required boundary conditions. The solution yields deflections and rotations at the nodes of the model that in turn can be used to obtain stresses and deflection continuously along each element. Results are given in the form of axial, radial, and rotational deflections and stresses.

## MULTIHOOK

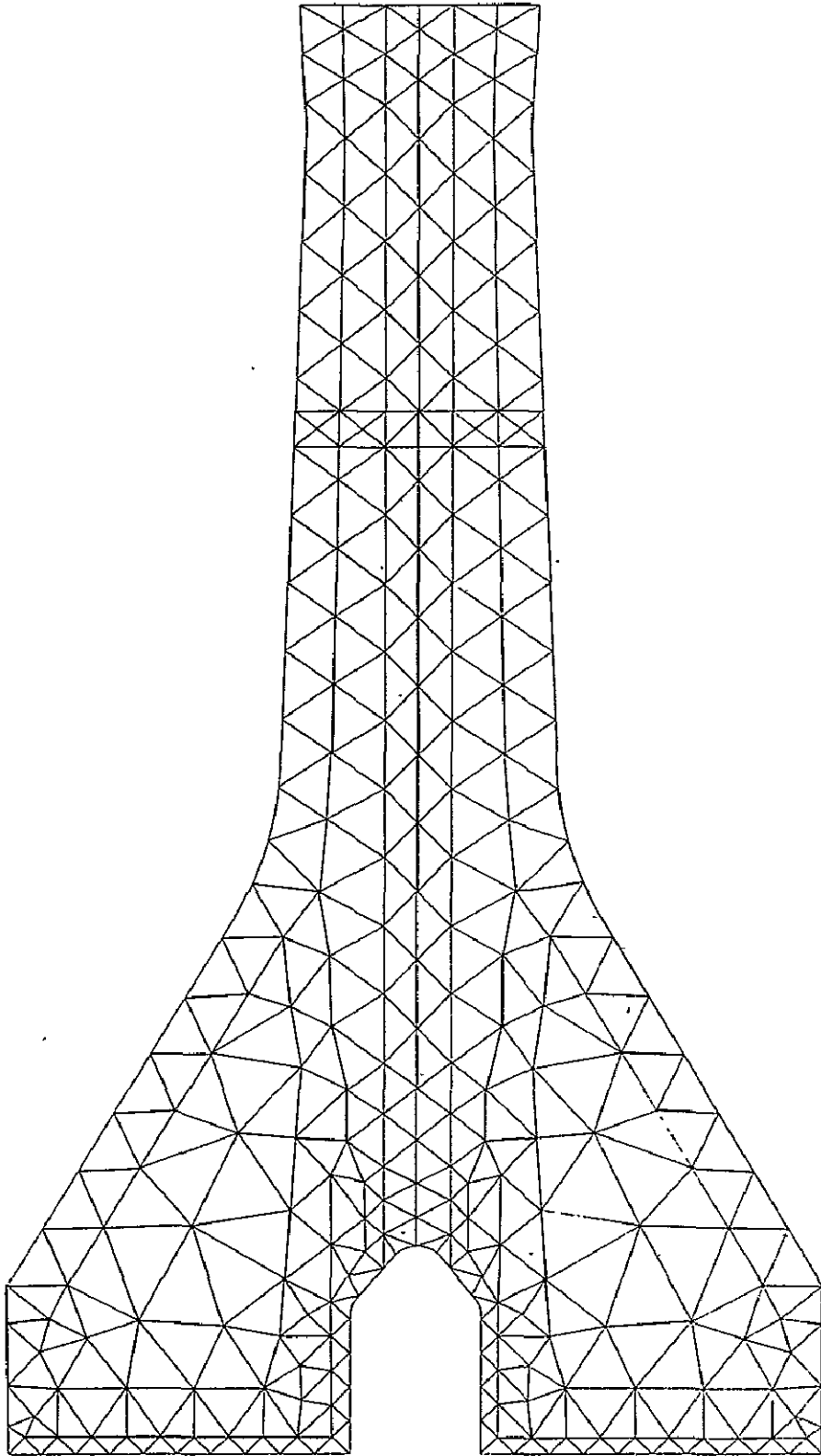
MULTIHOOK is used in performing analytical predictions of both steady and alternating stresses at the critical locations of single and MULTIHOOK blade and disk dovetails. The input items needed are a coordinate definition of the blade and disk dovetail geometries and the applied loading of the blade airfoil and shank of the dovetail cross section. All loads are accounted for simply through the equilibrium of forces and moments in a manner which may be termed consistent with beam theory, i.e., stress distributions across sections and flank load distributions are always taken to be linear.

Extensive experimental verification testing, both photoelastic and mechanical, has been performed confirming the validity of the analysis. This basic dovetail analysis has been successfully applied to a variety of dovetail types including straight single- and multitang dovetails as well as the single-tang circular arc dovetail seen on advanced cooled blade designs.

### 3. Disk Life

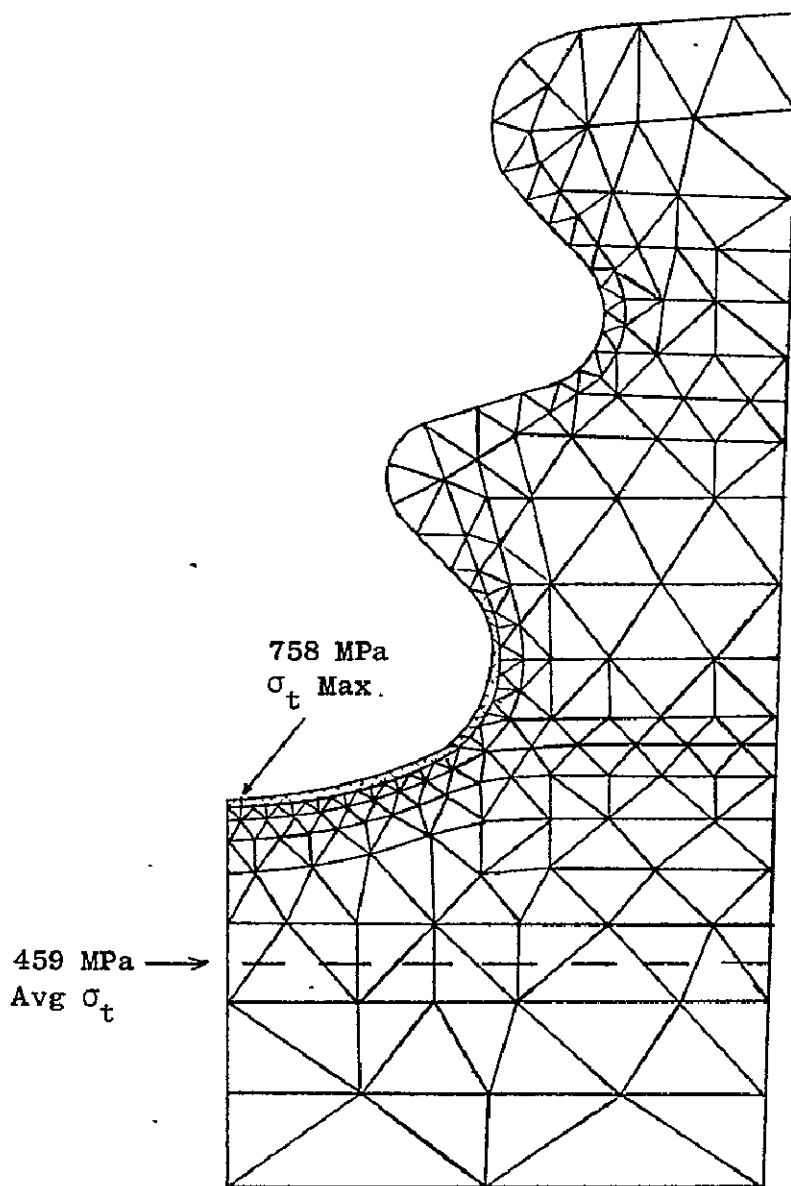
In the analysis of turbine disk life, two distinct and separate modes of life degradation were considered:

1. Initiation of a crack (cycles to crack initiation) which occurs primarily due to stress and temperature cycling conditions on the virgin disk material.



---

Figure 10. Typical ROTOR Disk Model.



$$\text{Effective } K_t = \frac{758}{459} = 1.65$$

Figure 11. Typical ROTOR Stress Concentration Study.

2. Propagation of an initial defect to failure (residual life) which occurs when a defect in the initial metal forging (a rare occurrence) is subjected to the same stress and temperature cycling conditions.

The following definitions were used in this work:

Crack initiation life was defined as the cyclic life available from the initial unflawed surface to initiation of a 0.25 mm x 0.76 mm (0.010 in. x 0.030 in.) crack).

Residual life was defined as the cyclic life from an assumed initial defect of dimensions 2.12 mm x 6.35 mm (0.0833 in. x 0.25 in.) to failure.

The selection of an appropriate initial defect size for the purpose of residual life calculation for this program was difficult. Occasions have been reported where relatively large defects led to premature failures, indicating a sensitivity to such defects. Some examples of large defects in engine components experienced by General Electric include several J85 Stage 1 turbine disks of A286 which contained inclusions in excess of approximately 25.4 mm (one inch) and led to engine shutdown without bursting. A case of a similar size defect occurred in an Astroloy turbine disk where a 25.4 mm (one inch) quench crack led to an engine test cell failure. On still another occasion, an approximately 12.7 mm (half inch) inclusion was present in the dovetail region of a J79 Stage 3 turbine disk but exhibited no growth during routine engine test. In the disk containing this latter inclusion, the observed residual life was greater than that predicted by crack growth analysis based on assuming this inclusion acted as a sharp crack. These cases are cited as examples that such defects can occur, and they highlight the need to maintain the strictest quality control.

Critical area definitions, which may vary among disks due to geometric dissimilarities, were defined for each specific configuration.

#### a. Crack Initiation Analysis

Low cycle fatigue calculations were performed using a simplified engine duty cycle. This was obtained from the "actual" CF6-50 engine flight cycle (Figure 8) by consideration of the severity of the stresses and temperatures. Several approximations of the "actual" cycle are shown in Figure 12 along with stresses pertaining to the bore of the CF6-50 HPT Stage 1 disk. In Figure 12(a), the small perturbations in stress have been ignored. A further reduction in cycle complexity is afforded by Figure 12(b) where the flight idle stress is taken as zero and the takeoff, climb, and cruise portions of the cycle are compared (as simple cycles) to ascertain which portion is most damaging. Temperatures used in these analyses are the maximum steady-state values for the hold time portions and the maximum transient values for the non-hold time portions. This is conservative since lower temperatures and stresses exist throughout much of the holdtime period. The final simplified duty cycle was thus determined to be that shown in Figure 12(c), consisting of a climb portion of 22 minutes duration plus a thrust reverse portion.

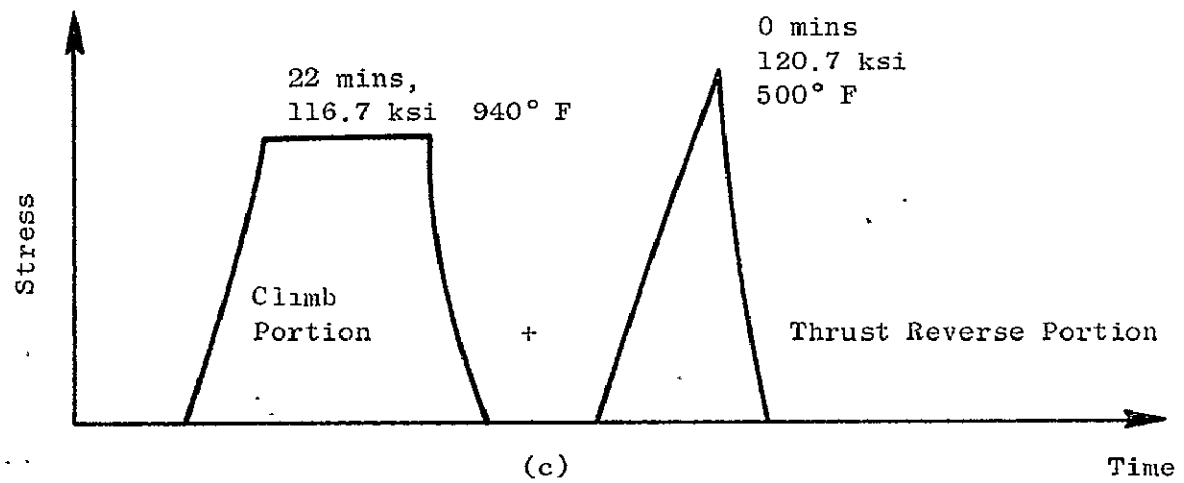
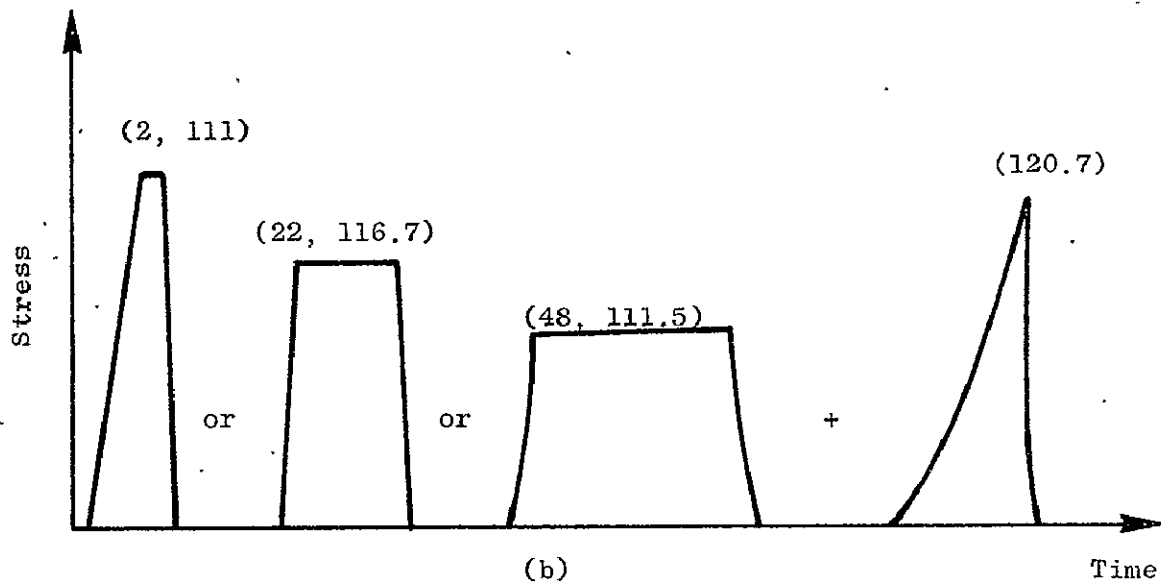
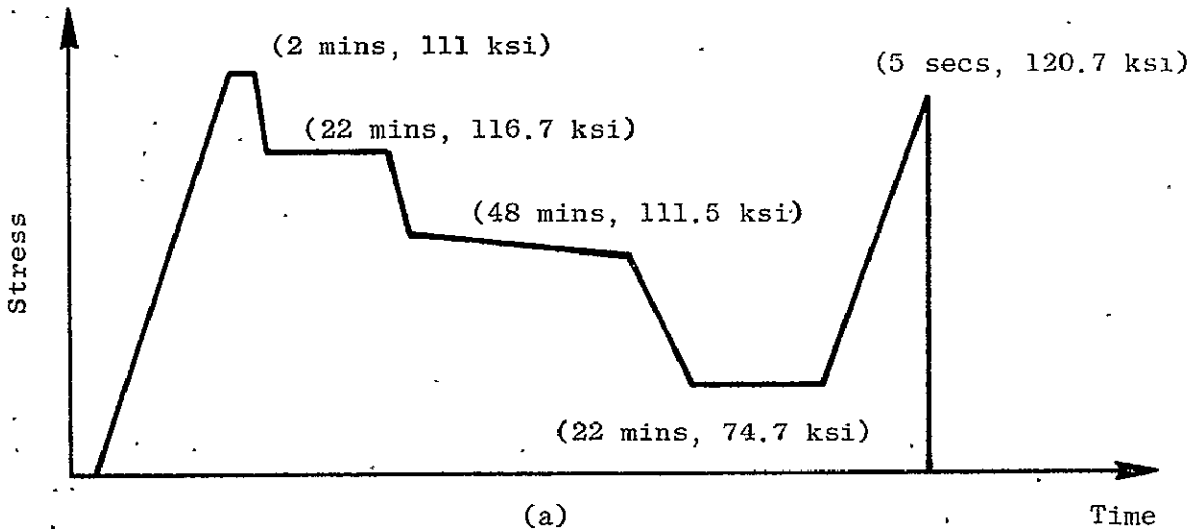


Figure 12. Simplified CF6-50 Engine Duty Cycles.

For each critical disk location, particular stress and temperature values were obtained for these cycles using Standard Day conditions. Biaxial stress effects were assumed to be small so that uniaxial data was generally used.

Laboratory specimen data were used to determine hardware life expectancy. Identification of the appropriate fatigue property curve is dependent on the critical area being analyzed, since local material response may be constant-strain or constant-load amplitude, subject to stress magnitude, component geometry, hold time, and temperature. The bore region ( $K_t = 1.0$ ) was considered as stress controlled while all other critical areas were taken as strain controlled.

For each critical area, LCF lives for the cruise portion and thrust reverse portion of the cycle were obtained. These were -3 $\delta$  minimum values from appropriate data curves corresponding to the particular stress, temperature, and cycling mode present. These lives were then combined using Miner's Linear Cumulative Damage rule (Reference 2).

#### b. Crack Propagation Analysis

The number of cycles to failure from an initial defect (residual life) was calculated for each disk using a fracture mechanics approach. An initial, crack-like defect was assumed in several critical (high stress and temperature) regions. As stated earlier in this section, the use of the large initial defect size of 2.12 mm x 6.35 mm (0.0833 in. x 0.25 in.) was based on documented failure analyses which tend to identify relatively large size defects as failure sources.

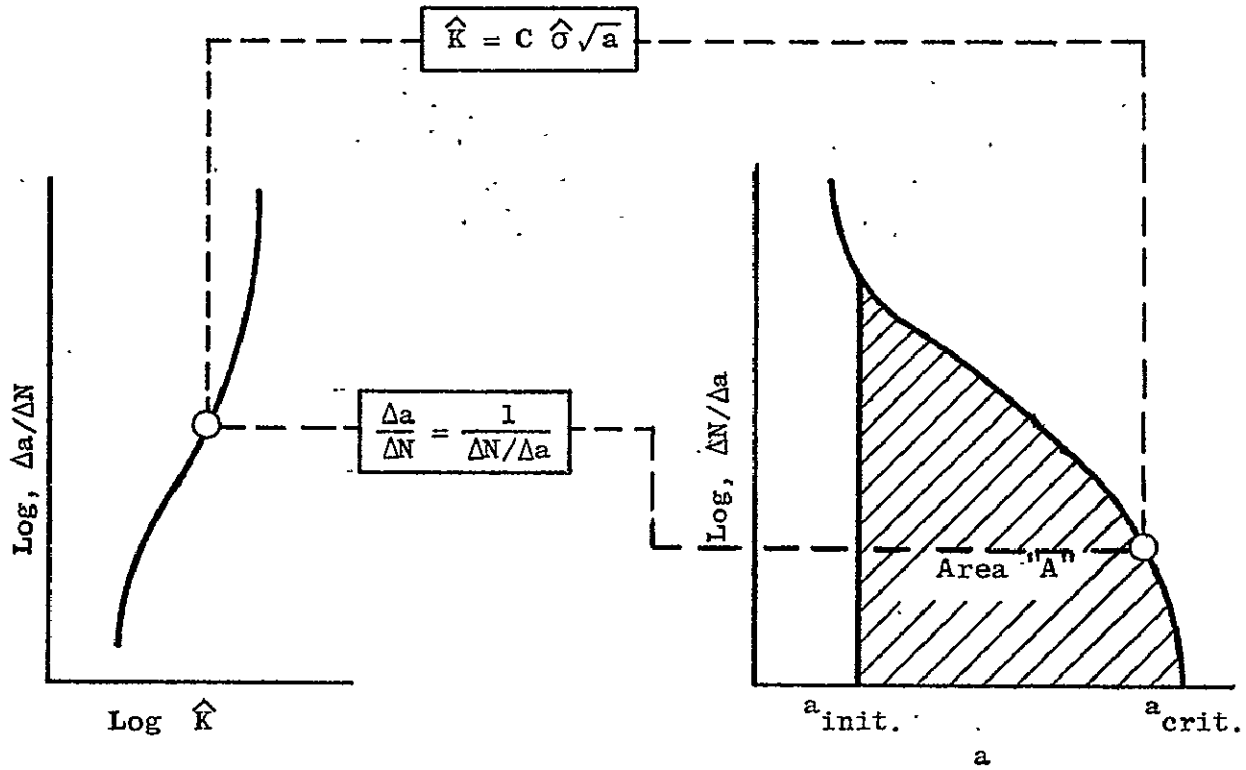
The chosen defect size served the following purposes:

1. Demonstrated fracture mechanics techniques used to predict component lives with assumed initial defects.
2. Provided a viable means of comparison between the calculated propagation lives for the Standard, Advanced Standard, and Design Disks.

The use of this size defect was conservative. Greater life improvements would be realized with the use of smaller defects, as will be shown later.

Using the chosen defect size in the critical areas, the propagation lives of initial defects were calculated. This was done using the time-sharing program SETCRACK which was developed by General Electric. SETCRACK calculates propagation lives by employing standard equations for stress intensity parameters and a sigmoidal curve representation of crack growth rate versus stress intensity. This is illustrated in Figure 13. The stress field near the crack determines the stress intensity as a function of crack length. The sigmoidal equation is numerically integrated from the initial defect size to the final size where the critical stress intensity is exceeded, or the ultimate stress

- a = Crack Length
- $\hat{K}$  = Stress Intensity Factor Range
- C = Constant
- $\hat{\sigma}$  = Stress Range
- N = Cycles
- $N_R$  = Residual Life



$$A = \int_{a_{init.}}^{a_{crit.}} (\Delta N / \Delta a) da = N_R$$

Figure 13. Graphical Representation of Residual Cyclic Life Calculation Procedure.

is achieved. A residual life was calculated for each of the two component cycles, i.e., the climb and thrust reverse cycles defined in the preceding section. The two results were then combined using Miner's rule to yield the residual life in terms of flight cycles.

#### 4. Disk Failure

##### a. Burst Speed Analysis

The burst speed of the disks was determined using a modified "Hallinan" criterion. The Hallinan equation is:

$$N_b = 0.95N \left[ S \left( \sqrt{\frac{\sigma_u}{\sigma_{T \text{ avg}}}} - \sqrt{\frac{\sigma_u}{\sigma_{T \text{ max}}}} \right) + \sqrt{\frac{\sigma_u}{\sigma_{T \text{ max}}}} \right] \quad (1)$$

where

- N = Speed at which stresses are determined
- $\sigma_u$  = Ultimate strength of disk material at room temperature
- $\sigma_{T \text{ avg}}$  = Average tangential disk stress at N rpm
- $\sigma_{T \text{ max}}$  = Maximum tangential disk stress at N rpm
- S = Empirical constant determined for the ratio of nominal ultimate tensile strength to the notched bar ultimate tensile strength, (1/NSR)
- NSR = Notch strength ratio
- $N_b$  = Burst speed (rpm)

Modifications to the above equation account for the true disk stress state through the use of the Von Mises-Hencky effective stress. Material ductility effects are also included. These modifications have been thoroughly substantiated by extensive disk testing. (Details of these modifications, which were developed under another program, are proprietary to General Electric and thus are not presented here.)

Overspeed capability was defined as the burst speed of a disk under spin pit conditions (room temperature). The stress values used in the above equation were, therefore, mechanical stresses at N rpm; thermal effects (which are small) have been deleted.

Minus-three-sigma values of  $\sigma_u$ , and NSR, were used for conservatism.

## b. Fragment Energy Analysis

The energies associated with various fragments were calculated based on the following principle assumptions:

1. Failure occurs at the maximum hot day takeoff speed of 10,613 rpm.
2. Fragmentation into the various patterns occurs instantaneously.
3. The energy expended in fragmentation is small relative to the total energy and is ignored.
4. The fragments do not interact with each other after failure.
5. Blade and post energy is completely translational.
6. Fragments consisting of several blades and an associated rim segment travel as a single piece.

The total disk kinetic energy is first determined by using an elemental breakdown and the approximate relation:

$$KE_{\text{disk}} = \omega^2 \sum_i m_i r_i^2 \quad (2)$$

where

$\omega$  = angular velocity

$m_i$  = mass of particular element

$r_i$  = centroidal radius of particular element

To this is added the blade kinetic energy:

$$KE_{\text{total}} = KE_{\text{disk}} + KE_{\text{blades}}$$

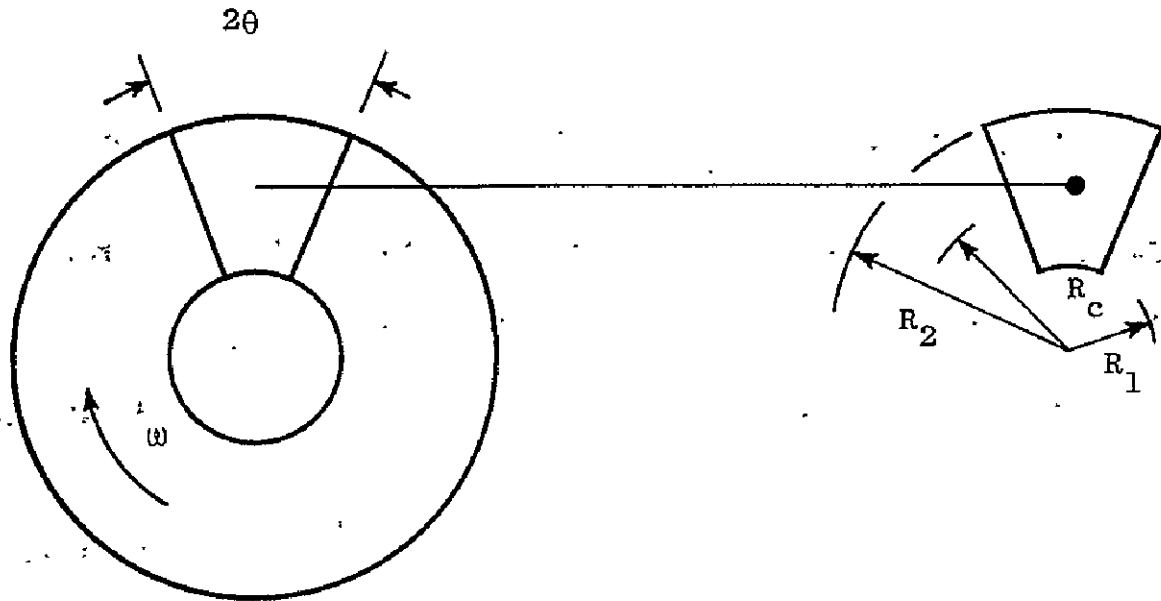
Next the translational kinetic energy of a disk segment is determined as illustrated in Figure 14. The rotational energy is then

$$KE_{\text{rot}} = KE_{\text{total}} - KE_{\text{trans}} \quad (3)$$

This determines the energy state for large disk fragments containing integral blades and posts.

For assumed fragments consisting of only blades or posts or other small pieces, the relation

$$KE = 1/2 MU^2 = 1/2 M(R\omega)^2 \quad (4)$$



$$KE_{\text{Trans}} = 1/2 M_f (V_{\text{Trans}})^2 = 1/2 M_f (\bar{R}_c \omega)^2$$

$$M_f = \rho \theta t (R_2^2 - R_1^2)$$

$$KE_{\text{Trans}} = 1/2 \sum \left[ \frac{\rho \theta t}{g} (R_2^2 - R_1^2) \right] \left[ 4/3 \frac{\sin \theta}{2\theta} \left( \frac{R_2^3 - R_1^3}{R_2^2 - R_1^2} \right) \right]^2 \omega^2$$

Where

$KE_{\text{Trans}}$  = Translational Kinetic Energy

$V_{\text{Trans}}$  = Translational Velocity

RC = Centroidal Radius

$\rho$  = Density

t = Thickness

g = Gravitational Constant

Figure 14. Kinetic Energy of a Fragment.

is used where:

$M$  = fragment mass

$R$  = fragment centroidal radius

Fragment patterns were determined by considering past experience with failed disks. The large fragment patterns have been observed in spin pit burst tests. The number of post and blade pieces for the small patterns was assumed based on test cell experience where two CF6 dovetail post failures were recorded. In these failures, a crack resulted in loss of a dovetail post and two blades as the primary failure. Additionally, two more posts and two more blades were lost as secondary failures. One might expect a "domino" effect due to continuous load transfer from post to post that would result in subsequent loss of all blades and posts. This effect is apparently counter-balanced, however, by the rapid ejection of the blades.

This pattern of three posts and four blades was assumed to be a viable pattern which might result from assumed affects in the vicinity of the dovetail posts in the CF6-50 engine. .

## SECTION IV

### STANDARD DISK

#### A. Standard Disk Temperature Distribution

The Standard Disk temperature distributions are shown in Figures 15 through 20 for the six flight cycle points defined for analysis. As previously discussed in Section III B, these temperatures are based on a correlation between analytical predictions and experimental engine test results.

#### B. Standard Disk Stress Distribution

To calculate the disk stress and deflection distributions, the ELADI and ROTOR finite element computer programs were used. Figure 21 defines the locations at which stresses and deflections are reported for the standard disk. The results were taken from the appropriate ELADI runs and are listed in Tables II through VII.

The dovetail stresses (Figure 22) were obtained using the MULTIHOOK computer program and are effective stresses. The applied loadings (Figure 23) used in the program are those calculated for the blade at its root cross section during Takeoff 2 conditions. In MULTIHOOK, all loads are accounted for through the equilibrium of forces and moments in a manner that is consistent with beam theory, i.e., stress distributions across sections and flank load distributions are always taken to be linear.

#### C. Standard Disk Weight

In addition to calculating stresses and deflections, both the ELADI and ROTOR finite element programs calculate the weight of the model being analyzed. By combining the calculated weight of the disk and the dovetail actual weight, the total weight of the Standard Disk was determined to be 67.2 kg (148 lb).

#### D. Standard Disk Life

##### 1. Low Cycle Fatigue Life

From consideration of high stress and high temperature combinations at several locations in the Standard Disk, four critical life areas were determined:

- Dovetail slot bottom
- Bolt holes

Standard Day

Temperatures in  $^{\circ}$  K ( $^{\circ}$  F)

ORIGINAL PAGE IS  
OF POOR QUALITY

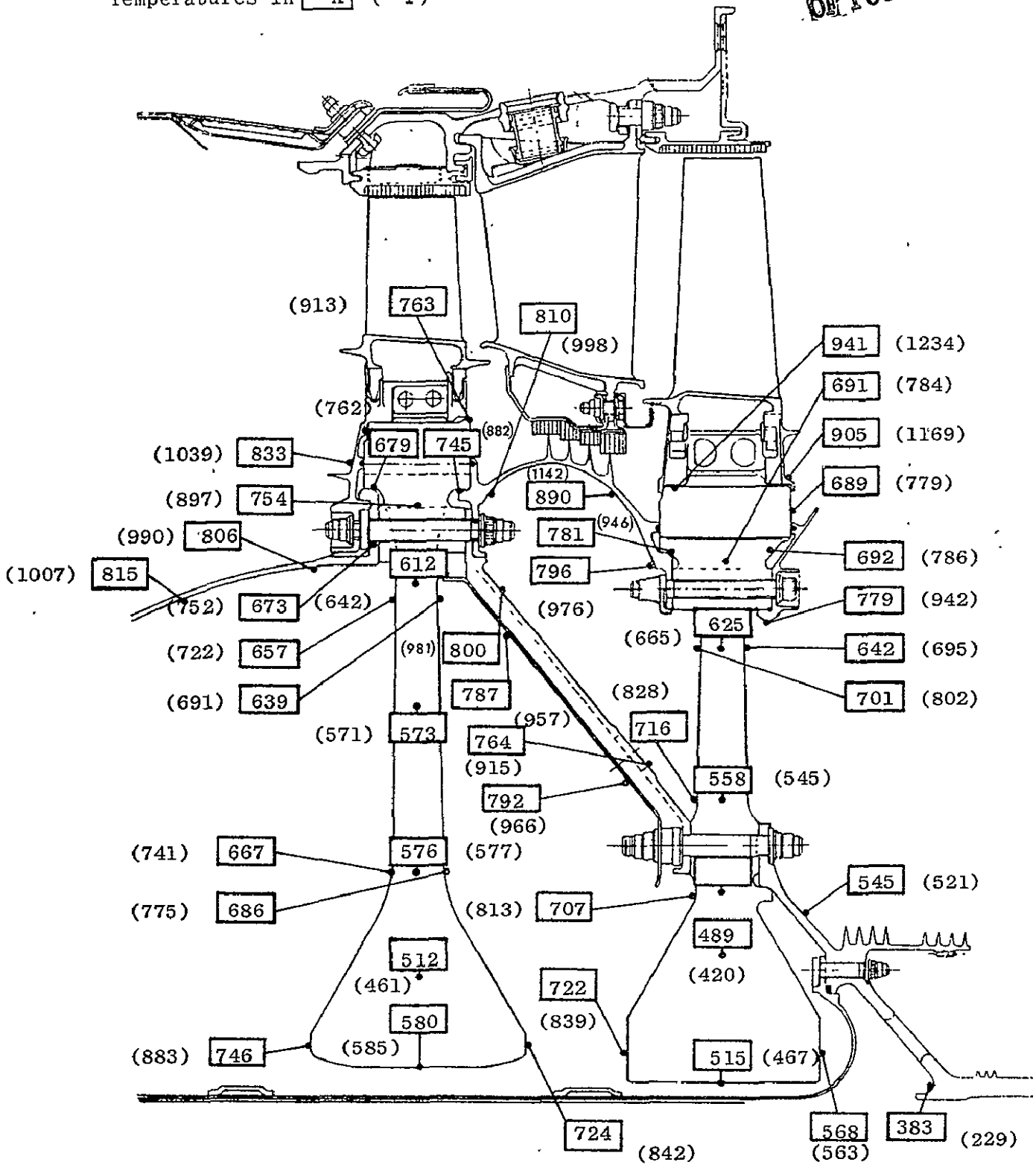


Figure 15. CF6-50C HPT Rotor Metal Temperatures at Takeoff 1 Conditions.

Standard Day

Temperatures in  $^{\circ}$  K ( $^{\circ}$  F)

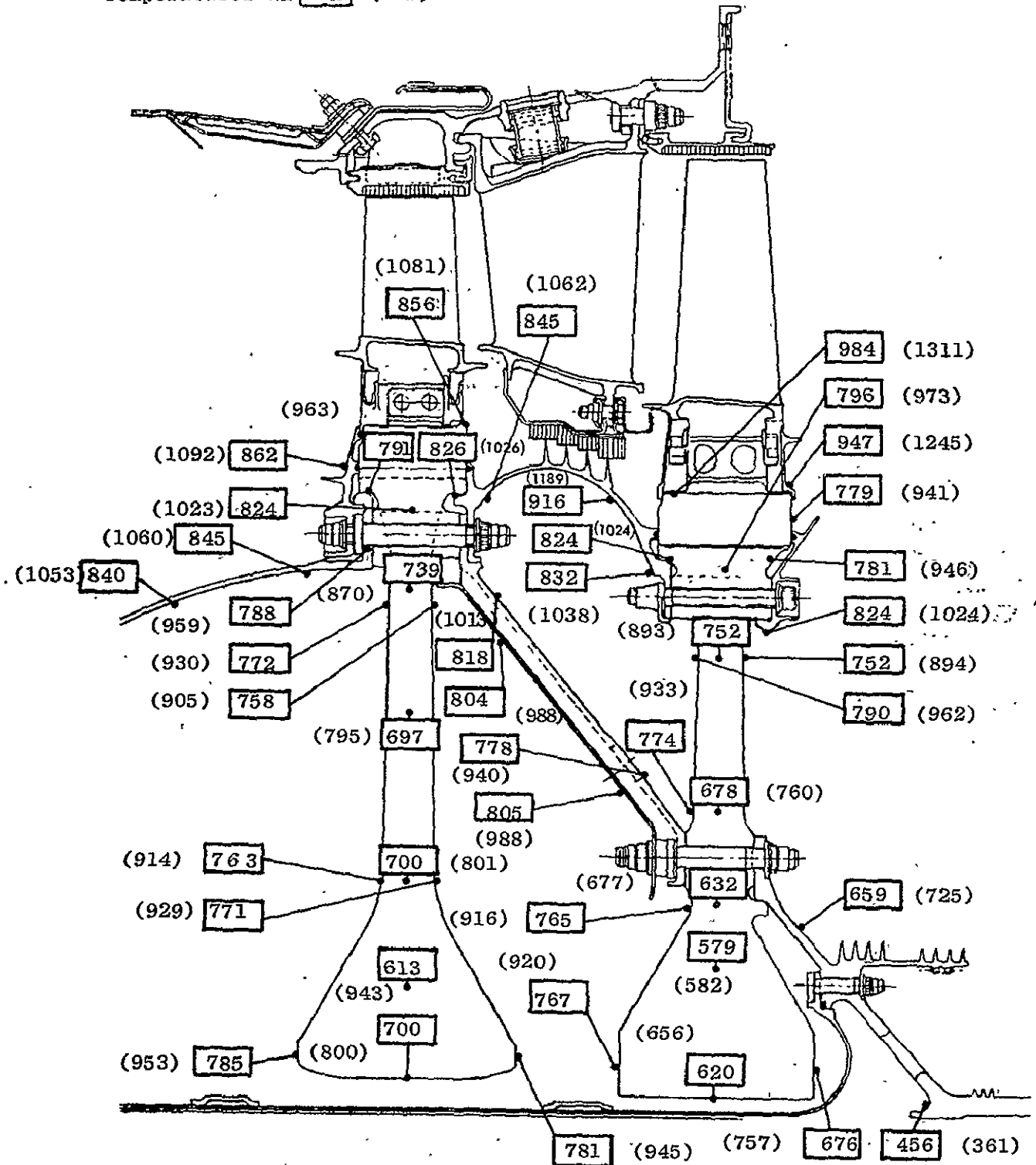


Figure 16. CF6-50C HPT Rotor Metal Temperatures at Takeoff 2 Conditions.

Standard Day

Temperatures in  $^{\circ}$  K. ( $^{\circ}$  F)

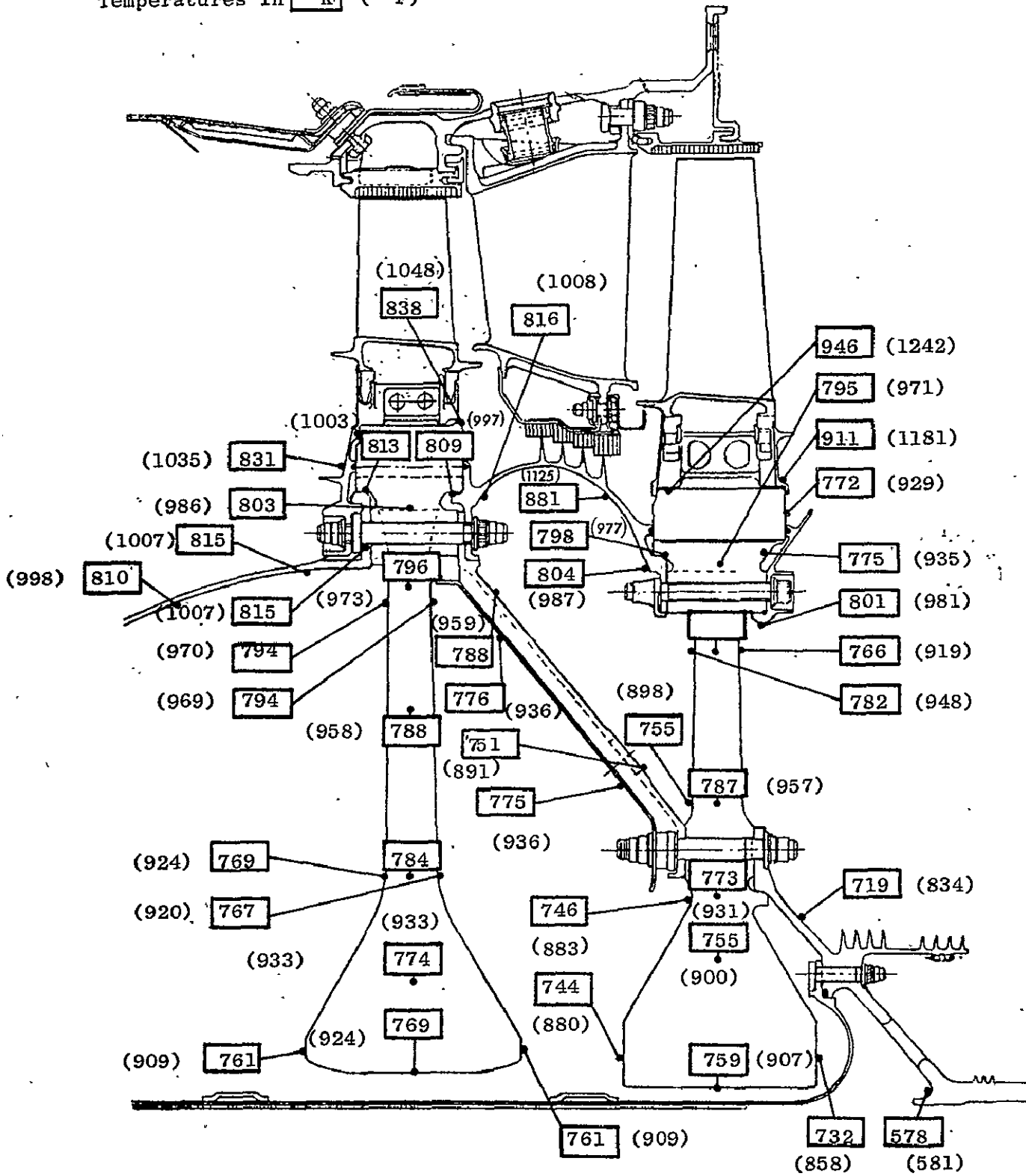
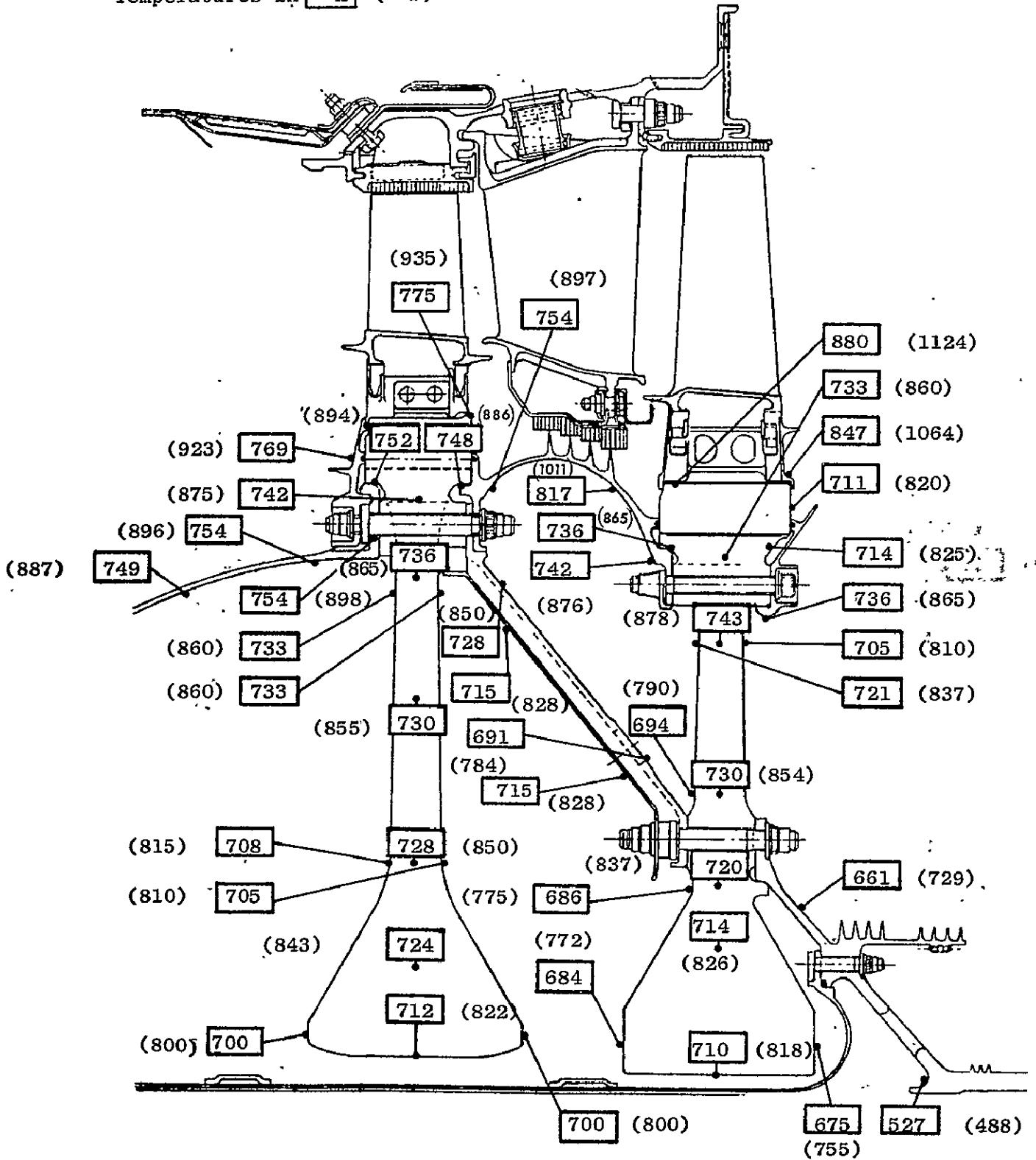


Figure 17. CF6-50C HPT Rotor Metal Temperatures at Maximum Climb Conditions.

Standard Day

Temperatures in  $^{\circ}$  K ( $^{\circ}$  F)



Standard Day

Temperatures in  $^{\circ}$  K ( $^{\circ}$  F)

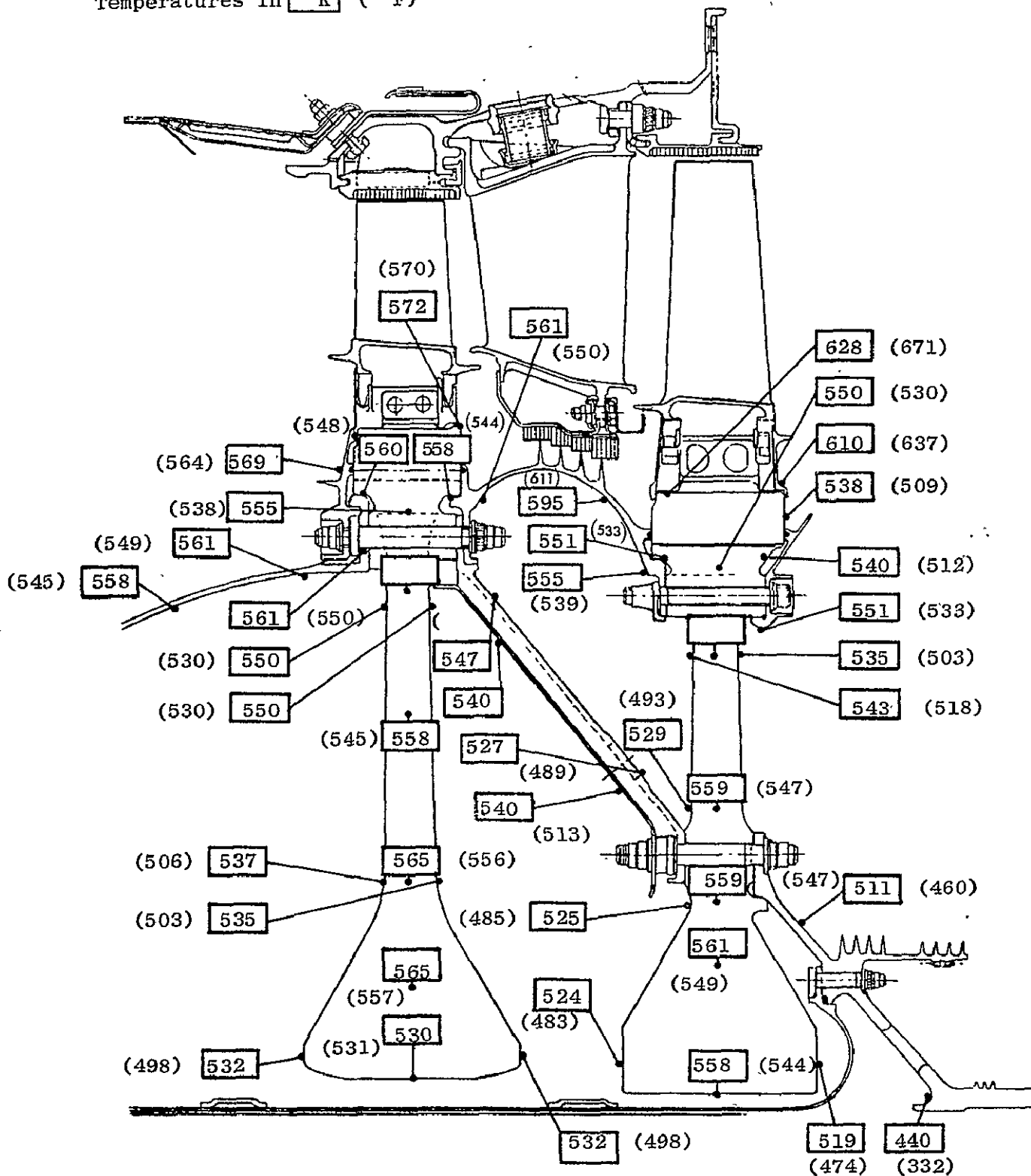


Figure 19. CF6-50C HPT Rotor Metal Temperatures at Flight Idle Conditions.

Standard Day

Temperatures in  $^{\circ}$  K ( $^{\circ}$  F)

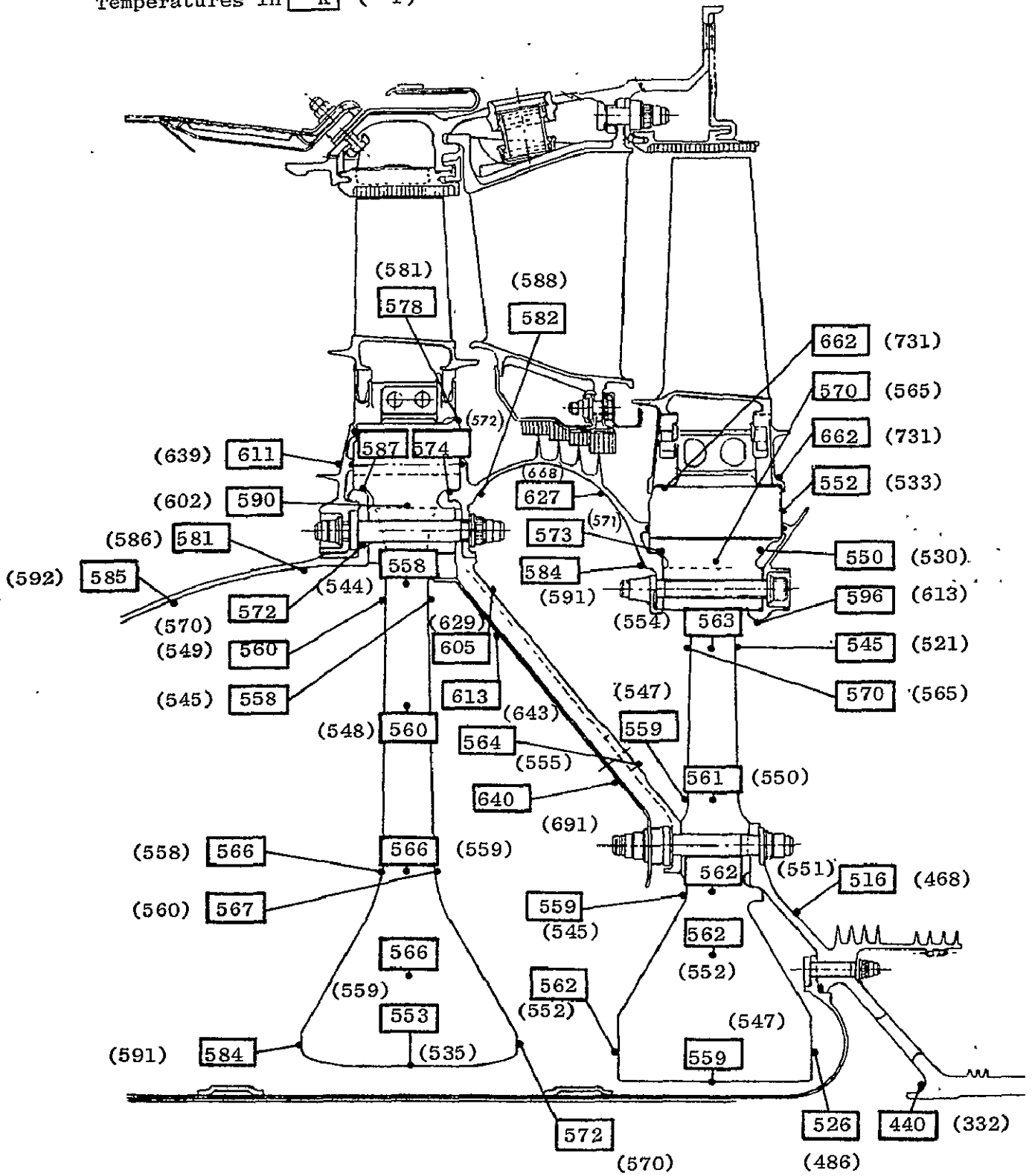


Figure 20. CF6-50C HPT Rotor Metal Temperatures at Thrust Reverse Conditions.

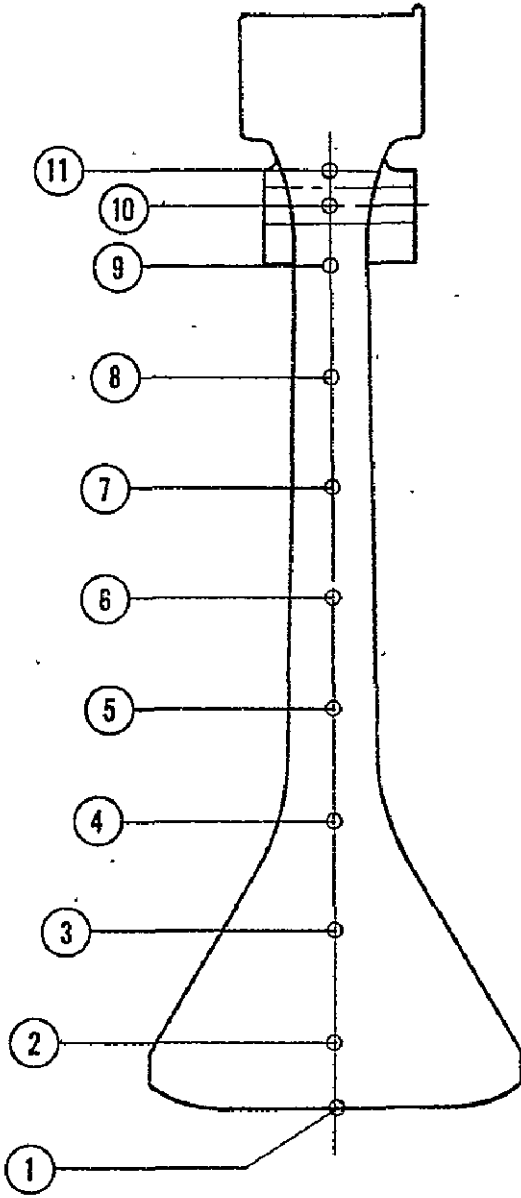


Figure 21. Standard Disk Stress and Deflection Locations.

Table II. Standard Disk Stress and Deflection  
Distribution at Takeoff 1 Conditions.

Location	Radius, mm (in.)	Tangential Stress, MPa (ksi)	Radial Stress, MPa (ksi)	Radial Deflection, mm (in.)
1	86.0 (3.39)	765.3 (111.0)	0 (0)	0.698 (0.0275)
2	101.6 (4.00)	729.4 (105.8)	100.3 (14.6)	0.746 (0.0294)
3	127.0 (5.00)	760.5 (110.3)	287.0 (41.6)	0.829 (0.0327)
4	152.4 (6.00)	749.4 (108.7)	641.6 (93.1)	0.935 (0.0368)
5	177.8 (7.00)	681.0 (98.8)	750.9 (108.9)	1.093 (0.0430)
6	203.2 (8.00)	692.7 (100.5)	739.4 (107.2)	1.260 (0.0496)
7	228.6 (9.00)	691.7 (100.3)	706.4 (102.5)	1.423 (0.0560)
8	254.0 (10.00)	637.4 (92.4)	706.3 (102.4)	1.589 (0.0626)
9	279.4 (11.00)	527.6 (83.1)	683.9 (99.2)	1.763 (0.0694)
10	293.3 (11.55)	490.3 (71.1)	549.5 (79.7)	1.860 (0.0732)
11	301.8 (11.88)	44.4 (6.4)	369.7 (53.6)	1.924 (0.0758)

Table III. Standard Disk Stress and Deflection  
Distribution at Takeoff 2 Conditions.

Location	Radius, mm (in.)	Tangential Stress, MPa (ksi)	Radial Stress, MPa (ksi)	Radial, Deflection, mm (in.)
1	86.1 (3.39)	704.3 (102.2)	0 (0)	0.858 (0.0338)
2	101.6 (4.00)	701.9 (101.8)	93.9 (13.6)	0.935 (0.0368)
3	127.0 (5.00)	775.6 (112.5)	277.3 (40.2)	1.061 (0.0418)
4	152.4 (6.00)	736.7 (106.8)	628.8 (91.2)	1.207 (0.0475)
5	177.8 (7.00)	627.9 (91.1)	731.5 (106.1)	1.415 (0.0557)
6	203.2 (8.00)	642.7 (93.2)	715.1 (103.7)	1.634 (0.0643)
7	228.6 (9.00)	643.5 (93.3)	678.8 (98.4)	1.848 (0.0728)
8	254.0 (10.00)	585.5 (84.9)	674.2 (97.8)	2.066 (0.0813)
9	279.4 (11.00)	516.3 (74.9)	647.7 (93.9)	2.291 (0.0902)
10	303.3 (11.95)	404.8 (58.7)	517.3 (75.0)	2.418 (0.0952)
11	301.5 (11.88)	164.5 (23.9)	346.1 (50.2)	2.496 (0.0983)

ORIGINAL PAGE IS  
OF POOR QUALITY

Table IV. Standard Disk Stress and Deflection  
Distribution at Maximum Climb  
Conditions.

Location	Radius mm (in.)	Tangential Stress MPa (ksi)	Radial Stress, MPa (ksi)	Radial Deflection, mm (in.)
1	86.0 (3.38)	804.8 (116.7)	0 (0)	0.980 (0.0386)
2	101.6 (4.00)	697.7 (98.6)	99.5 (14.4)	1.073 (0.0423)
3	127.0 (5.00)	588.1 (85.3)	258.9 (37.5)	1.249 (0.0492)
4	152.4 (6.00)	612.8 (88.9)	549.0 (79.6)	1.458 (0.0574)
5	177.8 (7.00)	621.9 (90.2)	640.8 (92.9)	1.700 (0.0669)
6	203.2 (8.00)	616.0 (89.3)	630.4 (91.4)	1.947 (0.0766)
7	228.6 (9.00)	600.8 (87.1)	598.8 (86.9)	2.191 (0.0863)
8	254.0 (10.00)	586.3 (85.0)	595.4 (86.3)	2.436 (0.0959)
9	279.4 (11.00)	565.2 (82.0)	575.2 (83.4)	2.680 (0.1055)
10	293.3 (11.55)	514.8 (74.7)	462.1 (67.0)	2.812 (0.1107)
11	301.8 (11.88)	455.7 (65.8)	310.9 (45.1)	2.886 (0.1136)

Table V. Standard Disk Stress and Deflection  
Distribution at Cruise Conditions.

Location	Radius mm (in.)	Tangential Stress, MPa (ksi)	Radial Stress, MPa (ksi)	Radial Deflection mm (in.)
1	86.0 (3.39)	768.9 (111.5)	0 (0)	0.870 (0.0342)
2	101.6 (4.00)	640.5 (92.9)	94.6 (13.7)	0.950 (0.0374)
3	127.0 (5.00)	540.1 (78.3)	243.4 (35.3)	1.104 (0.0435)
4	152.4 (6.00)	567.6 (82.3)	512.8 (74.4)	1.289 (0.0508)
5	177.8 (7.00)	586.2 (85.0)	598.7 (86.8)	1.503 (0.0592)
6	203.2 (8.00)	581.8 (84.4)	589.6 (85.5)	1.720 (0.0677)
7	228.6 (9.00)	568.8 (82.5)	560.7 (81.3)	1.935 (0.0762)
8	254.0 (10.00)	558.4 (81.0)	558.3 (81.0)	2.149 (0.0846)
9	279.4 (11.00)	541.7 (78.6)	540.4 (78.4)	2.363 (0.0930)
10	293.3 (11.55)	495.5 (71.9)	434.7 (63.0)	2.478 (0.0976)
11	301.8 (11.88)	439.0 (63.7)	292.9 (42.5)	2.543 (0.1001)

ORIGINAL PAGE IS  
OF POOR QUALITY

Table VI. Standard Disk Stress and Deflection  
Distribution at Flight Idle Conditions.

Location	Radius mm (in.)	Tangential Stress, MPa (ksi)	Radial Stress, MPa (ksi)	Radial Deflection mm (in.)
1	86.0 (3.39)	515.1 (74.7)	0 (0)	0.521 (0.0205)
2	101.6 (4.00)	422.9 (61.3)	62.9 (9.1)	0.567 (0.0223)
3	127.0 (5.00)	346.2 (50.2)	159.9 (23.2)	0.658 (0.0259)
4	152.4 (6.00)	364.3 (52.8)	333.9 (48.4)	0.769 (0.0303)
5	177.8 (7.00)	384.6 (55.8)	389.1 (56.4)	0.896 (0.0353)
6	203.2 (8.00)	390.6 (56.7)	383.7 (55.6)	1.024 (0.0403)
7	228.6 (9.00)	390.4 (56.6)	366.1 (53.1)	1.150 (0.0453)
8	254.0 (10.00)	391.9 (56.8)	366.3 (53.1)	1.273 (0.0501)
9	279.4 (11.00)	388.7 (56.4)	356.9 (51.8)	1.395 (0.0549)
10	293.3 (11.55)	356.2 (51.7)	288.3 (41.8)	1.460 (0.0575)
11	301.8 (11.88)	317.9 (46.1)	194.8 (28.3)	1.496 (0.0589)

Table VII. Standard Disk Stress and Deflection Distribution at Thrust Reverse Conditions.

Location	Radius mm (in.)	Tangential Stress, MPa (ksi)	Radial Stress, MPa (ksi)	Radial Deflection mm (in.)
1	86.0 (3.39)	831.9 (120.7)	0 (0)	0.661 (0.0260)
2	101.6 (4.00)	693.0 (100.5)	102.1 (14.8)	0.702 (0.0276)
3	127.0 (5.00)	583.7 (84.7)	262.6 (38.1)	0.792 (0.0312)
4	152.4 (6.00)	617.6 (89.6)	552.9 (80.2)	0.914 (0.0360)
5	177.8 (7.00)	646.8 (93.8)	646.3 (93.7)	1.063 (0.0419)
6	203.2 (8.00)	651.7 (94.5)	638.2 (92.6)	1.214 (0.0478)
7	228.6 (9.00)	646.8 (93.8)	609.2 (88.4)	1.361 (0.0536)
8	254.0 (10.00)	645.5 (93.6)	609.5 (88.4)	1.506 (0.0593)
9	279.4 (11.00)	633.6 (91.9)	593.4 (86.1)	1.649 (0.0649)
10	293.3 (11.55)	534.7 (77.5)	478.0 (69.3)	1.727 (0.0680)
11	301.8 (11.88)	444.9 (64.5)	321.5 (46.6)	1.771 (0.0697)

ORIGINAL PAGE IS  
OF POOR QUALITY

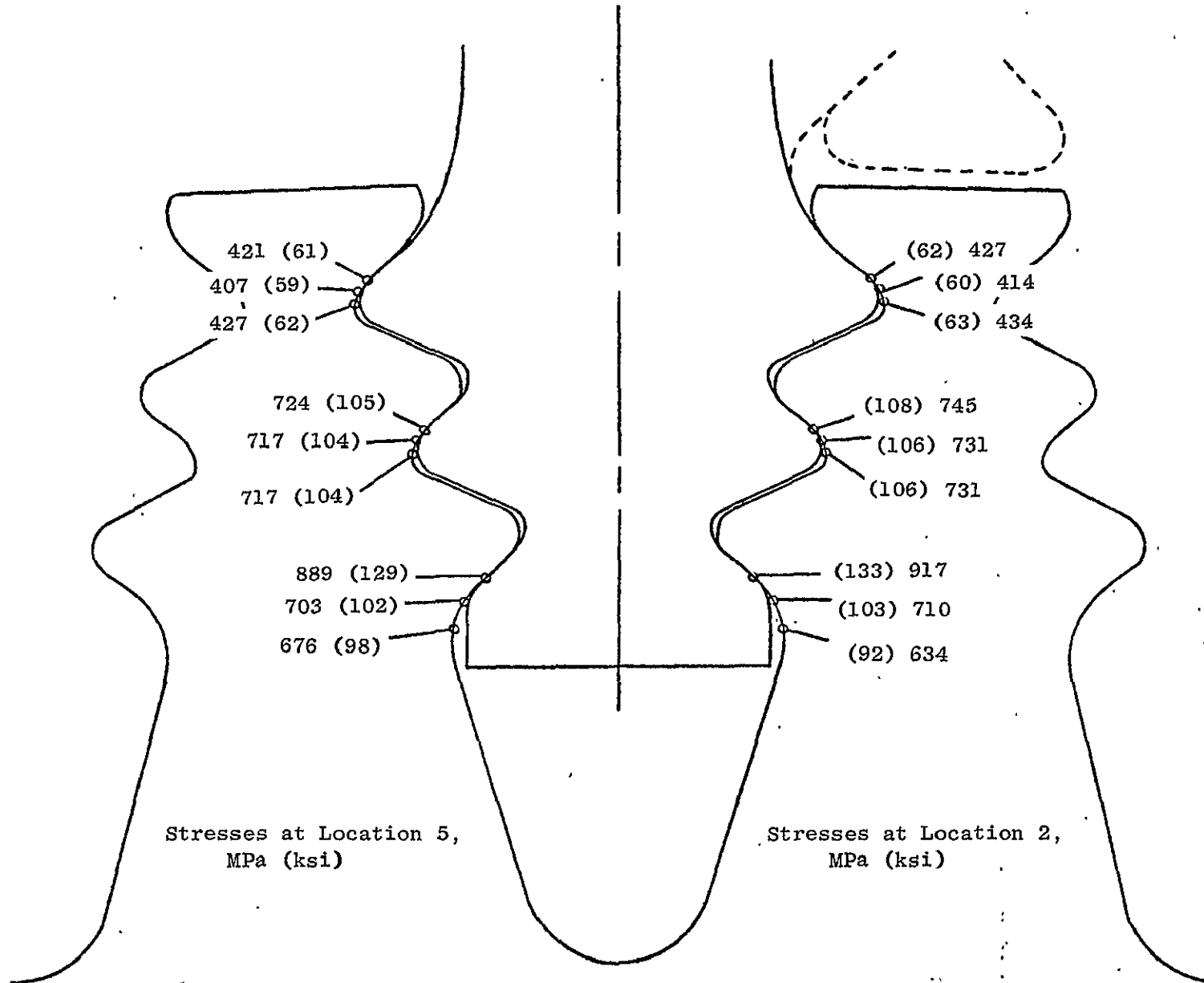


Figure 22. Standard Disk Dovetail Stresses at Takeoff 2 Conditions.

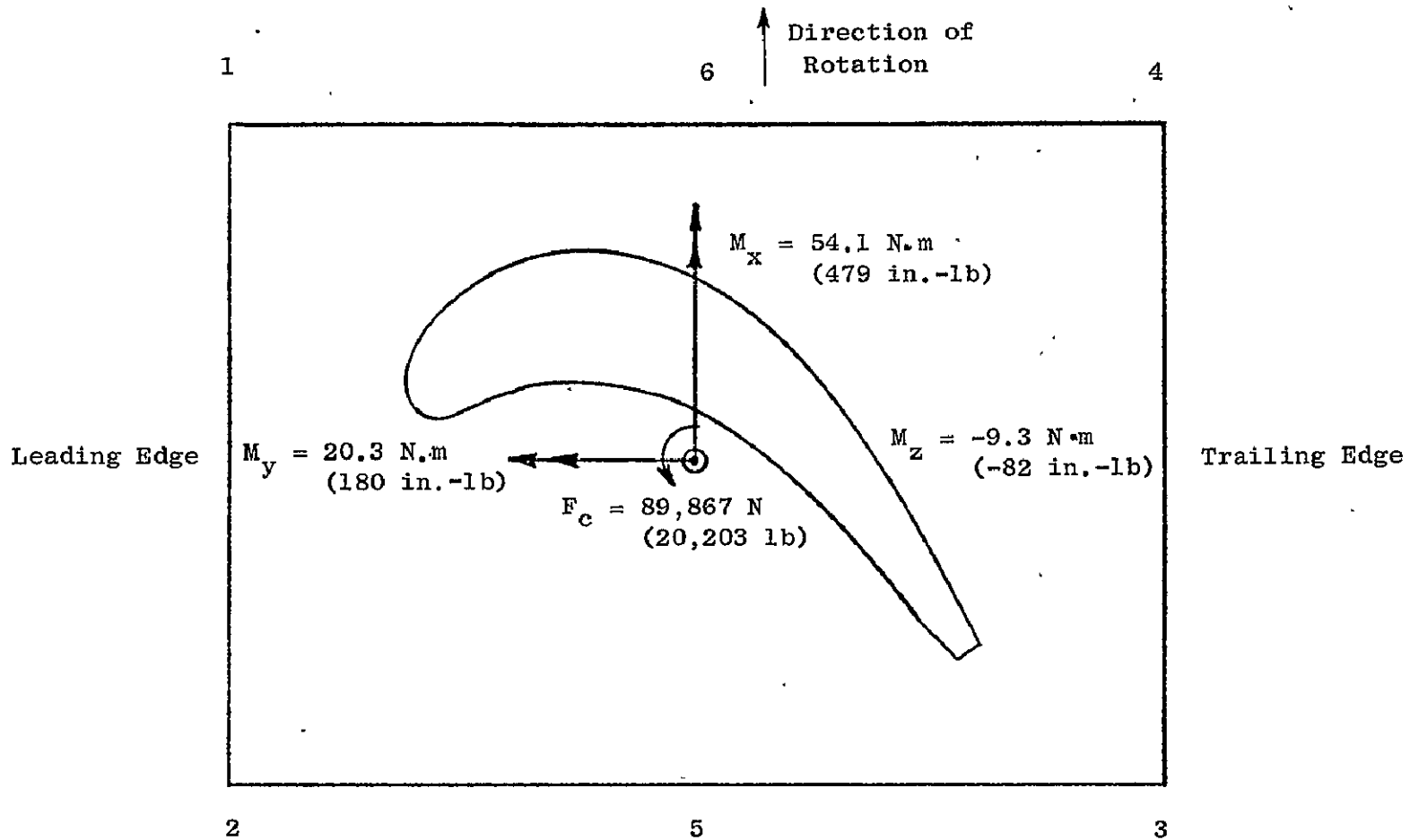


Figure 23. Standard Disk Dovetail Loading and Stress Calculation Positions at Takeoff 2 Conditions.

- Disk bore
- Aft rabbet

Cycles to crack initiation were calculated for these locations on the basis of standard day operating conditions. The dovetail slot bottom and bolt holes were calculated to have more than 100,000 cycles life, the disk bore life was calculated to be 63,000 cycles, and the aft rabbet was calculated to have 30,000 cycles LCF life.

Of these four areas, the aft rabbet has the shortest cyclic life but is the least critical in terms of disk failure. This is the case since a failure resulting from propagation in the aft rabbet region would result in the smallest fragments and the least fragment energy of the four areas considered. Thus, the three critical areas used for further analysis of the Standard Disk were the disk bore, dovetail slot bottom, and the bolt holes.

## 2. Residual Life

Using the chosen defect size in the critical areas, the propagation lives of initially flawed disks were calculated. The life of a Standard Disk with an assumed defect at the disk bore was calculated to be 611 cycles; with a defect at the dovetail slot bottom, 380 cycles; and with a defect at the bolt holes, 1809 cycles.

## E. Standard Disk Failure

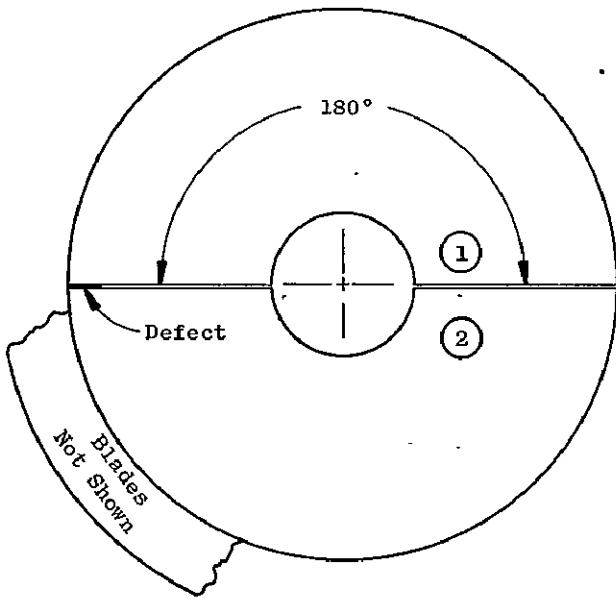
### 1. Burst Speed

Using the analysis described in Section IIIB.1, the speed at burst was calculated to be 13,345 rpm. This gave an overspeed capability of 126 percent compared with the maximum operating speed of 10,613 rpm.

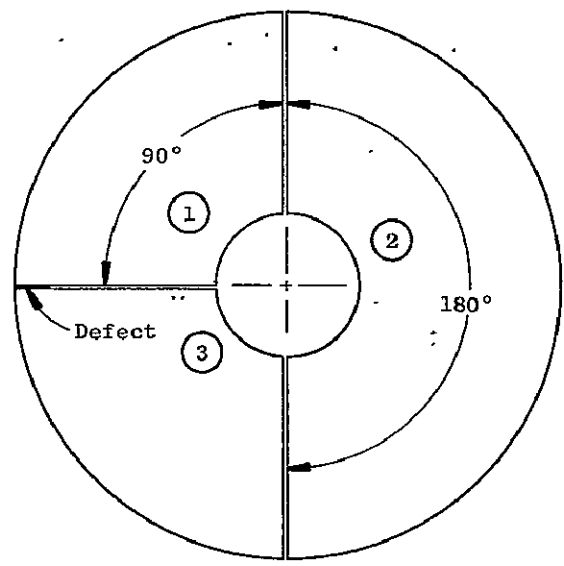
### 2. Fragment Patterns and Energies

Based on spin pit test experience, the probable Standard Disk fragment patterns depicted in Figure 24 were considered. Patterns (b), (c), and (d) were used for the analysis. Fragment pattern (a) was not recommended for specific analysis since its results would be similar to those of pattern (b). Patterns (b) and (c) would be typical of burst fragments associated with overspeed conditions and with critical crack propagation from bore or rim cracks. Experience with several single blade failures indicated that a four-blade, three-dovetail post pattern as shown in Figure 24 (d) would result from local crack propagation from an assumed defect in the dovetail slot bottom region.

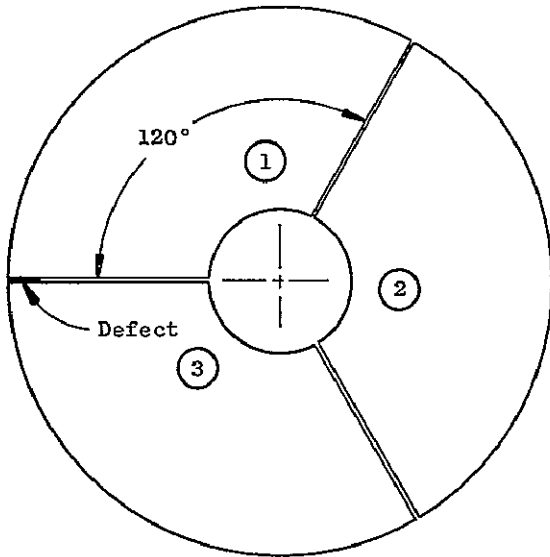
A fragment energy analysis as described in Section IIIB.2 was conducted on the Standard Disk. It must be emphasized that the mode and type of assumed failure in no way can be identified with a predetermined cause. Further, it in no way compromises any previous analysis of the engine capability to meet operational life limits as certified. The results of the analysis are given in Table VIII.



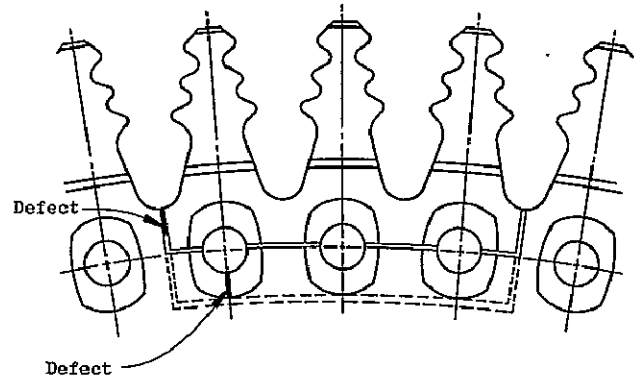
(a)



(b)



(c)



— Slot Bottom Pattern  
 - - - Bolt Hole Pattern

(d)

Figure 24. Standard Disk Fragment Patterns.

Table VIII. Kinetic Energy Available for Structural Penetration - Standard Disk.

Fragment	Rotational Energy Nm (ft-lb)	Translational Energy Nm (ft-lb)
A (90° Segment)	14,969 (30,955)	837,387 (617,625)
B (180° Segment)	370,997 (273,633)	1,387,718 (1,023,538)
C (120° Segment)	115,764 (84,383)	1,056,712 (779,391)
D	-	110,290 (81,346)
E	-	107,214 (79,077)

## SECTION V

### ADVANCED STANDARD DISK

René 95 was selected as the material to be used in the Advanced Standard Disk as the replacement for the current material, IN 718. A comparison between René 95 and other forged disk candidate materials is presented in Table IX. As can be seen, René 95 is superior to the other candidates in tensile strength. Also, René 95 is among the best materials in low cycle fatigue at the comparison point. This would provide improved burst margin and greater cyclic life capability.

#### A. Advanced Standard Disk Temperature Distribution

René 95 physical properties are different from those of IN 718. In a transient heat transfer analysis, the important factor that differs is the thermal conductivity of René 95, which is lower by approximately 25 percent. Specific heat values show a minor difference.

The base acceleration and deceleration transients for the IN 718 Standard Disk were modified for René 95 by accounting for the above physical property changes. Then, the flight cycle temperature point calculations were rerun to give estimated temperature distributions for the Advanced Standard Disk. These are illustrated in Figures 25 through 30. Table X shows a comparison between Standard and Advanced Standard Disk temperatures at the six flight cycle points.

#### B. Advanced Standard Disk Stress Distribution

The Advanced Standard Disk was analyzed in a manner similar to that used on the Standard Disk. The estimated temperature distribution was utilized to provide for any difference in thermal response. The results are listed in Tables XI and XII for the Maximum Climb and Thrust Reverse flight cycle points. The locations used correspond to those shown in Figure 21. Only these two cases were run as they were the life-limiting cycle points for the Standard Disk. Table XIII shows a comparison of the Standard and Advanced Standard Disk stresses at the Maximum Climb flight cycle point.

#### C. Advanced Standard Disk Weight

Since the Advanced Standard Disk has the identical geometry as the Standard Disk, the only difference in weight could come from a density change. The René 95 material used for this application is slightly more dense than the IN 718 used in the Standard Disk. Thus, there is an increase from 67.2 kg (148 lb) to 67.6 kg (149 lb) for the Advanced Standard Disk.

#### D. Advanced Standard Disk Life

The principal differences between the Standard and Advanced Standard Disk relative to failure analysis lie in the higher ultimate tensile strength

Table IX. Properties of Candidate Disk Materials.

Property	Temperature K (° F)	IN 718* Forging	Astroloy Forging	Waspaloy Forging	René 95 Forging
Ultimate Tensile Strength, MPa (ksi)	RT	1262 (183)	1255 (182)	1186 (172)	1503 (218)
	811 (1000)	1096 (159)	1165 (169)	1041 (151)	1448 (210)
	922 (1200)	1014 (147)	1124 (163)	993 (144)	1386 (201)
0.2% Offset Yield Strength, MPa (ksi)	RT	1007 (146)	903 (131)	772 (112)	1158 (168)
	811 (1000)	917 (133)	848 (123)	710 (103)	1096 (159)
	922 (1200)	855 (124)	827 (120)	683 (99)	1067 (155)
0.02% Yield Strength, MPa (ksi)	RT	876 (127)	779 (113)	655 (95)	1076 (156)
	811 (1000)	786 (114)	717 (104)	648 (94)	1007 (146)
	922 (1200)	724 (105)	689 (100)	600 (87)	965 (140)
Stress for 0.2% Creep in 100 hours	811 (1000)	910 (132)	---	---	---
	867 (1100)	731 (106)	---	648 (94)	972 (141)
	922 (1200)	517 (75)	689 (100)	524 (76)	883 (128)
	978 (1300)	228 (33)	510 (74)	365 (53)	517 (75)
Cycle for Crack Initiation at 689 MPa (100 ksi)	811 (1000)	$>6 \times 10^5$ ( $>10^5$ )	$>2 \times 10^6$ ( $>3 \times 10^4$ )	$>6 \times 10^5$ ( $>10^5$ )	$>6 \times 10^5$ ( $>10^5$ )
	922 (1200)	$>6 \times 10^5$ ( $>10^5$ )	$>2 \times 10^6$ ( $>3 \times 10^4$ )	$1.7 \times 10^5$ ( $2.5 \times 10^4$ )	$>6 \times 10^5$ ( $>10^5$ )

\*Current CF6-50 Disk Material

ORIGINAL PAGE IS  
OF POOR QUALITY

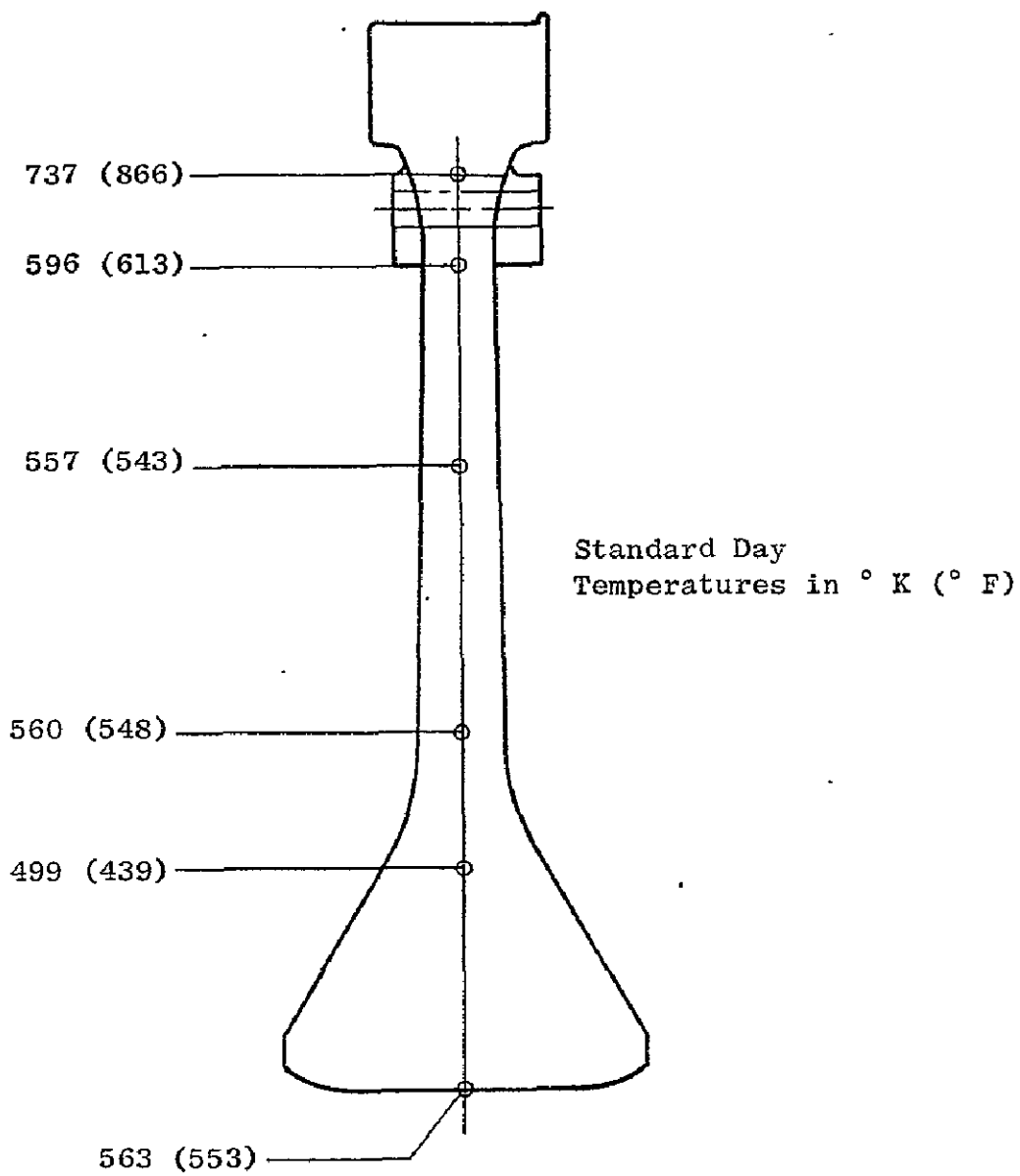


Figure 25. Advanced Standard Disk Temperature Distribution at Takeoff 1 Conditions.

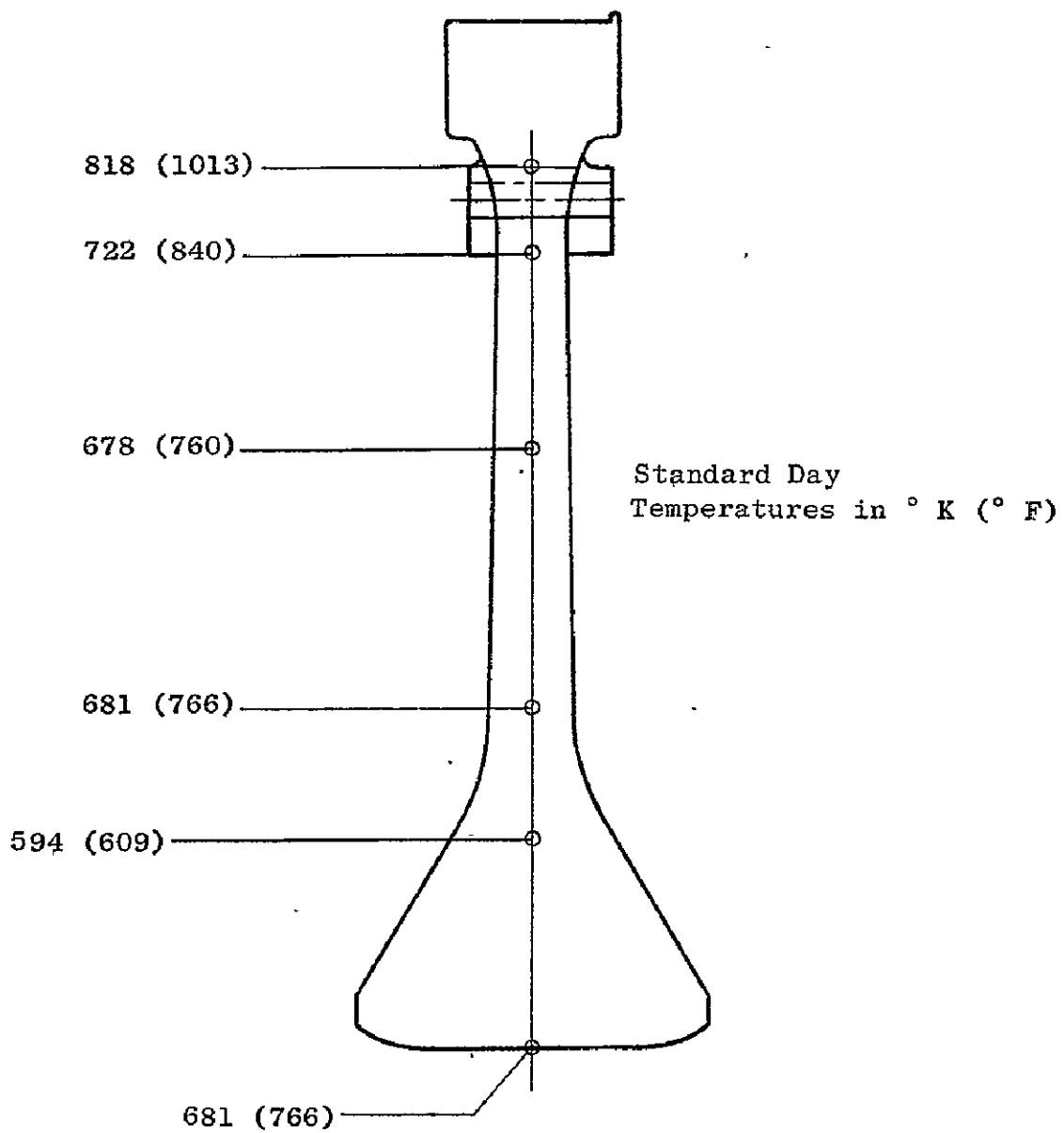


Figure 26. Advanced Standard Disk Temperature Distribution at Takeoff 2 Conditions.

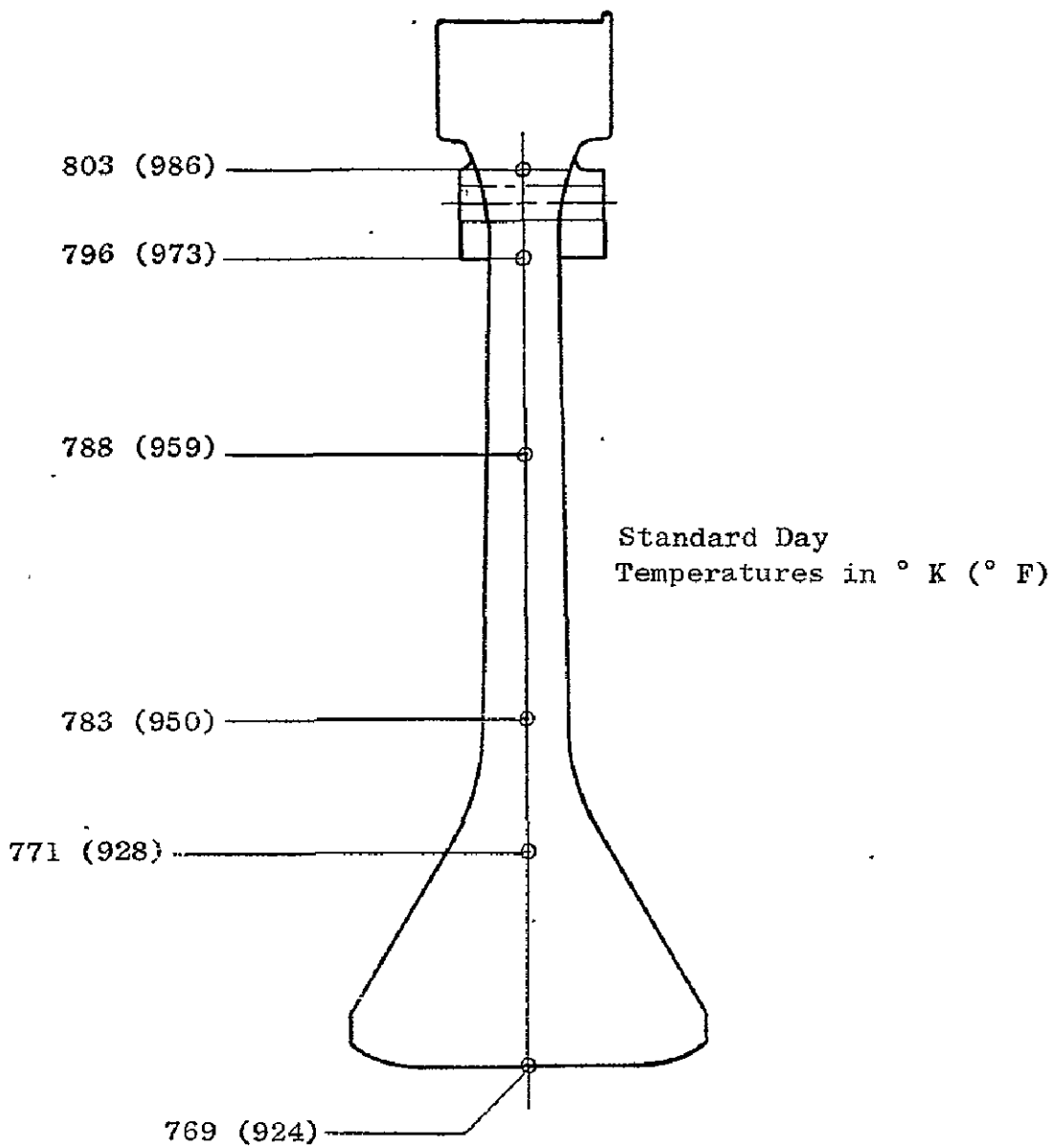


Figure 27. Advanced Standard Disk Temperature Distribution at Maximum Climb Conditions.

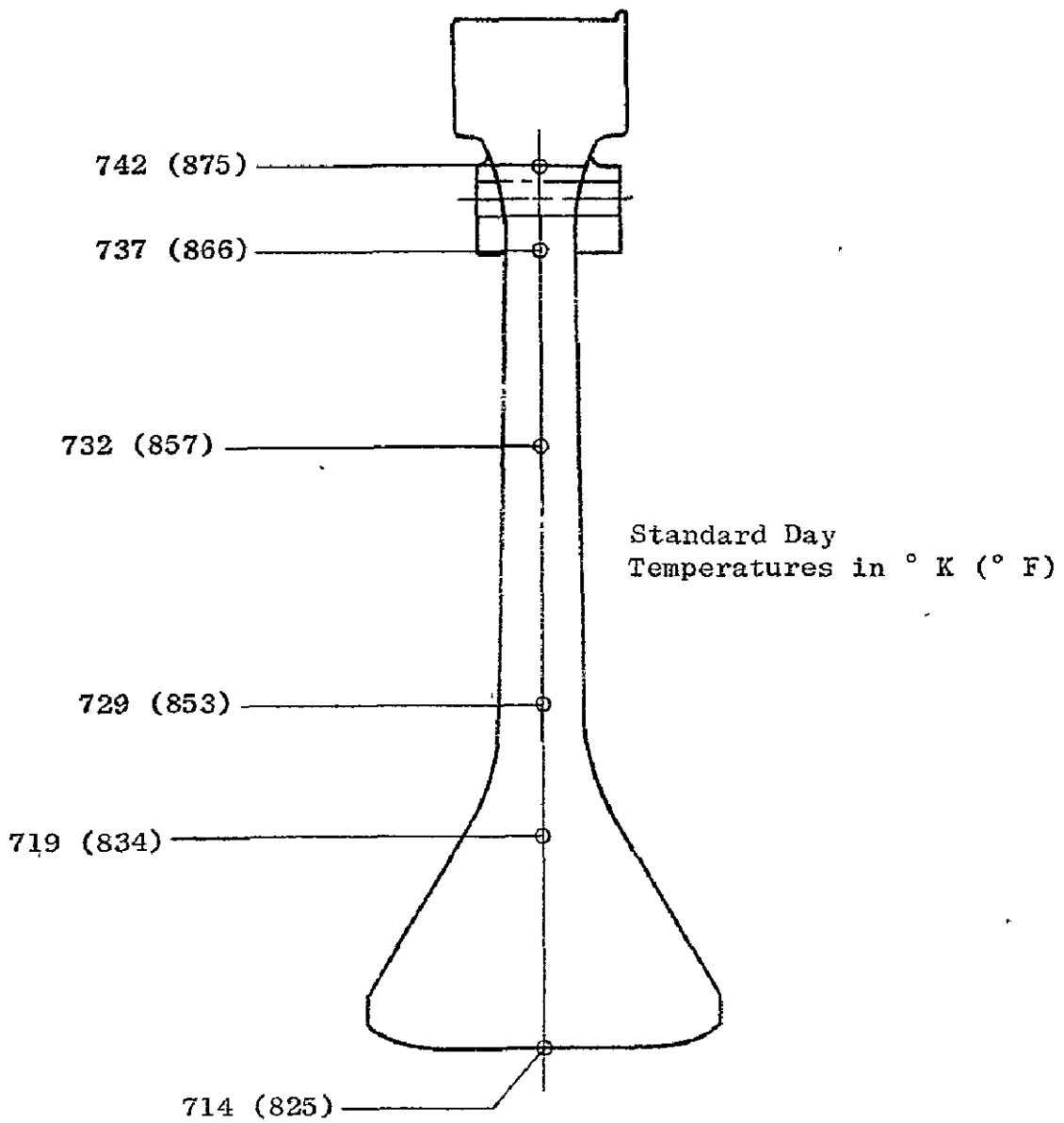


Figure 28. Advanced Standard Disk Temperature Distribution at Cruise Condition.

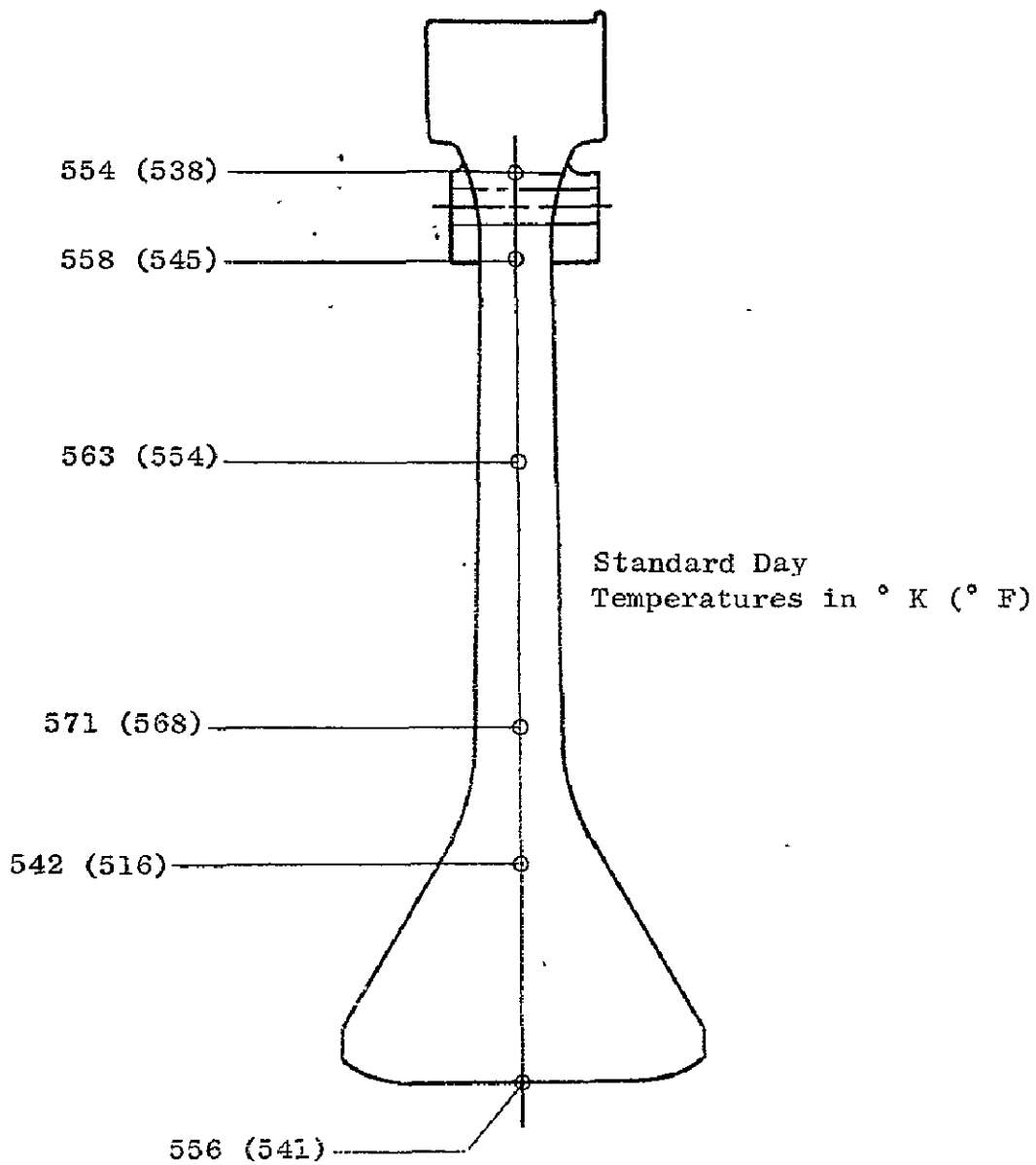


Figure 29. Advanced Standard Disk Temperature Distribution at Flight Idle Condition.

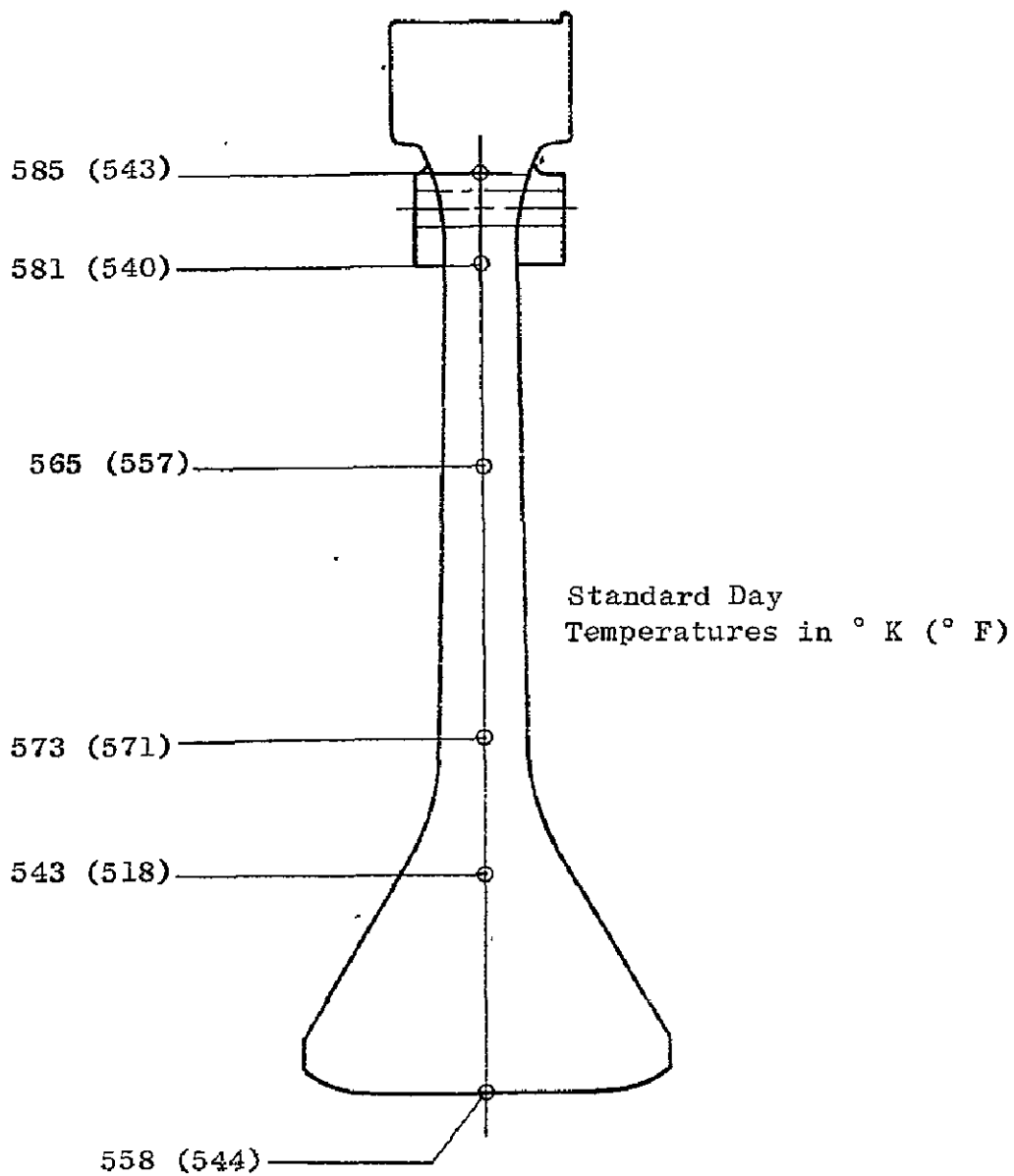


Figure 30. Advanced Standard Disk Temperature Distribution at Thrust Reverse Condition.

Table X. Temperature Comparison: Standard Disk Versus Advanced Standard Disk.

		Standard Day Temperatures, in ° K (° F).					
		Takeoff 1	Takeoff 2	Max. Climb	Cruise	Flight Idle	Thrust Reverse
Bore	Std. Disk	581 (585)	700 (800)	769 (925)	712 (822)	551 (531)	553 (535)
	Adv. Std. Disk	563 (553)	681 (766)	769 (924)	714 (825)	556 (540)	558 (544)
Web	Std. Disk	57 (577)	700 (801)	783 (950)	728 (850)	565 (556)	566 (559)
	Adv. Std. Disk	560 (548)	681 (766)	783 (950)	729 (853)	571 (568)	573 (571)
Rim	Std. Disk	754 (897)	824 (1023)	803 (986)	742 (875)	554 (538)	590 (602)
	Adv. Std. Disk	734 (866)	818 (1013)	803 (986)	742 (875)	554 (538)	585 (593)

Table XI. Advanced Standard Disk Stress and Deflection Distribution at Maximum Climb Conditions.

Location	Radius, mm (in.)	Tangential Stress, MPa (ksi)	Radial Stress, MPa (ksi)	Radial Deflection, mm (in.)
1	86.0 (3.39)	814.8 (118.2)	0 (0)	0.922 (0.0363)
2	101.6 (4.00)	690.4 (100.1)	101.0 (14.6)	1.006 (0.0396)
3	127.0 (5.00)	601.0 (87.2)	263.7 (38.2)	1.163 (0.0458)
4	152.4 (6.00)	628.3 (91.1)	560.6 (81.3)	1.354 (0.0533)
5	177.8 (7.00)	636.5 (92.3)	655.3 (95.0)	1.577 (0.0621)
6	203.2 (8.00)	629.5 (91.3)	645.3 (93.6)	1.808 (0.0712)
7	228.6 (9.00)	613.2 (88.9)	613.8 (89.0)	2.035 (0.0801)
8	254.0 (10.00)	601.5 (87.2)	611.2 (88.6)	2.263 (0.0891)
9	279.4 (11.00)	584.2 (84.7)	591.9 (85.8)	2.489 (0.0980)
10	293.32 (11.55)	533.7 (77.4)	476.4 (69.1)	2.611 (0.1028)
11	301.75 (11.88)	472.0 (68.5)	322.0 (46.7)	2.680 (0.1055)

Table XII. Advanced Standard Disk Stress and Deflection Distribution at Thrust Reverse Conditions.

Location	Radius, mm (in.)	Tangential Stress, MPa (ksi)	Radial Stress, MPa (ksi)	Radial Deflection, mm (in.)
1	86.0 (3.39)	794.3 (115.2)	0 (0)	0.638 (0.0251)
2	101.6 (4.00)	691.6 (100.3)	99.3 (14.4)	0.673 (0.0265)
3	127.0 (5.00)	630.1 (91.4)	264.5 (38.4)	0.752 (0.0296)
4	152.4 (6.00)	640.1 (92.8)	568.1 (82.4)	0.859 (0.0338)
5	177.8 (7.00)	628.4 (91.1)	661.6 (96.0)	1.003 (0.0395)
6	203.2 (8.00)	637.0 (92.4)	650.1 (94.3)	1.151 (0.0453)
7	228.6 (9.00)	634.5 (92.0)	618.3 (89.7)	1.295 (0.0510)
8	254.0 (10.00)	637.7 (92.5)	617.1 (89.5)	1.435 (0.0565)
9	279.4 (11.00)	629.9 (91.4)	599.9 (87.0)	1.572 (0.0619)
10	293.32 (11.55)	553.0 (80.2)	483.5 (70.1)	1.648 (0.0649)
11	301.75 (11.88)	475.9 (69.0)	326.2 (47.3)	1.687 (0.0664)

Table XIII. Stress Comparison at Maximum Climb Conditions:  
Standard Disk Versus Advanced Standard Disk.

		Tangential Stress, MPa (ksi)	Radial Stress, MPa (ksi)
Bore	Std. Disk	804.6 (116.7)	0
	Adv. Std. Disk	815.0 (118.2)	0
	% Δ	1.3	0
Web	Std. Disk	621.9 (90.2)	644.0 (93.4)
	Adv. Std. Disk	635.7 (92.2)	658.4 (95.5)
	% Δ	2.2	2.3
Bolt Circle	Std. Disk	515.0 (74.7)	461.9 (67.0)
	Adv. Std. Disk	533.7 (77.4)	476.4 (69.1)
	% Δ	3.6	3.1
Rim	Std. Disk	453.7 (65.8)	311.0 (45.1)
	Adv. Std. Disk	472.3 (68.5)	322.0 (46.7)
	% Δ	4.1	3.6

and improved cyclic crack growth holdtime characteristics of the René 95 material. The Advanced Standard Disk is thus superior to the Standard Disk as illustrated in the following sections.

1. Low Cycle Fatigue Life

Because of the identical geometry, the critical areas for the Advanced Standard Disk were taken to be identical to those of the Standard Disk.

LCF life calculations were performed on the Advanced Standard Disk using the method previously described. The results, presented in Table XIV with comparison numbers for the Standard Disk, indicate that a life improvement does result from directly substituting René 95 material for IN 718 in the existing disk geometry. The cycles to crack initiation for the Advanced Standard Disk are greater than those of the Standard Disk in the dovetail slot bottom and bolt hole locations. At the bore, the life increased from 63,000 cycles to more than 100,000 cycles. These results reflect the higher ultimate tensile strength and endurance limit of the René 95 material.

Table XIV. Disk Life Comparison - Standard and Advanced Standard Disks.

	Initially Unflawed Disk, Cycles to Crack Initiation		Initially Flawed Disk, Cycles of Crack Propagation	
	Standard Disk	Advanced Standard Disk	Standard Disk	Advanced Standard Disk
Disk Bore	63,000	>100,000	611	662
Slot Bottom	>100,000	>100,000	380	1,155
Bolt Holes	>100,000	>100,000	1,809	7,161

2. Residual Life

Crack propagation lives also are compared in Table XIV. The Advanced Standard Disk is superior in every case. This benefit is primarily due to the improved cyclic crack growth holdtime capability of the René 95 material at the disk operating temperatures.

The differences in the relative improvement for the various defect locations can be illustrated using the schematic in Figure 31. For the climb portion of the flight cycle, a comparison of the crack growth rate versus the stress intensity factor curves for the Standard and Advanced Standard Disk materials is shown. The stress levels at the several locations result in initial stress intensity factors as shown. Since residual life is inversely proportional to the area under the curve, the bolt hole and slot bottom locations were expected to show much more improvement in life than the bore. This was the case, as illustrated in Table XIV.

The effect of defect size on crack propagation cycles was studied for initial defect sizes other than 6.35 mm (0.25 in.). Figure 32 shows the

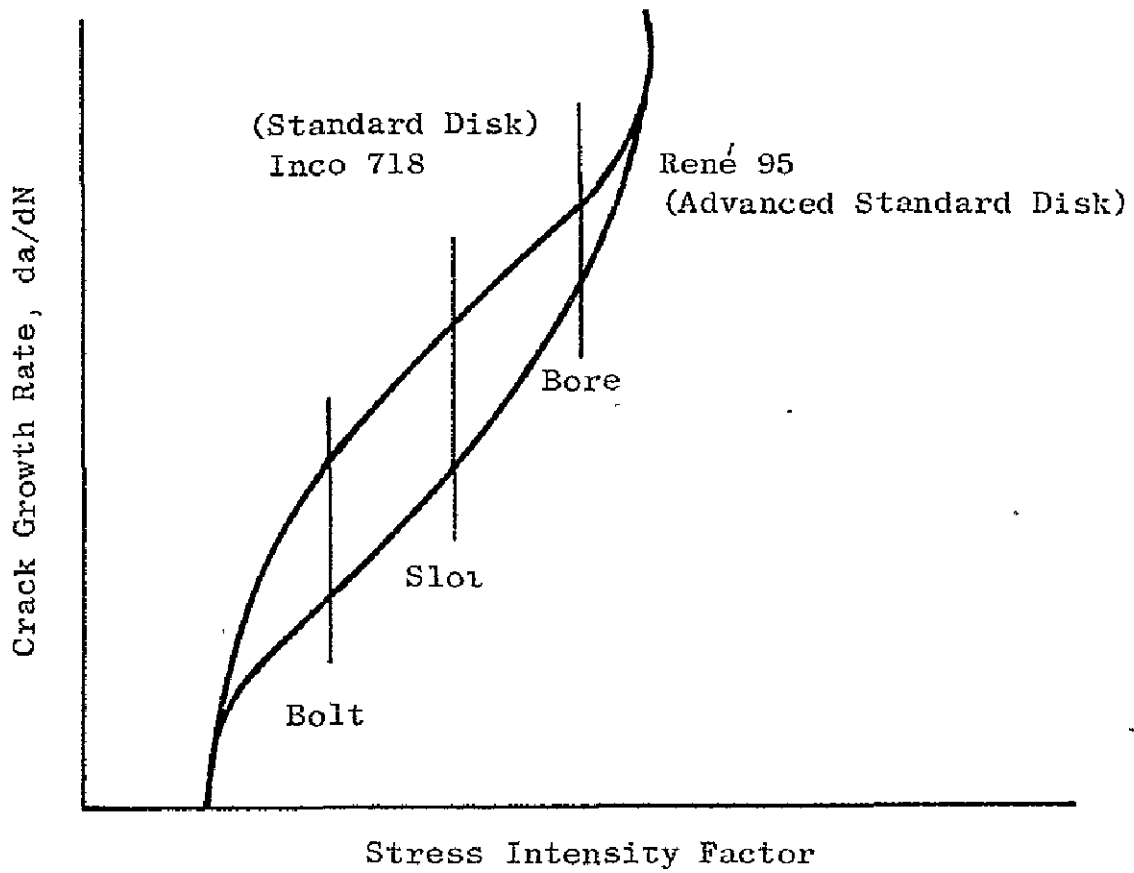


Figure 31. René 95 and Inco 718 Cyclic Crack Growth Rate Schematic Curves at Maximum Climb Condition.

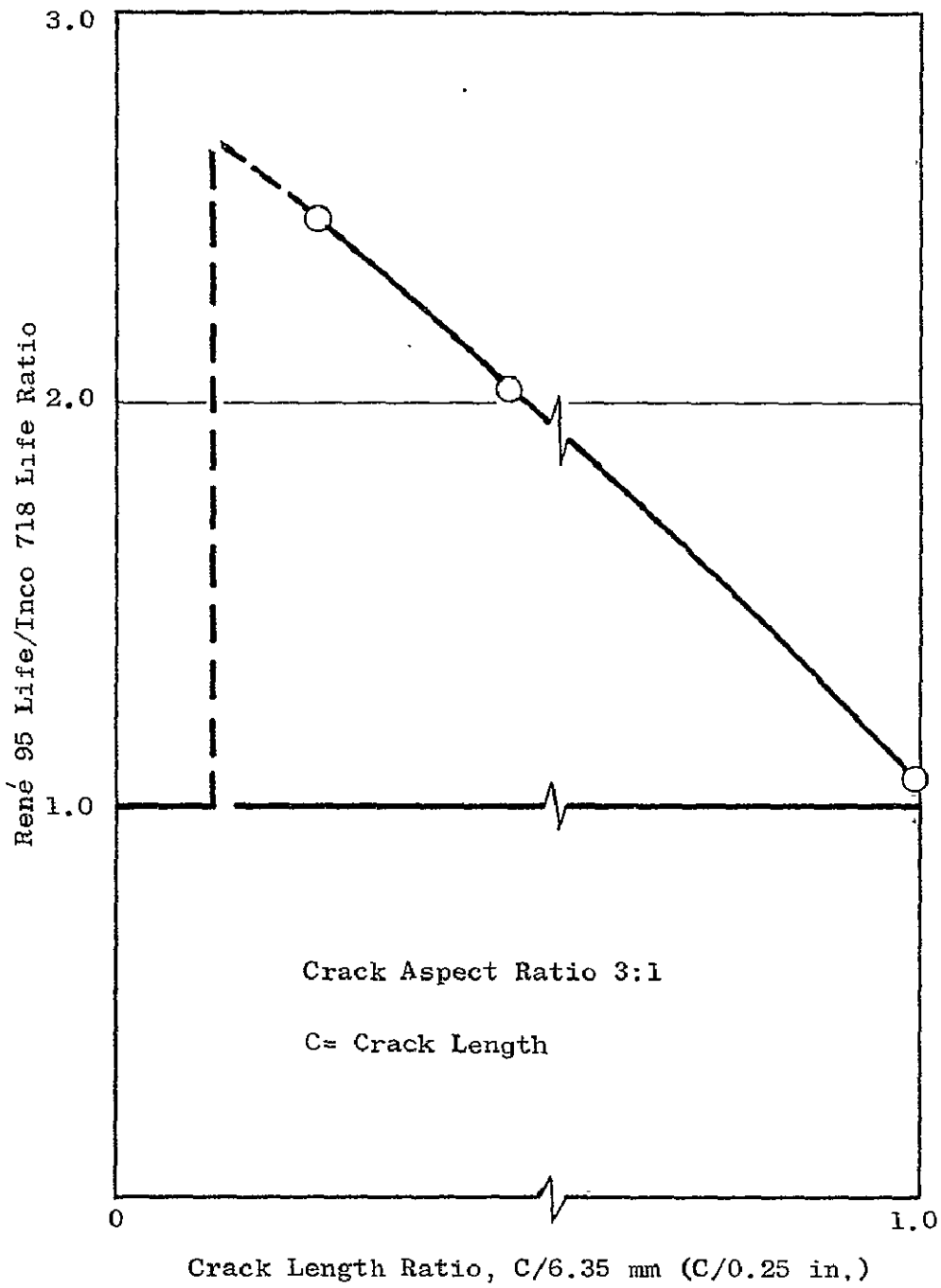


Figure 32. René 95/Inco 718 Crack Propagation Life Ratio Vs. Assumed Initial Defect Size.

results of this study. As can be seen from the figure, the life of the Advanced Standard Disk relative to the Standard Disk increases with decreasing initial defect size. Thus, the analyses with the 6.35 mm (0.25 in.) defect are conservative in life prediction, if a single life ratio is employed.

E. Advanced Standard Disk Failure

1. Burst Speed

Another improvement of the Advanced Standard Disk is the greater burst margin. The Advanced Standard Disk was calculated to burst at 14,184 rpm, or 134 percent of the maximum disk speed, compared to 13,345 rpm, or 126 percent, for the Standard Disk. This, too, is a consequence of the higher ultimate tensile strength of the René 95 material.

2. Fragment Patterns and Energies

The geometry of the Advanced Standard Disk is identical to the Standard Disk; hence, the fragment patterns were assumed to be the same.

It must again be emphasized that the mode and type of assumed failure in no way can be identified with a predetermined cause. Further, it in no way compromises any previous analysis of the engine capability to meet operational life limits as certified. The fragments considered were as depicted in Figure 24. The results of the analysis are given in Table XV. These results can be compared with those obtained for the Standard Disk by referring to Table VIII. The higher density of the René 95 material accounts for the slightly higher energies of the Advanced Standard Disk.

Table XV. Kinetic Energy Available for Structural Penetration - Advanced Structural Disk.

Fragment	Rotational Energy Nm (ft-lb)	Translational Energy Nm (ft-lb)
A (90° Segment)	42,167 (13,101)	839,425 (619,128)
B (180° Segment)	377,751 (274,927)	1,390,436 (1,025,533)
C (120° Segment)	116,312 (85,787)	1,059,147 (781,187)
D	-	110,450 (81,464)
E	-	107,398 (79,176)

## SECTION VI

### ALTERNATIVE DISK DESIGN CONCEPTS

Work is performed on a continuing basis to improve material properties, analysis techniques, and manufacturing methods to yield longer life, high-performance disks and keep the probability of high-pressure disk failure to a minimum. Past studies have indicated a potential for improving disk life and safety through mechanical design. This potential lies in the area of mechanical design addressing that period of time following the initiation of a crack in a critical area of the disk.

Methods for extending life after crack initiation include retarding crack propagation, stopping crack propagation, or allowing cracks to propagate in a manner such that detection and no damage, or minimum damage, will result.

Candidate design disk concepts were investigated which primarily addressed the extension of disk life after crack initiation; however, life before crack initiation may also be increased.

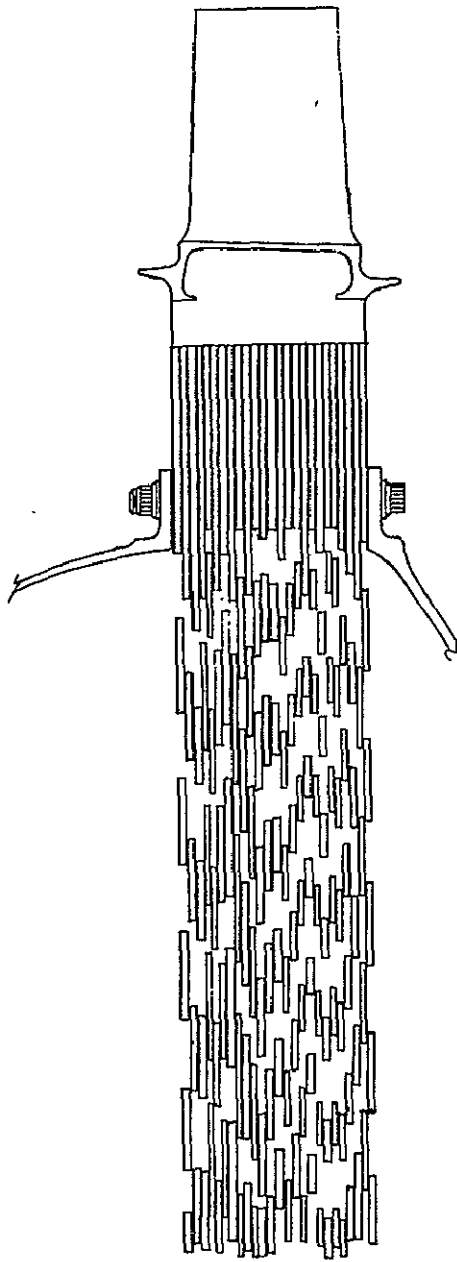
#### A. Link Disk

The Link Disk design concept was initially developed in preliminary studies made prior to this program in which this concept was shown to be feasible for the fan disk on the CF6-6 engine. Figure 33 shows a cross section of the Link Disk as it might appear in the CF6-50 turbine.

Transverse forces on the links (due to the link weight) and the blade load at the ends of the links are proportional to the centrifugal field. Thus, the links have a catenary shape (modified for the radial field) to reduce bending stresses in the links. The disk is attached to shafts via the center bolt circle. For high volumetric load carrying efficiency, the links are arranged in discrete layers. A typical layer is shown in Figure 34.

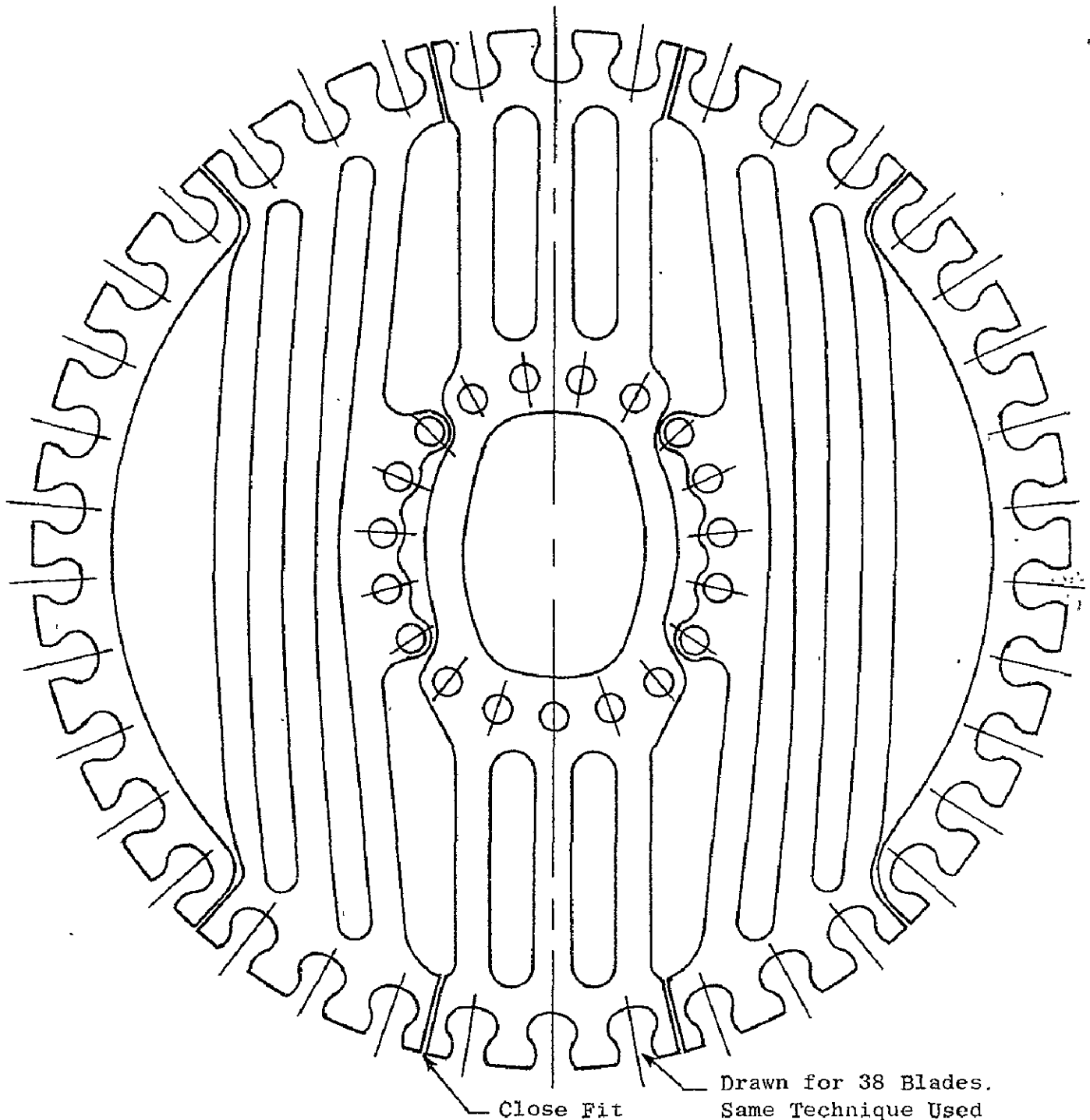
Since this concept employs a large number of small individual links, the energy fragments from a link failure would be negligible when compared to a Standard Disk burst. For this reason, the Link Disk was a natural candidate for study in this program.

Preliminary analysis on the Link Disk for the CF6-50 Stage 1 high-pressure turbine included an assessment of a link's ability to carry its own weight in the given centrifugal field. It was concluded that a typical link could not support itself when subjected to its inherent body loading. In a two-spool engine such as the CF6, the link design may be feasible for a lower-speed fan spool disk, but the higher centrifugal field of the CF6 core (high-pressure) turbine would overstress the link design. For this reason, the Link Disk design was eliminated from further consideration.



---

Figure 33. Link Disk Cross Section  
in CF6-50 Turbine.



Typical Disk Would Contain 20 to 40  
Layers, Each Clocked Tangentially Relative  
to the Next.

Drawn for 38 Blades.  
Same Technique Used  
for 80 Blades.

Figure 34. Typical Layer of Links for Dovetail Blade Attachment.

## B. Laminated Disk

The Laminated Disk design concept involves a disk constructed of several sheet metal disks bolted together. Thickness distribution would be controlled by adding reinforcing disks at the bore and rim. Figure 35 shows this concept.

The most important potential advantage of this concept is the ability of the disk to experience failure of one lamina without suffering immediate burst of the entire disk. As the remaining laminas pick up the load from the failed lamina, the disk would signal the problem by imbalance or increased radial growth with a tip rub.

Another advantage is the fact that the laminas could be stamped out of sheet metal, greatly reducing the fabrication costs associated with conventional forged and machined disks. Due to the constant thickness of the sheet metal, each lamina could be easily inspected ultrasonically for internal flaws. Also, the disk could be disassembled for detailed inspection at overhaul.

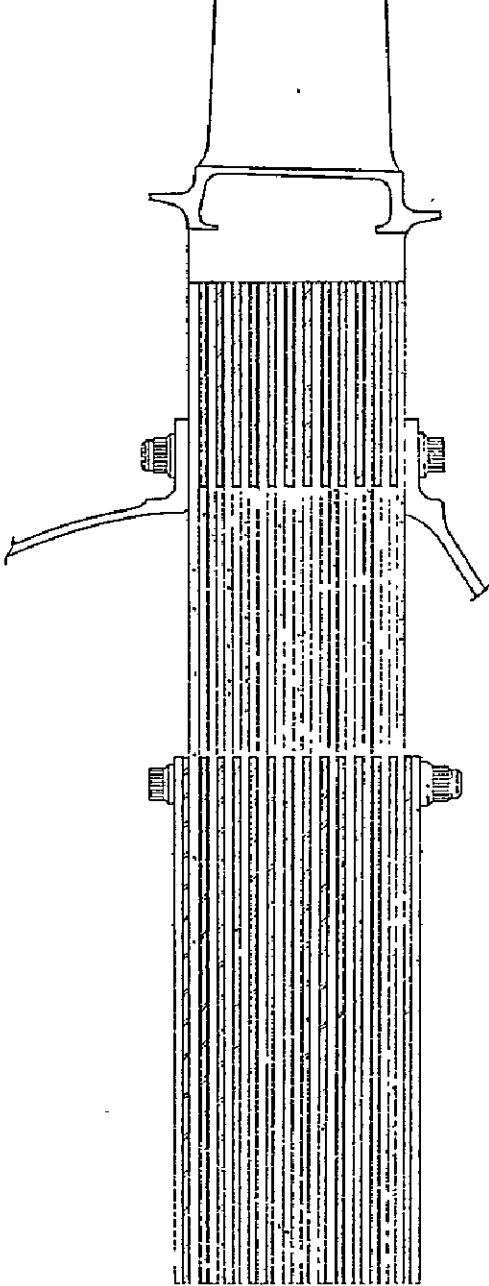
A limitation of the Laminated Disk is that the thickness distribution would have to be as step functions. This is very inefficient in carrying loads and increases the weight substantially.

René 41 was selected as the material for the Laminated Disk because it was the highest strength material available in sheet form. René 41 has a large differential between 0.2 percent yield strength and ultimate strength, which in the event of one or two laminas failing would allow very large deflections of the disk before all laminas fail. This should assure tip rub indications if individual laminas fail.

A preliminary analysis was conducted on a Laminated Disk to determine stresses and to estimate the cyclic life capacity of this configuration. The analysis was performed using the CF6-50 takeoff wheel speeds and rim loads, and the initial thickness proportions were based on those of the Standard Disk. Connection of one level of sheet material to another was achieved through the use of bolts. Since each bolt circle introduces stress concentrations, the number of bolt circles and, thus, the number of thickness changes must be kept to a minimum in order to efficiently use the sheet material. Three thickness sections were used: rim section, web section, and bore section. They were connected by 80 bolts at the rim/web interface radius of 293.3 mm (11.548 in.) and by 50 bolts at the web/bore interface radius of 177.8 mm (7 in.).

Several analyses were performed using a range of web and bore thicknesses with the objective of achieving bore stresses of 0.2 percent yield strength or less and so attain cyclic life comparable to the Standard Disk. The results of these analyses are presented in Figure 36. A combination of rim, web and bore thicknesses was identified that had a reasonable balance between web and bore stress levels.

Analysis of the bolt showed that it cannot carry the load generated at the bore overhang from the web. It is deficient in two modes. The first mode



---

Figure 35. Laminated Disk.

ORIGINAL PAGE IS  
 OF POOR QUALITY

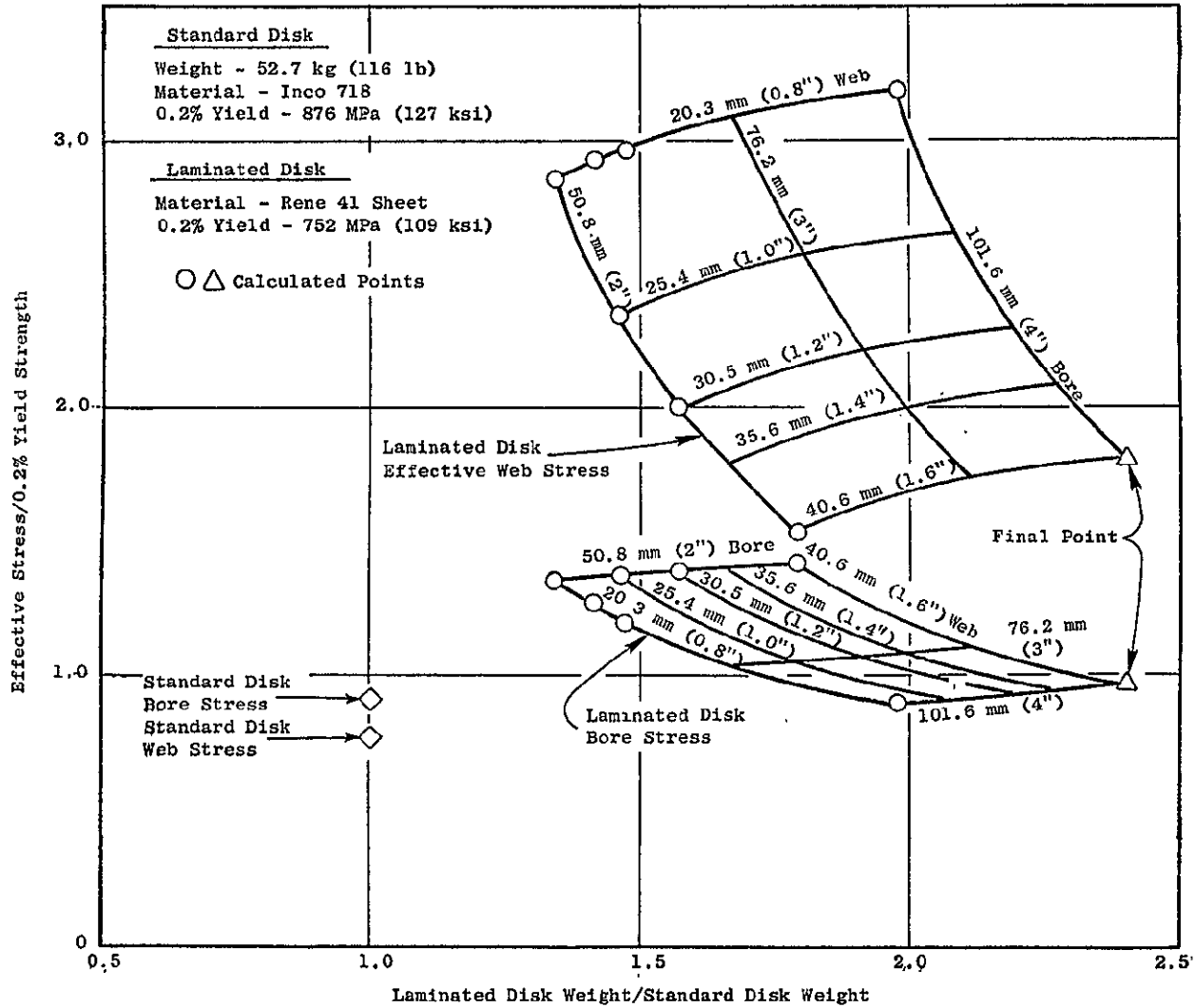


Figure 36. Laminated Disk Normalized Effective Stress Vs. Normalized Weight.

is deflection. The bolt deflects radially inward at the ends, relative to its center, unloading the overhung bore and raising stresses in the rest of the bore and web. Secondly, the calculated bolt stresses exceed the ultimate strength of the bolt material. This could be overcome by diffusion bonding the sheets together. However, this leads to another set of problems as is discussed later.

If the laminas were bolted together with no space between them, the thermal response would be slower than a conventional one-piece forged/machined disk due to thermal contact resistance between laminas. This would lead to high thermal stress gradients across the web. If the laminas were distributed across the web with spaces between them as shown in Figure 35, the thermal response of the inner disks would be significantly slower than the outer disks, since the primary mode of heat transfer of the inner disks will be radiation. To prevent severe thermal mismatches, air must be channeled through the spaces. There are two alternative methods to accomplish this. The first method is to provide holes in the web sheets to admit air, but this introduces a large stress concentration factor in an already highly stressed region. The second method is to bring air up through the bore by selectively omitting bore disks between web disks and moving the bore disks to the outside, while utilizing spacers between the web disks to permit the passage of air. This means increasing the bore overhang, which is ineffective because of bolt stresses and deflection, as described above.

Thus, although this study confirmed that the Laminated Disk has a desirable feature in its lack of catastrophic burst upon failure of a single element, it was also found that this configuration has severe penalties in cyclic life. Because of these cyclic life problems, the Laminated Disk was dropped from further consideration.

### C. Multibore Disk

The Multibore Disk configuration is directed toward flaws or cracks in the critical, highly stressed region of the disk bore. Figure 37 depicts the multibore configuration.

Each of the individual bores (or continuous circumferential ribs) has a tangential stress distribution in the radial direction similar to that of the original solid disk. Should a crack initiate from an undetected defect at the highly stressed inside diameter of the rib (bore), it should only propagate radially outward to the outer diameter of the rib. In the area of the outer diameter of the rib, radial and axial stresses are small relative to tangential stress, and the tangential stress would drop to approximately 75 percent of the bore stress. In this lower stress field, the crack propagation rate would be significantly lower than that of a crack propagating from the highly stressed bore of a solid disk. Based on this lower propagation rate, a practical inspection period could be established such that the large but very slowly propagating cracks could be easily detected before they propagate to impending disk failure.

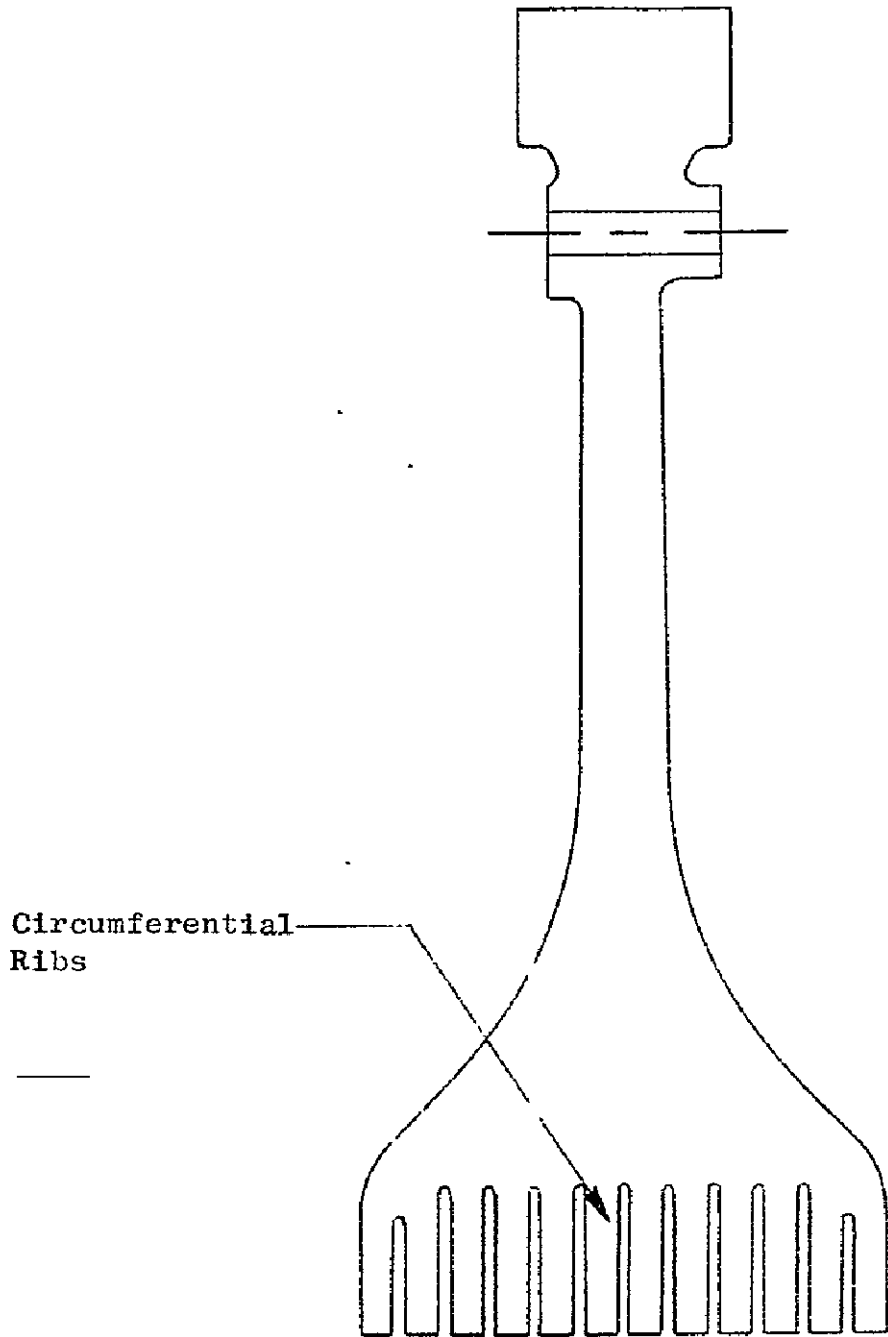


Figure 37. Multibore Disk.

However, the transient stress analysis of such a multibore design operating at the CF6 takeoff condition revealed that the temperature gradient forces the tangential stress to a maximum in an area more than 25 mm (one inch) radially outward from the top of the circumferential ribs (see Figure 38). As a result, a crack that had propagated radially to the top of a rib would see a still higher stress field above it. This would accelerate the crack growth rather than inhibit it as originally postulated, and therefore the anticipated benefit of this design would not be realized. As a possible solution, one could extend the circumferential rib height radially outward. However, to reach the necessary reduced stress level, the configuration required would be similar to the Multidisk design concept. Therefore, further effort in this area was transferred to the Multidisk concept.

#### D. Composite Disk

The Composite Disk design concept (Figure 39) substitutes high-strength filaments or wires for portions of a conventional disk. The extra load-carrying capability of the wire portion enables the designer to execute a lower stressed and longer cyclic life disk of the same weight as a conventional disk but potentially able to sustain the failure of individual elements without burst, or a lighter disk at the same stress level, or an effective compromise between the two. In the examination of this candidate disk, both the preliminary sizing of a disk and the availability of materials with the desired characteristics were investigated.

Load relieving stresses could be imposed on the wires in several ways. First, the machined disk could be wound with stressed wire which could then be secured with a matrix material. Second, unstressed wound wire could be interference-fitted onto an oversize diameter on the disk. Third, a low thermal expansion material could be assembled with the disk, and the thermal growth differentials would provide restraint on the disk.

Since the disk must be capable of operating in the CF6-50 engine environment, the composite must have an allowable operating temperature of at least 811° K (1000° F). Preliminary analysis indicated that an operating stress of 1379 MPa (200,000 psi) on the wire would be necessary to unload the disk while maintaining a reasonable balance between the amount of composite and the amount of disk material.

Figure 40 shows the available fiber and matrix candidates for the Composite Disk. Three fibers have the required temperature/stress capability. Of these, silicon carbide and boron are low thermal expansion materials, and the third, MP159, is a new high-strength nickel-base superalloy that has never been drawn into wire.

Analysis of a low thermal expansion configuration showed that substantial stress reductions and, therefore, life improvements could be achieved with proper placement of the composite material. However, the necessary manufacturing and metallurgical processes have not been demonstrated to date, and a separate development program would be required to show that a practical execution of the design would be possible.

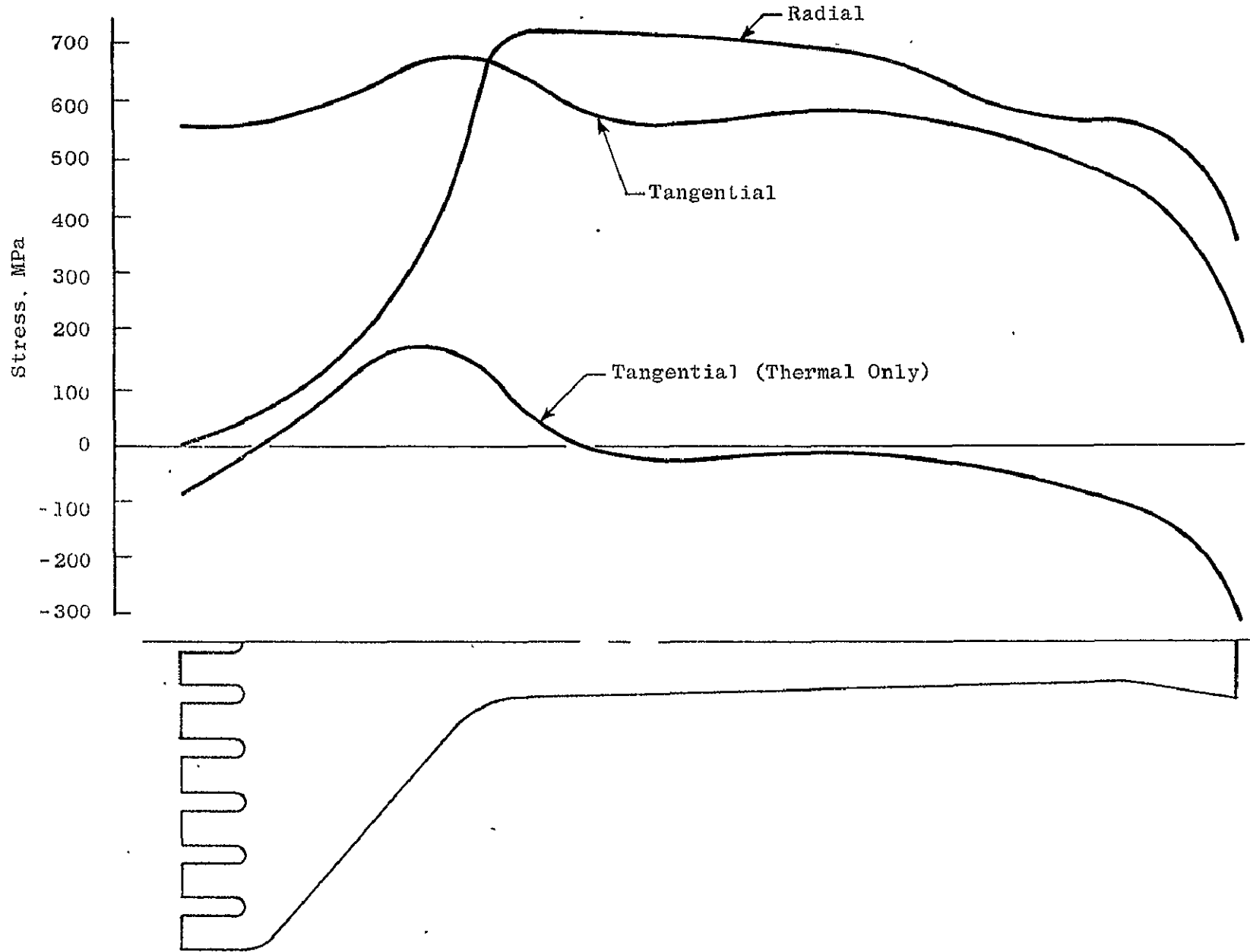
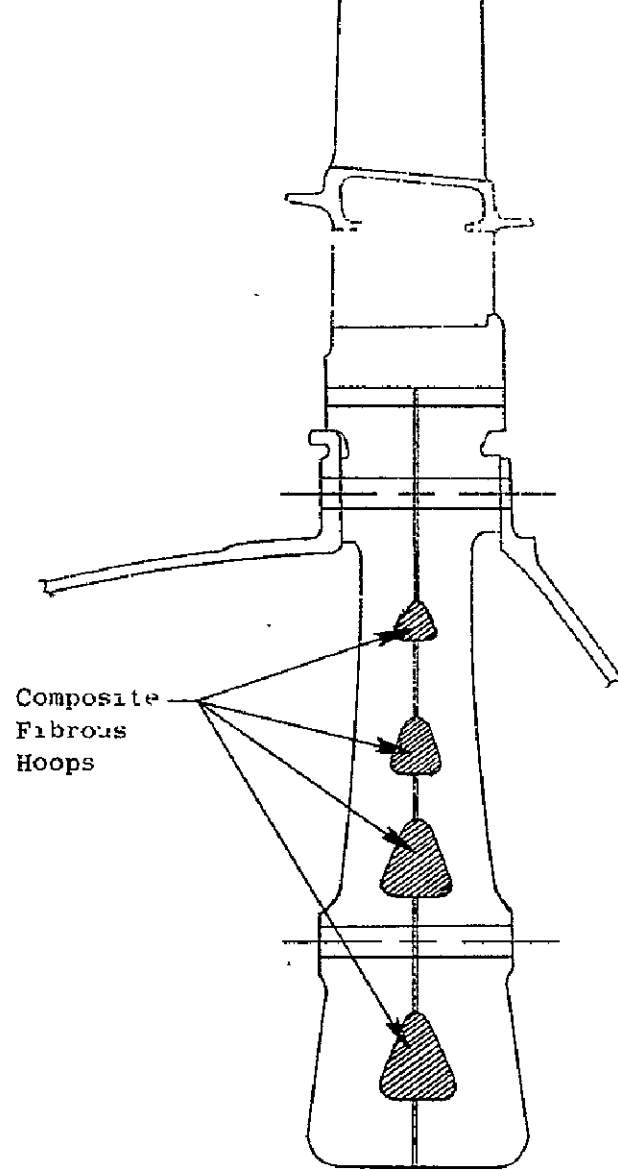


Figure 38. Multibore Transient Stress Distribution.



---

Figure 39. Composite Disk.

ORIGINAL PAGE IS  
OF POOR QUALITY

Temperature Capacity, ° K (° F)

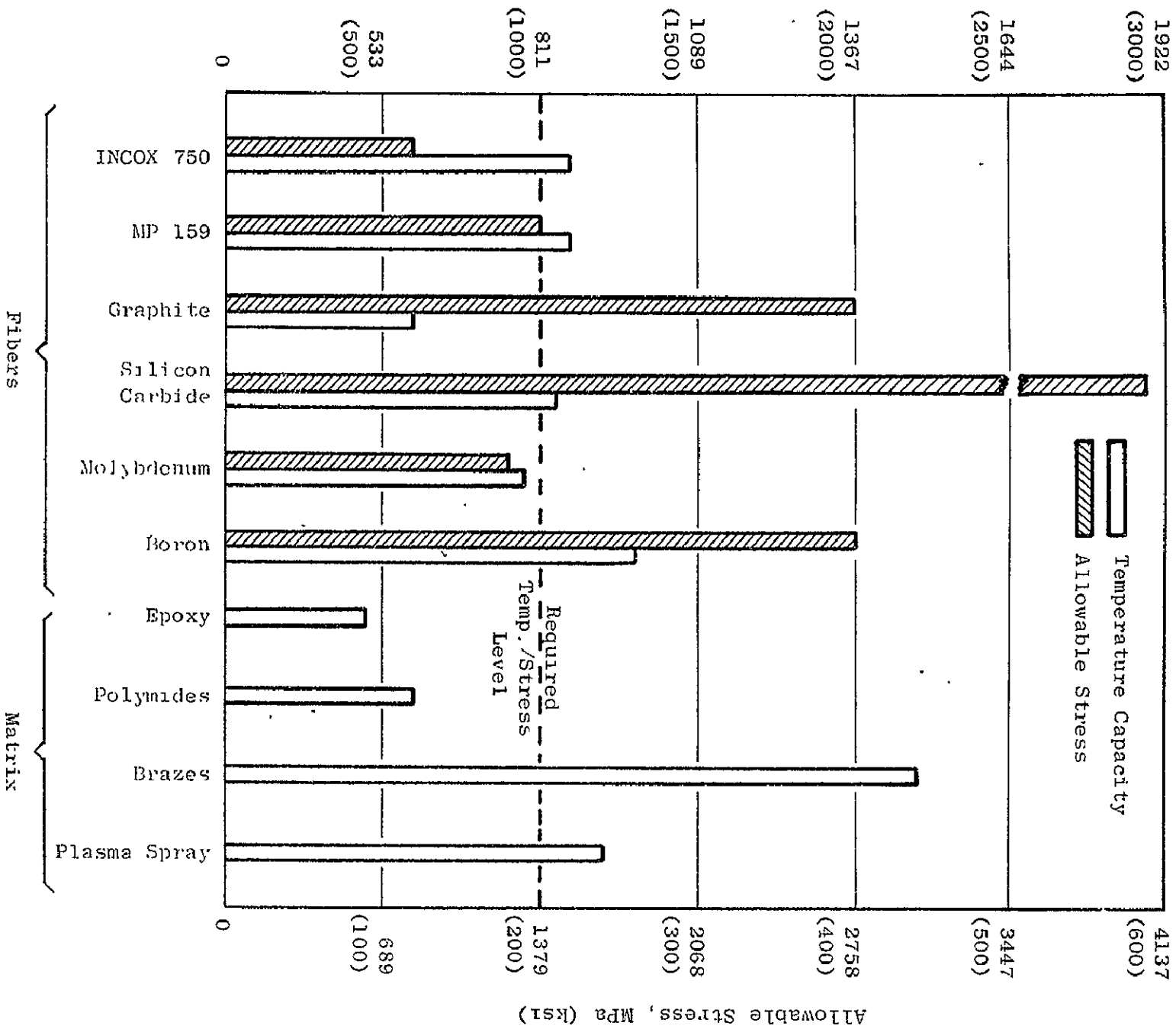


Figure 40. Composite Disk Material Candidates.

Although the Composite Disk would accomplish the major goals of this study, the lack of needed technology in the materials/manufacturing execution of the design is a limiting factor, and therefore this configuration was dropped from further consideration. If a successful composite with the desired characteristics is fabricated in the future, then the Composite Disk design concept would warrant a relook.

#### E. Multidisks

The use of a small, finite number of disks to replace the one-piece Standard Disk was the final design concept investigated. Three distinct types of Multidisks were considered:

- Bolted Multidisk
- Splined Multidisk
- Integral Multidisk

Several apparent advantages arise from the use of a Multidisk approach. First, the shaping of individual members of a Multidisk allows for a more efficient use of the material's load carrying capability than is obtainable in a laminated disk. Second, with the proper attachments between disks, the Multidisk can be designed as a redundant structure such that if one disk member should fail, the remaining members would sustain the failed disk and retain overall turbine system integrity. Third, compared with the Standard Disk, the radial temperature distribution and, thus, the thermal stresses could be reduced by bringing the cooling air up through the bore of the disk.

The preliminary analyses of each of the Multidisk types will be discussed separately.

##### 1. Bolted Multidisk

The easiest method for combining two or more disks into a Multidisk assembly is to use bolts as the attachment mechanism. A typical Bolted Multidisk is shown in Figure 41. It was originally believed that as a flaw propagated in one member of the Multidisk, the bolted connection would force a deflection match to continue to occur at the bolt circle. This then would serve to unload the flawed disk by forcing the remaining disks to carry a larger portion of the load. Thus, the unloading of the flawed disk would retard crack propagation. However, the design stress levels obtainable in disks dictate that the critical crack length (length at which a flaw propagates spontaneously) would be between 7.6 mm (0.3 in.) and 10.2 mm (0.4 in.). Investigations into the unloading behavior of a disk with this amount of effective load carrying area removed indicated that the expected load shift would not occur significantly before the crack reached critical length.

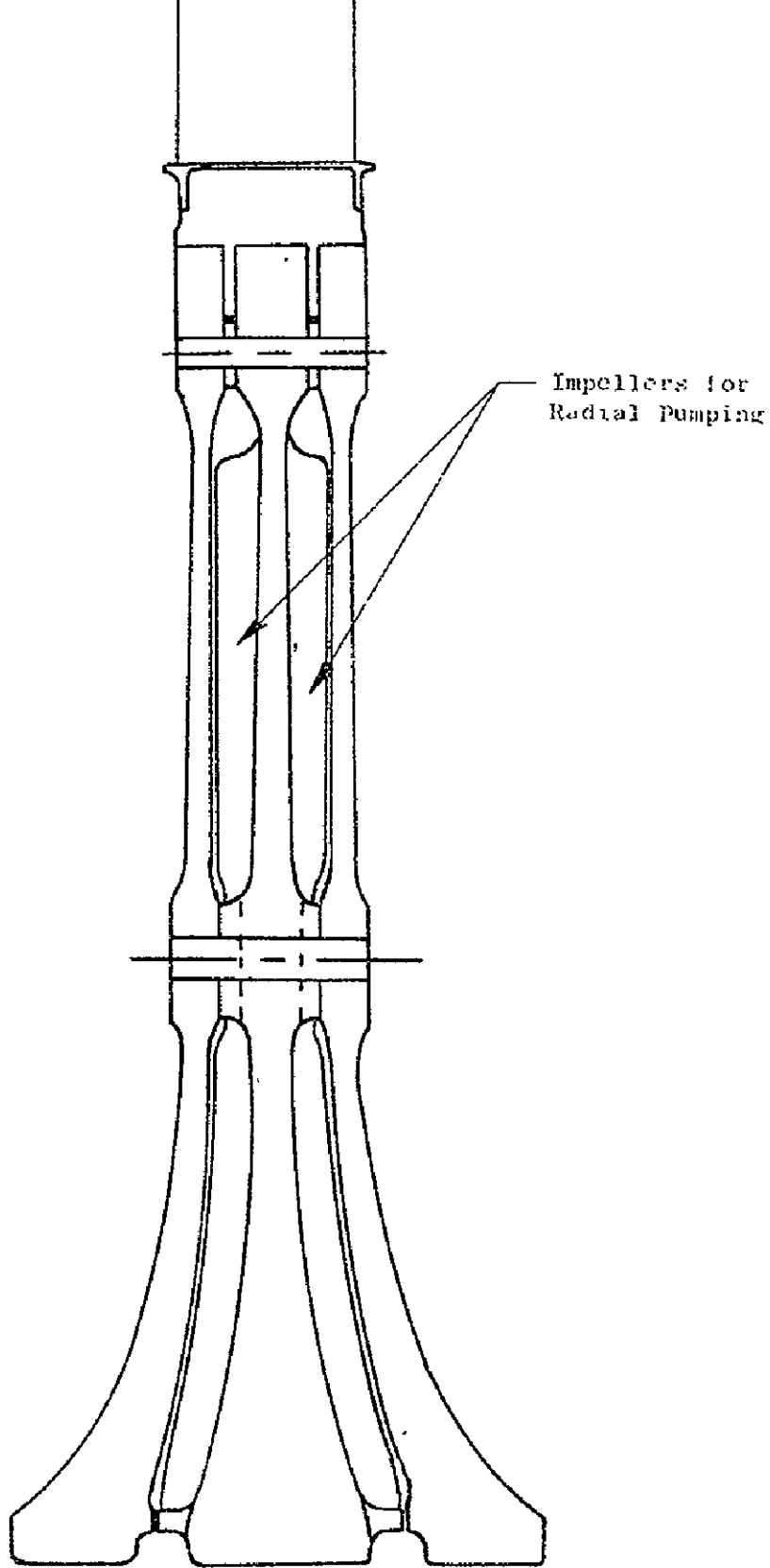


Figure 41. Three-Element Bolted Multidisk.

An analysis was also conducted on the bolt behavior in the event that an outer disk of a Bolted Multidisk configuration would fail. This revealed that the bolts alone could not support the failed disk. This led directly to consideration of the next candidate disk concept.

## 2. Splined Multidisk

This concept evolved as a way to provide the necessary area to support a failed disk in a Multidisk system. The Splined Multidisk approach is shown in Figure 42. This figure shows two disks splined together, such that if one disk fails, its tangential stress load will be transmitted through the splines to the other disk. Since this prevents the failed disk from unwrapping and failing at another point, the failure is contained with no loose fragments. This same concept could be applied as well to three or more disks.

The two disks when put together would be symmetrical, but each disk by itself would not be symmetrical about a radial line and, therefore, would have a tendency to straighten out at speed. This can be countered by radial interlocking splines, as shown in Figure 43. The Splined Multidisk is heavier than the Standard Disk, due in part to the dead weight of the splines and the weight that must be added to carry the spline weight. More weight is added when the disk is sized to carry, locally, twice the normal tangential stress because this value is developed when one disk fails (see Table XVI). However, this weight could be reduced by using more disks.

Table XVI. Splined Disk Stress Analysis Results.

	Intact	Half Failed
Bore Tangential Stress, MPa (ksi)	579 (84)	1,158 (168)
Maximum Tangential Stress, MPa (ksi)	579 (84)	1,158 (168)
Average Tangential Stress, MPa (ksi)	473 (70)	965 (140)
Dovetail Stress, MPa (ksi)	310 (45)	310 (45)
Burst Speed, rpm	15,664	11,220
Weight, kg (lb)	114.4 (252)	

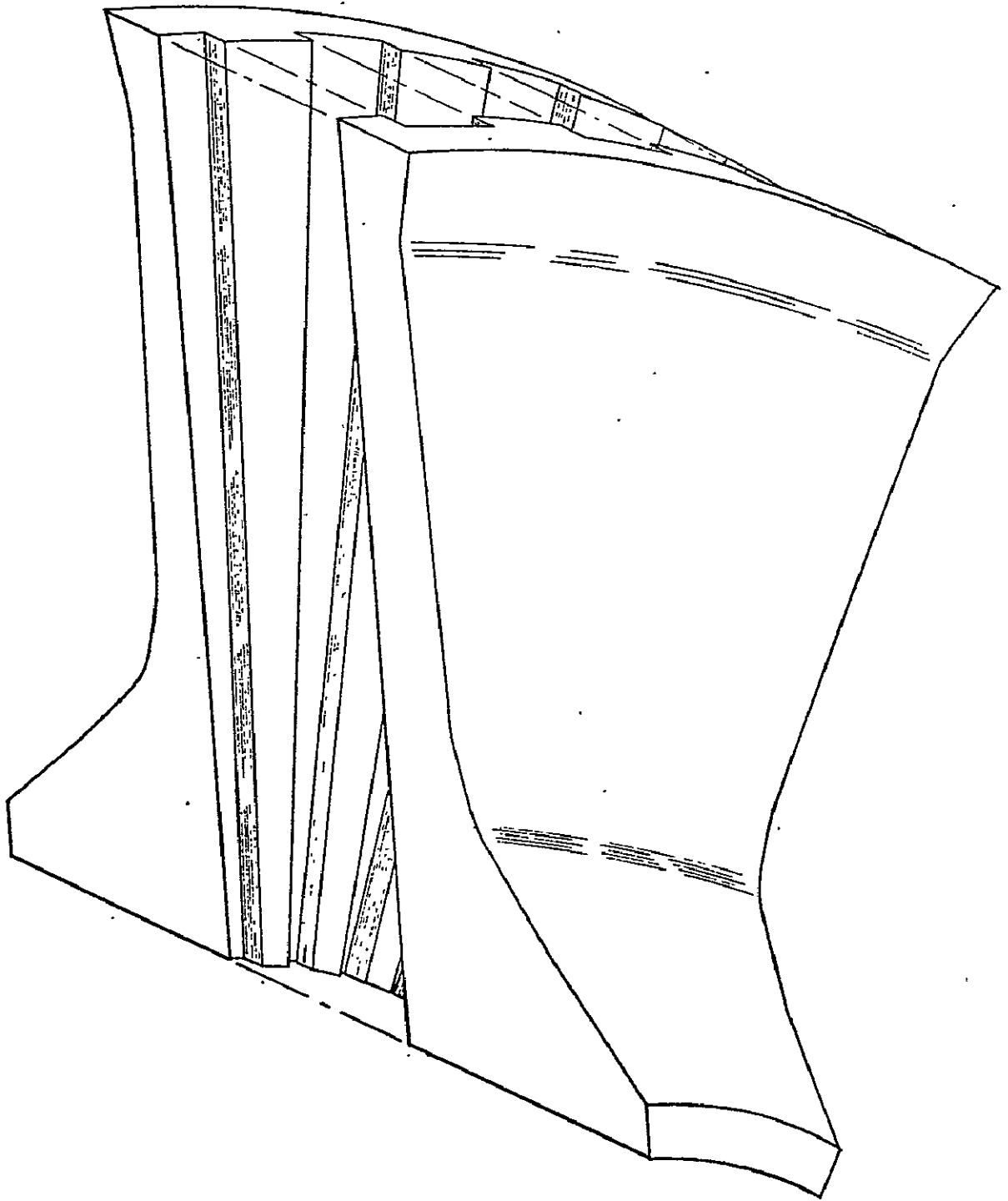


Figure 42. Splined Multidisk.

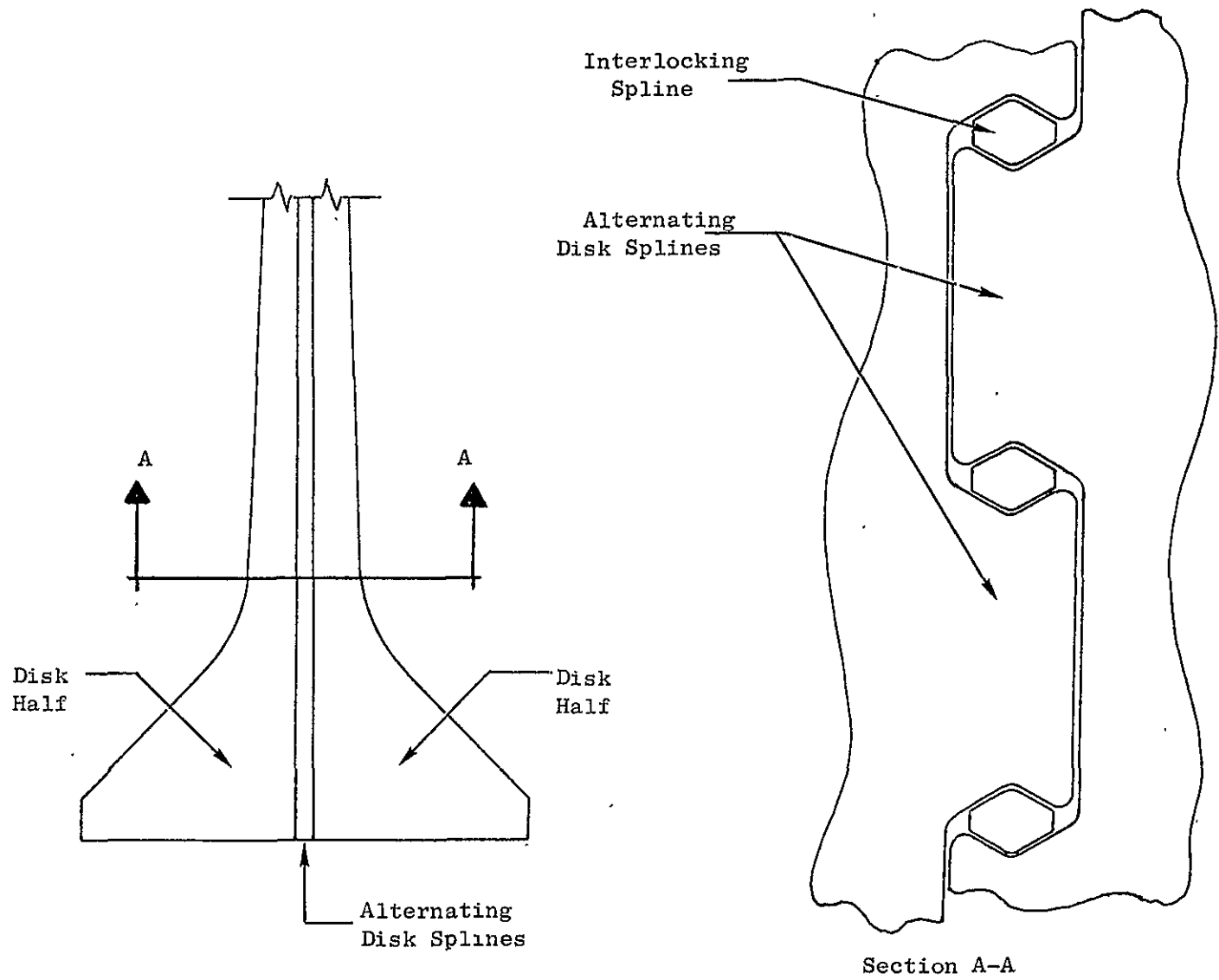


Figure 43. Splined Multidisk - Interlocking Spline Concept.

The Splined Multidisk presents a challenging design problem because of the very complex behavior of the system with one disk failed. Major questions raised are the following:

1. How is the load distributed among the splines? Does the first spline on either side of a failed section take all the load, or is it spread out to three or four splines?
2. How much out-of-plane deflection and induced stress will the disk experience due to moments induced by spline loads?
3. Will the out-of-plane bending be localized around the failed section, or will it have several maxima and minima around the circumference?

These questions are difficult to answer. However, it was felt that some of the questions could be answered in an analysis of the next candidate, the Integral Multidisk.

### 3. Integral Multidisk

The Integral Multidisk is similar to the Splined Multidisk. Here, though, instead of separate disk pieces, the entire disk is machined from a single forging. The internal cavities are formed by electrochemical machining. This leaves, as the name implies, integral ribs between the disk sections. Figure 44 shows a two-disk Multidisk of this type construction.

Earlier attempts at fabricating and testing an Integral Multidisk involved a process by which the disk sections were separately machined and then diffusion bonded together. It was discovered that the entire surface area of the joint was required to be 100 percent bonded. Anything less than a complete bond gave rise to defect sites that propagated during cyclic testing. The results of this testing shifted General Electric's approach from bonding disks together to machining integral forgings. Since then, extensive investigation into powder metallurgy development has led to successful "near-net-shape" hot isostatic pressing of disk forms. Future investigation of this technique will include "coring-in" the disk radial holes.

The Integral Multidisk concept has been shown feasible both from a manufacturing/cost standpoint and by actual testing in a development core engine at General Electric. Additionally, preliminary analysis indicated that a two-disk Integral Multidisk could be sized for redundant operation. That is, if one half of the disk would fail, the remaining half could carry it without burst. For these reasons (plus the insight that could be gained on a Splined Multidisk), the Integral Multidisk with two disk sections was chosen as the Design Disk.

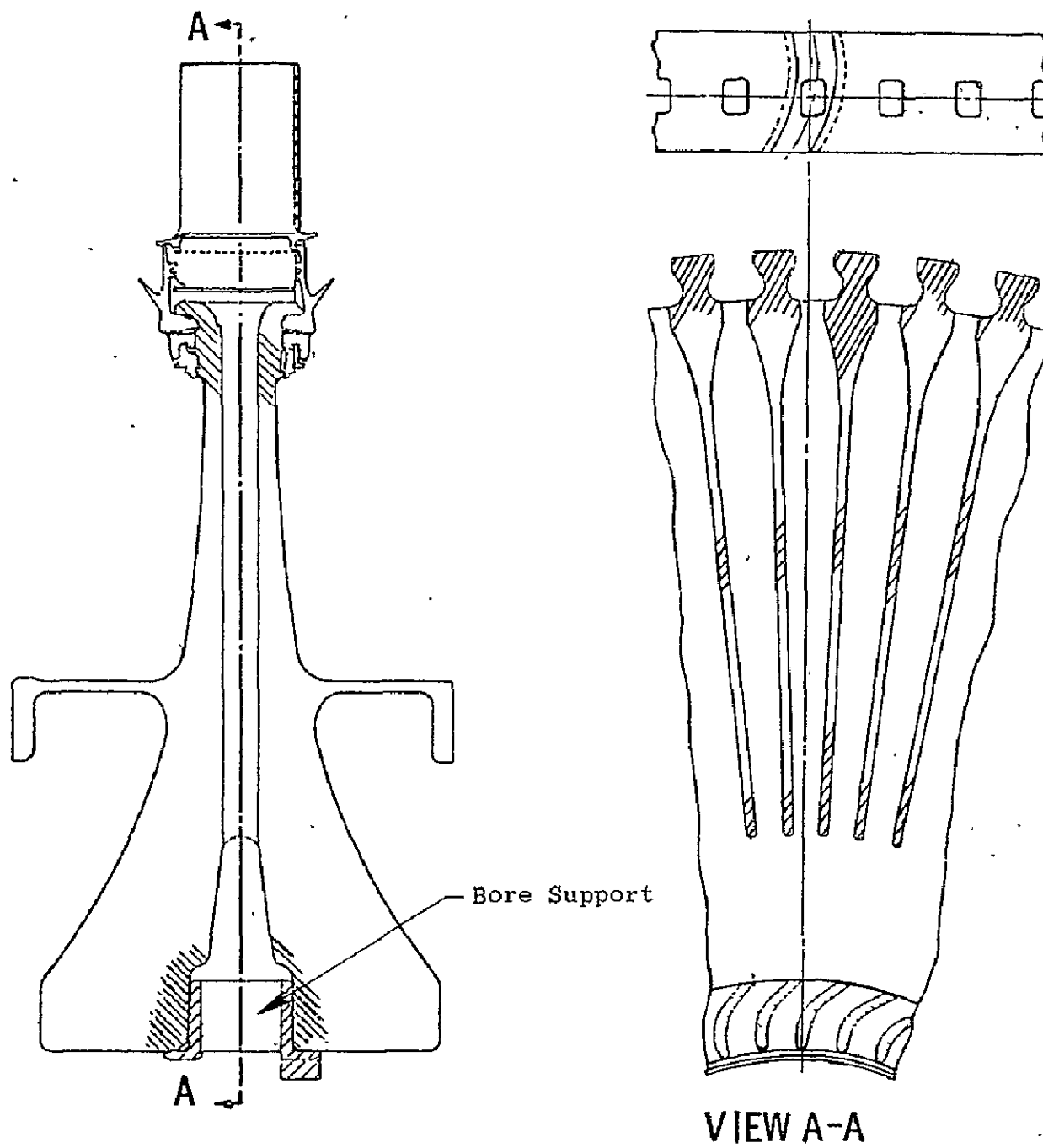


Figure 44. Intregal Multidisk.

C.2

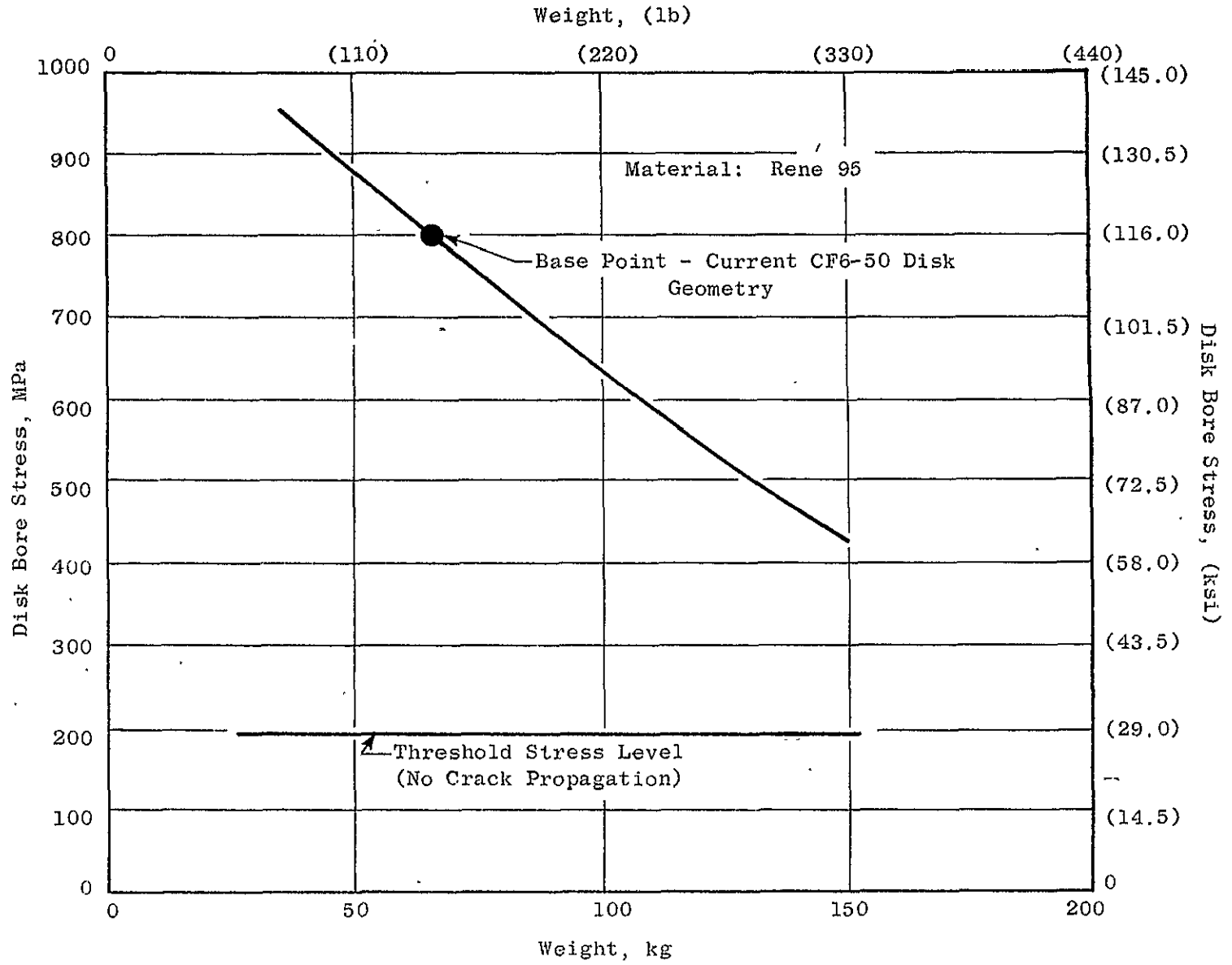


Figure 45. Advanced Standard Disk, Bore Stress Variation with Weight.

## F. Redundant Disks Versus Strengthened Standard Disks

Two different approaches can be taken to reduce the burst containment problem. First, a redundant design could be employed that would allow failure of one portion of the disk while the total load would be picked up by the remaining disk members. The alternative approach is to forestall burst by strengthening the standard-type disk with added material such that the stresses are lowered and life and overspeed capability are increased.

The sizing of the Integral Multidisk indicated a weight increase of approximately 45.4 kg (100 lb) over the Standard Disk. Several versions of the Advanced Standard Disk of varying weight were then designed to compare the relative merits of strengthening the Standard Disk.

Figure 45 shows the trend in disk weight versus bore stress for a CF6-50 disk of René 95. Also shown is the threshold stress level for René 95. This stress is the value beyond which any defect will not propagate. As can be seen, large weight penalties would be required to preclude the propagation of a bore defect. Figure 46 shows the variation of critical crack size with disk bore stress and illustrates the effect of an additional 45.4 kg (100 lb) of disk weight on the critical crack size.

However, both the LCF and the flaw propagation lives would be increased as the disk stress levels were reduced.

Thus, it is evident that the strengthened Standard Disk approach has several drawbacks. In the existing Standard Disk, the critical crack size is approximately 7.6 mm (0.3 in.); i.e., once a crack reaches that depth, it will become unstable and propagate to failure. With this small a depth, the disk stresses do not redistribute significantly in the presence of the pre-critical crack. Therefore, one assumes the same stresses for the unflawed and critically flawed disks. As the stress level in the disk drops due to weight addition, the critical crack size becomes larger to the point that redistribution of stresses does indeed become significant. Thus, although an increase in life is possible, some of the anticipated gain may not really be attainable. Adding 45.4 kg (100 lb), or 86 percent, to the Advanced Standard Disk drops its bore stress level from 793 MPa (115 ksi) to 586 MPa (85 ksi). At this condition, the life for a 6.35 mm (0.250 in.) × 2.11 mm (0.083 in.) defect at the bore becomes 4975 cycles, which is a factor of 7.5 improvement over the current Advanced Standard Disk. Here the critical crack size is approximately 10.2 mm (0.4 in.) deep. One other factor removes some of the anticipated gain in life improvement. During takeoff conditions, for example, the disk is still undergoing transient temperature response even when takeoff power is no longer needed, and a heavier disk will develop increased thermal stresses due to larger transient temperature gradients.

In summary, simply increasing the weight of a Standard Disk to drive down stress levels does not directly buy all the life improvement anticipated. Also, once a standard-type disk reaches the critical crack size state, it will burst. However, in a redundant-type design such as a Multidisk configuration, failure of one disk portion would lead to a shift in loading and increased stress levels in the remaining good disks.

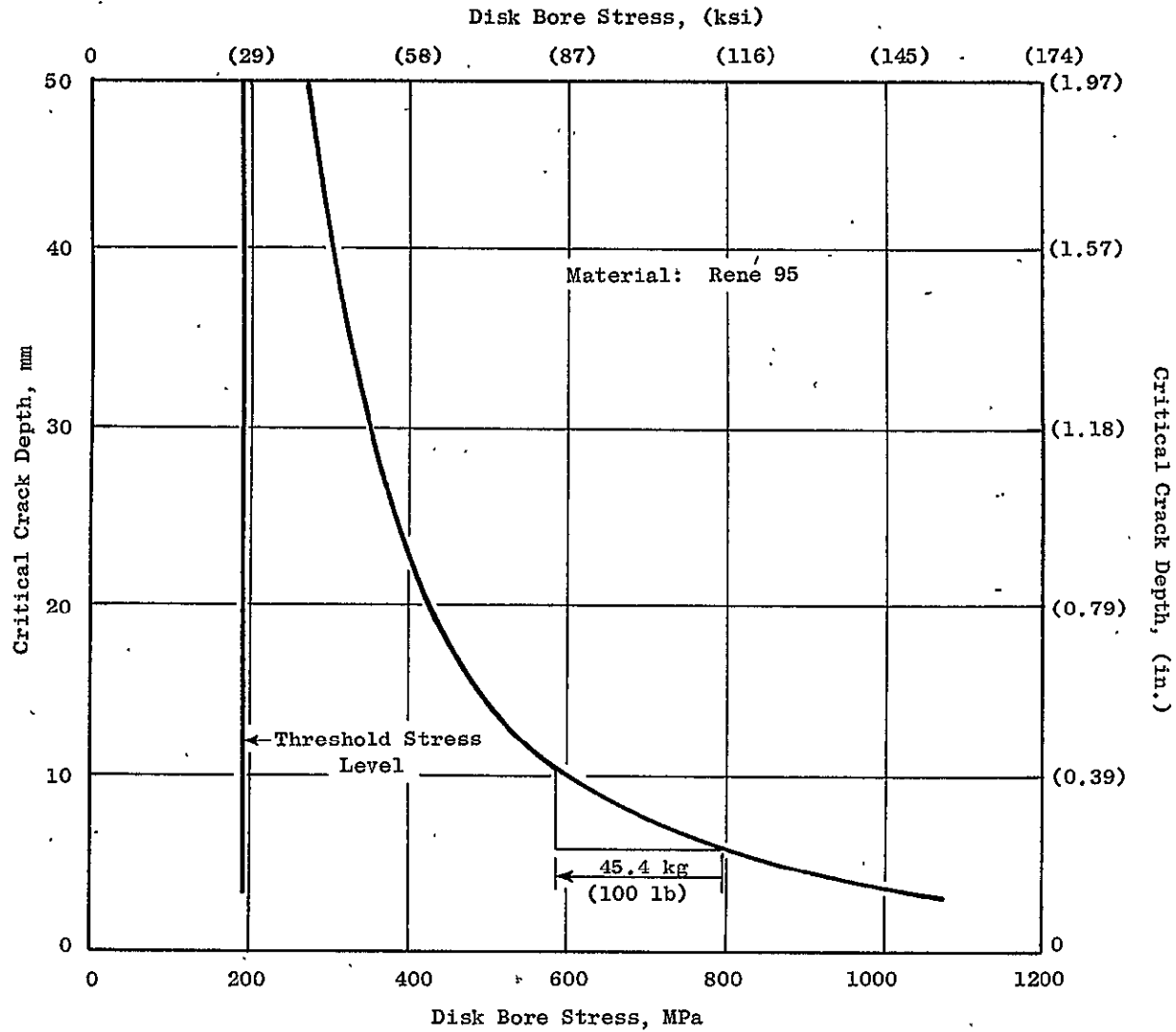


Figure 46. Advanced Standard Disk Critical Crack Size Vs. Bore Stress.

## SECTION VII

### DESIGN DISK

The Integral Multidisk was chosen as the Design Disk for further analysis under this program. As discussed previously, the most advantageous approach to forestall disk failure is to design for redundancy.

The preliminary sizing of the Design Disk was executed by making it a twin-disk redundant structure, i.e., if one side of the disk fails, the remaining half will carry it without releasing any large fragments. A simplification of this failure mode showing the load transfer from the failed disk to the intact disk is presented in Figure 47. The hoop tension present in the failed disk at the instant of failure is transferred through the connecting rib elements into the intact disk. Thus, each zone of the intact disk must carry its original load plus the transferred load. This new loading becomes cumulative through Zones 1 and 2 up to the intact disk section (Zone 3) opposite the failure point. Here the total load becomes maximum, approaching twice the "normal" load. Thus, Zone 3 must be sized (thickened) to withstand the overload. Since failure could occur at any zone, all zones must be sized to this same criterion, resulting in a heavier disk in order to prevent burst.

Figure 48 shows the live portion of the disk, i.e., minus dovetail posts, sized for redundancy. The preliminary stress distribution for this disk is shown in Figure 49.

Use of the twin disk Integral Disk design will permit future development of the necessary techniques for analysis and criteria for design that can be applied to the execution of twin- or multiple-disk spline-type designs. Higher rotational speed designs, such as those in advanced engines, will likely require a three or more disk multidisk configuration. The higher speed directly increases operational stresses. Sizing a redundant twin-disk configuration for this higher loading situation would incur a very large weight and, therefore, performance penalty if it could be accomplished at all.

#### A. Design Disk Temperature Distribution

In the transient temperature analysis for the Design Disk, temperature history was determined for the same accel/decel schedule used in the analysis of the Standard and Advanced Standard Disks. As discussed in Section IIIB, the surface temperatures of components of the CF6-50 HPT spool had been measured in actual engine operation in both transient and steady-state modes. A transient heat transfer model had been constructed for the Standard Disk and surface heat transfer coefficient boundary conditions adjusted until the calculated surface temperature response matched the engine test data. The same external heat transfer coefficients were used in the analysis of the Design Disk. Internal heat transfer boundary conditions were determined

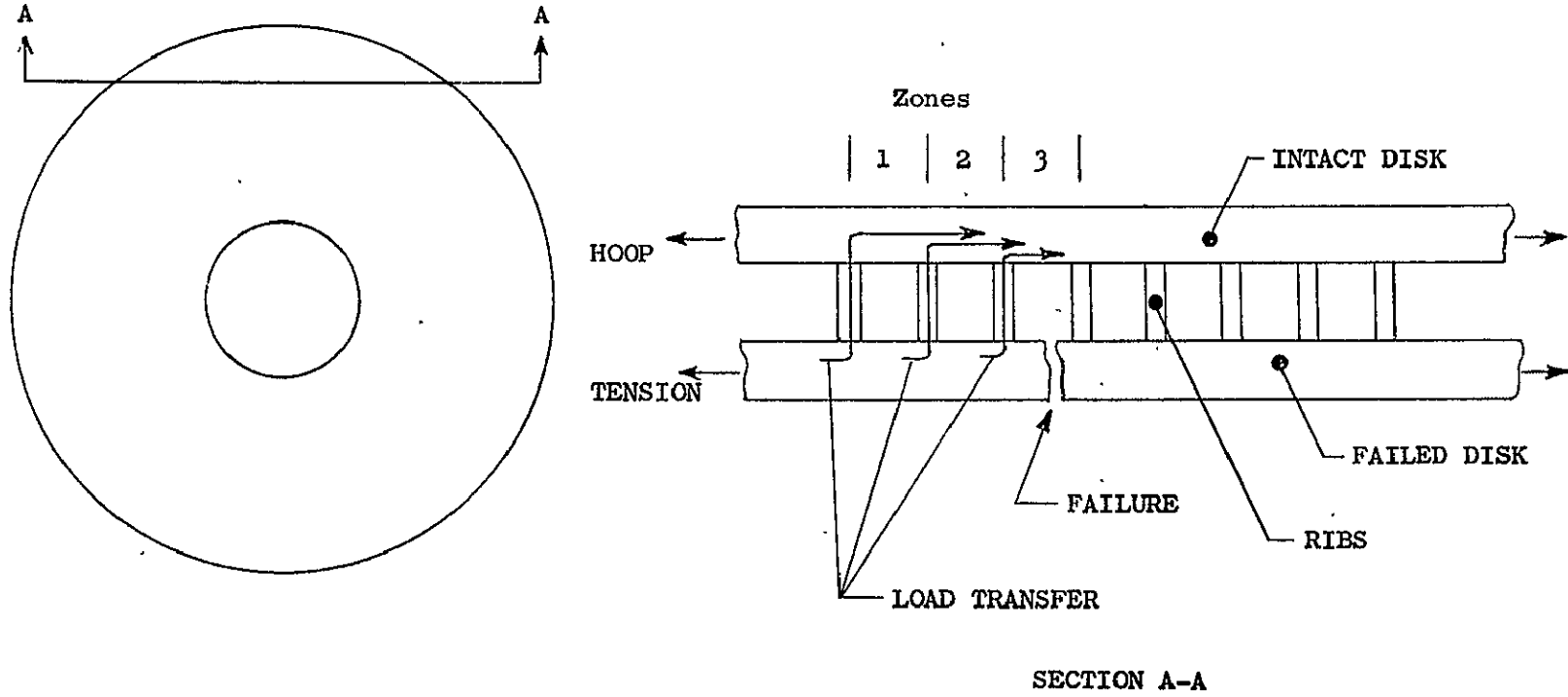


Figure 47. Schematic of Failed Design Disk Configuration.

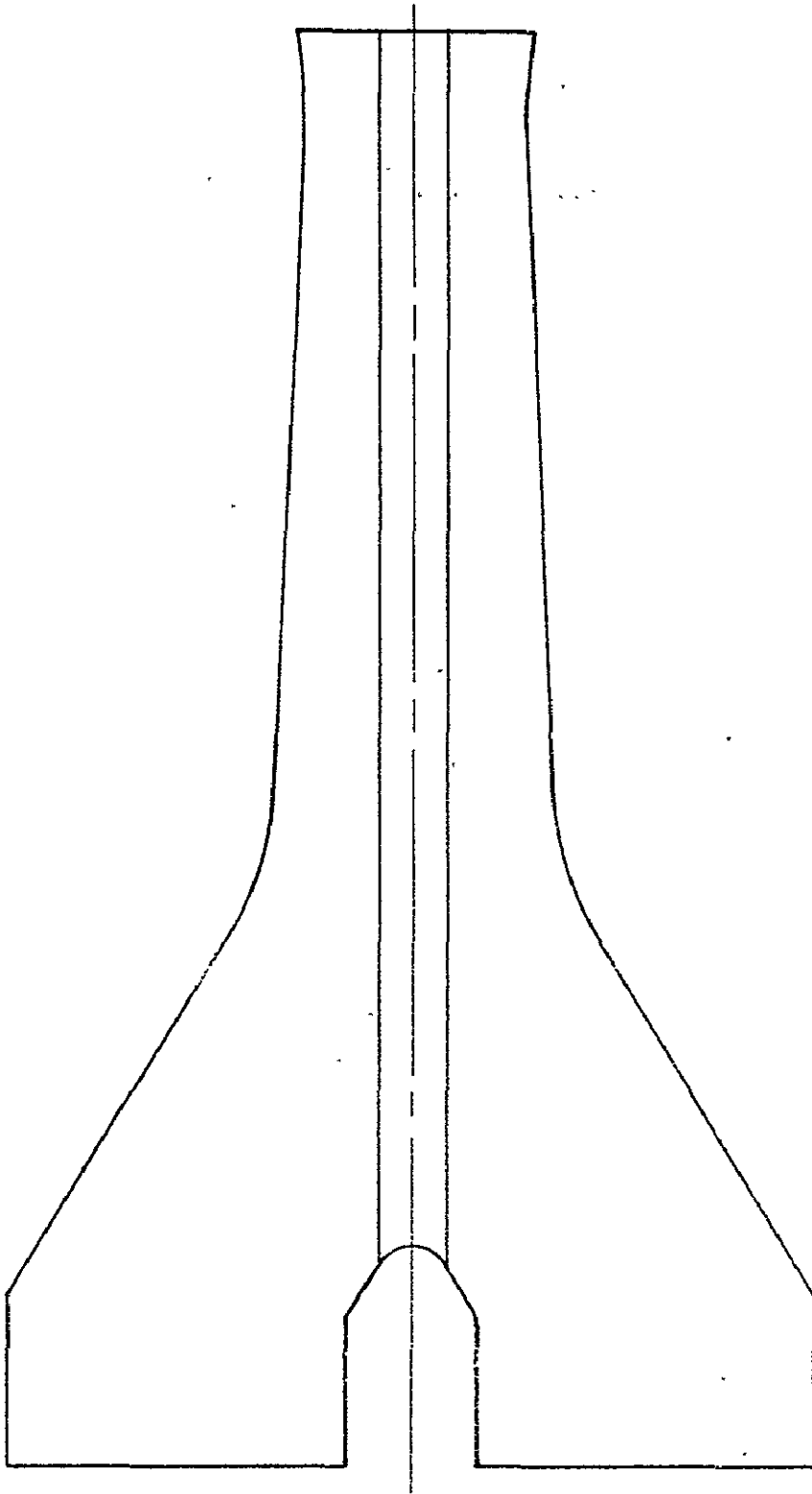


Figure 48. Initial Design Disk Configuration -  
Integral Twin Multidisk.

**ORIGINAL PAGE IS  
OF POOR QUALITY**

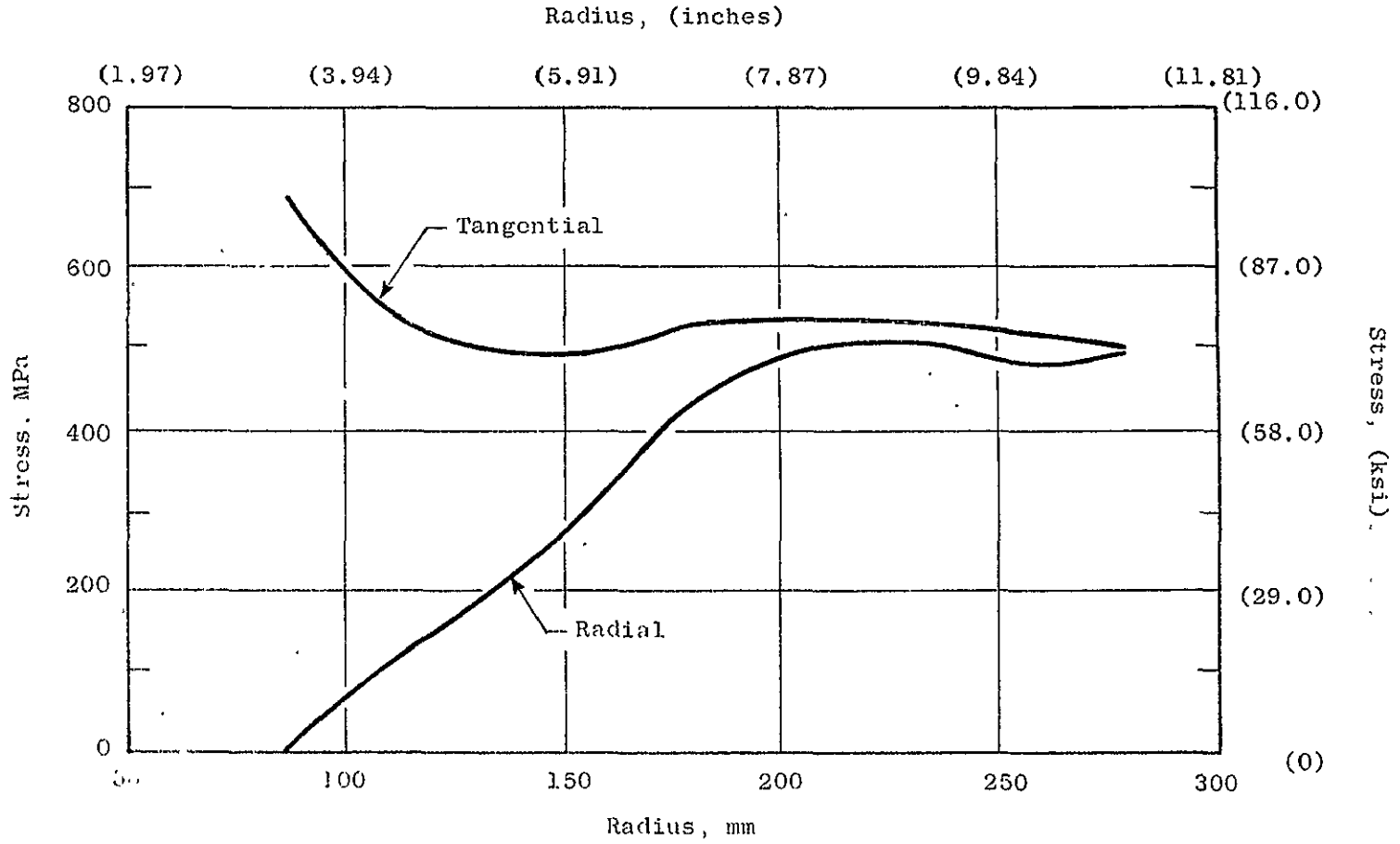


Figure 49. Design Disk Preliminary Stress Distribution.

consistent with previous General Electric experience and heat transfer prediction methods. The resulting temperature distributions for the Design Disk are shown in Figures 50 through 55. Table XVII shows a comparison of temperatures of the Standard, Advanced Standard, and Design Disks at the bore, web, and rim regions for the six flight cycle points used for analysis.

#### B. Design Disk Stress Distribution

The detailed stress analysis of the Design Disk was performed by use of the ROTOR program. The finite element model used is shown in Figure 56. Preliminary SNAP analysis of the bolt circle deflections indicated that the same shaft loading effects used on the Advanced Standard Disk should be used on the Design Disk. These boundary conditions and the Design Disk temperature distributions were input to the finite element model of the disk. Figure 57 defines the element stress and nodal deflection locations for the values presented in Tables XVIII through XXIII.

In performing the life analysis on this configuration, it was found that for propagation of an initial defect the bore region was the limiting location with one exception. The most critical location was identified to be the rib-disk interface at the bottom of the rib. Here the concentration effect of the cooling passage degraded the life.

Since the life for a defect in the bore region could be improved only by the addition of more weight (i.e., there were no concentrations or other modifying effects to alter this life), the bore life was accepted as it was, and a redesign was undertaken to improve the only life that fell below this value, that of the rib-disk intersection.

The redesign addressed two possible avenues of life improvement in this region. One was a recontouring of the cooling air passage to achieve a lower stress concentration. The second was to raise the bottom of the rib to a higher radius where the driving stresses in the disk would be lower. Both of these improvements were incorporated into the design.

An engineering drawing of the improved (high rib) configuration of the Design Disk is presented in Figure 58.

The ROTOR model was modified for these changes and rerun for the two life limiting points in the flight cycle, Climb and Thrust Reverse. Figure 59 defines the stress and deflection comparison points for these two configurations as listed in Tables XXIV and XXV. The resulting lives for this "high rib" design are discussed in Section VII E, which follows.

#### C. Design Disk Weight

The Design Disk is inherently heavier than the standard or Advanced Standard Disk due to its unique design for redundancy. This feature puts the Design Disk at 111.7 kg (246 lb) as compared to 67.2 kg (148 lb) for the Standard Disk.

Standard Day  
Temperatures in  $^{\circ}\text{K}$  ( $^{\circ}\text{F}$ ).

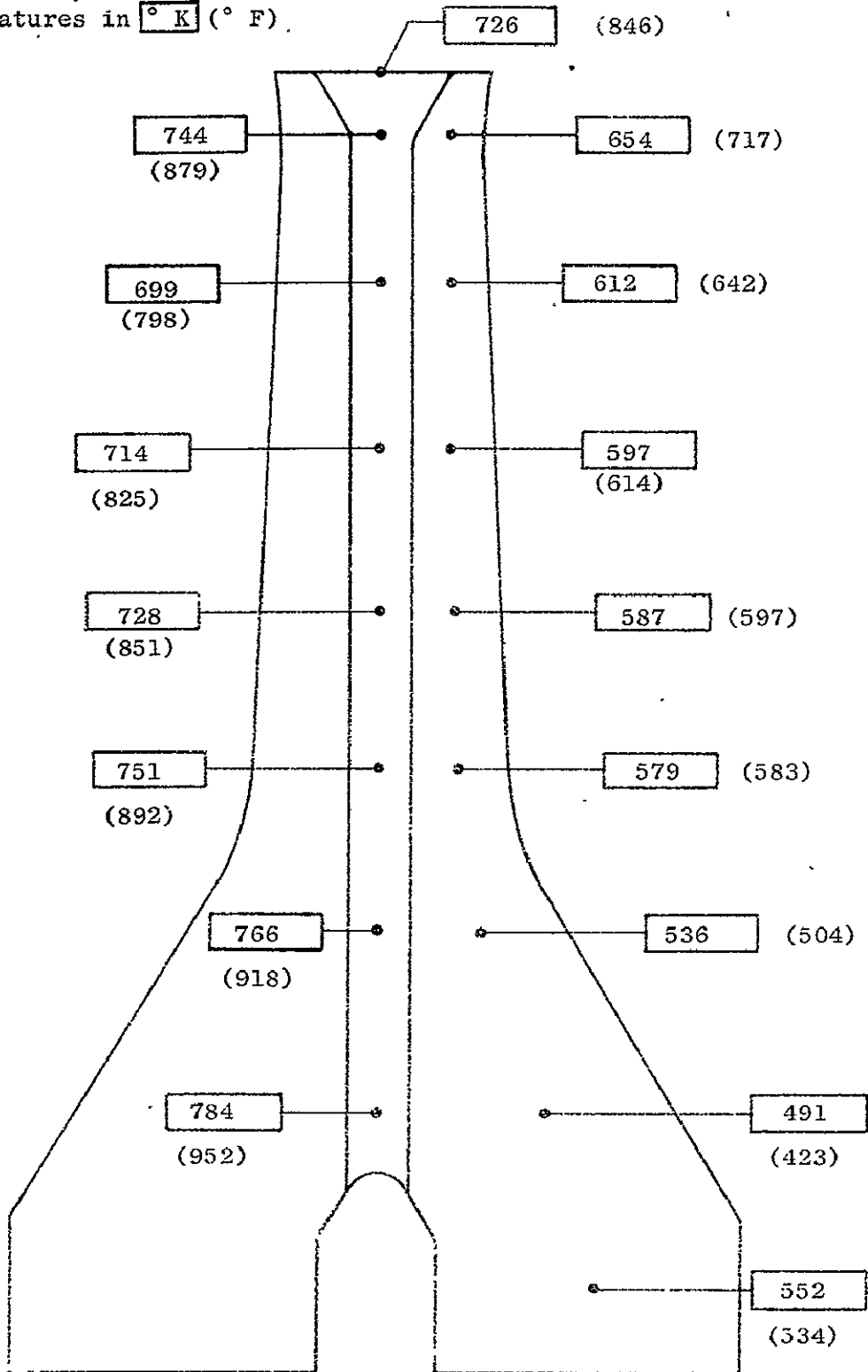


Figure 50. Design Disk Metal Temperatures at Takeoff 1 Conditions.

Standard Day  
Temperatures in  $^{\circ}\text{K}$  ( $^{\circ}\text{F}$ )

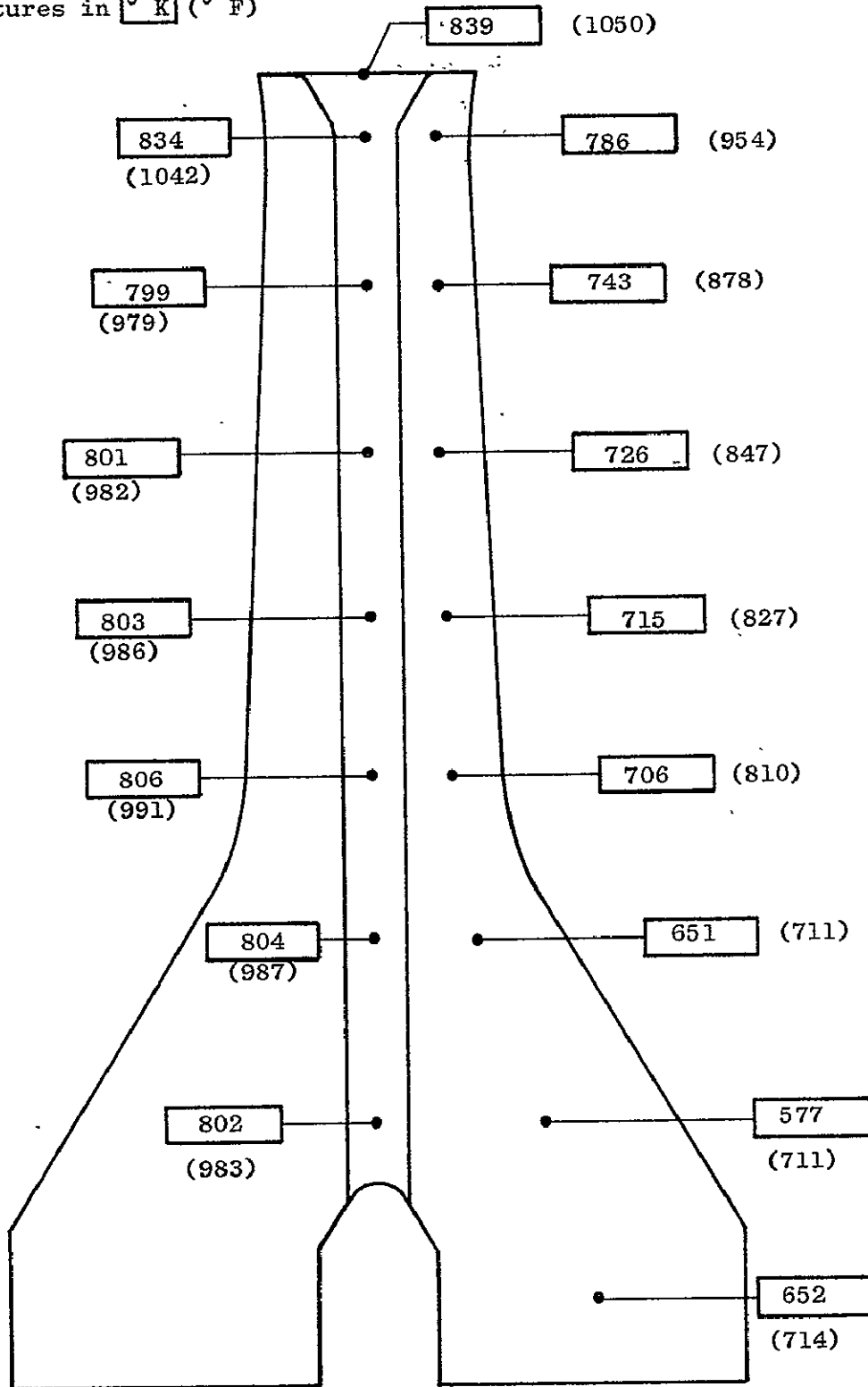


Figure 51. Design Disk Metal Temperatures at Takeoff 2 Conditions.

Standard Day  
 Temperatures in  $^{\circ}\text{K}$  ( $^{\circ}\text{F}$ )

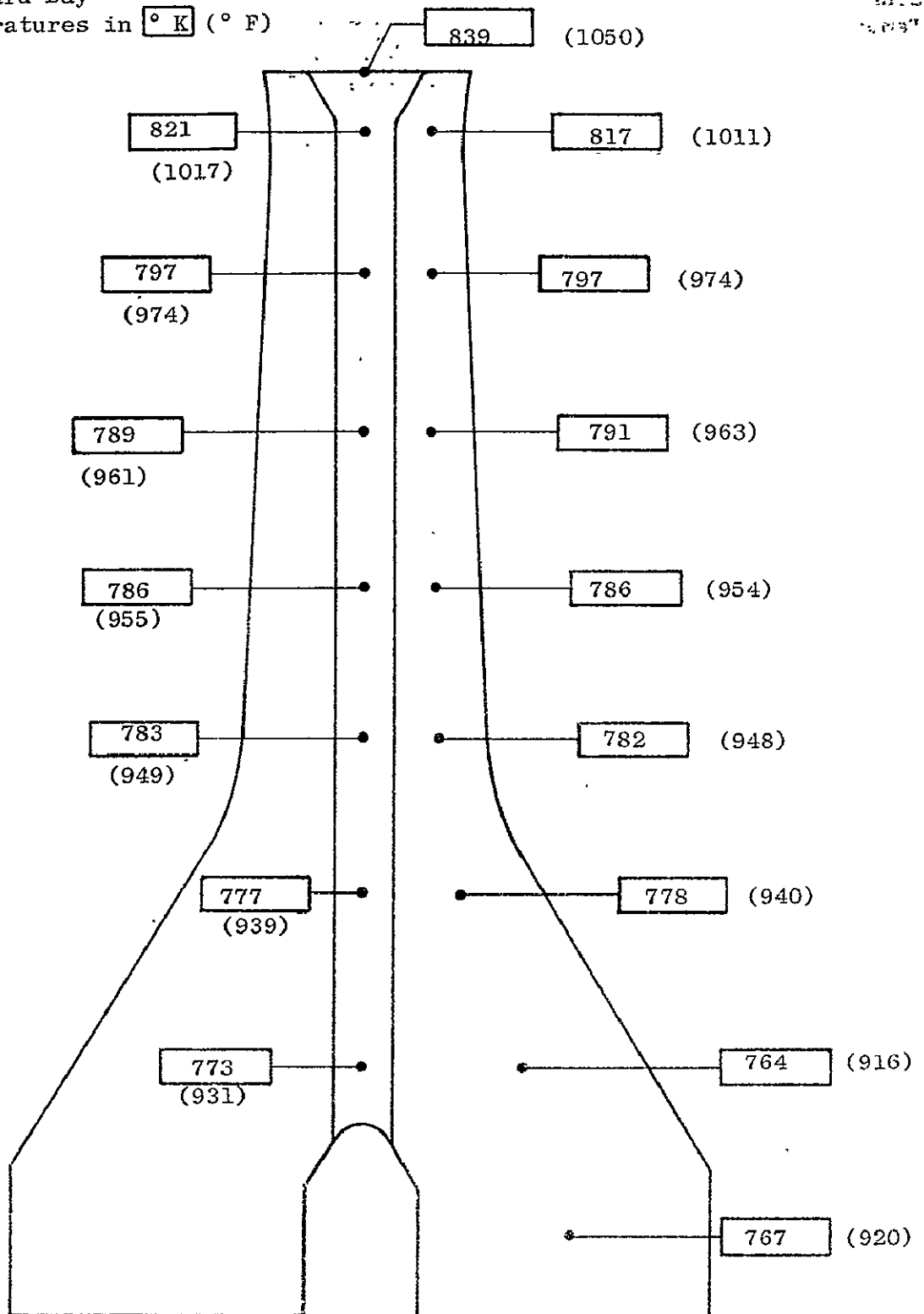


Figure 52. Design Disk Metal Temperatures at Maximum Climb Conditions.

Standard Day  
Temperatures in  $^{\circ}\text{K}$  ( $^{\circ}\text{F}$ )

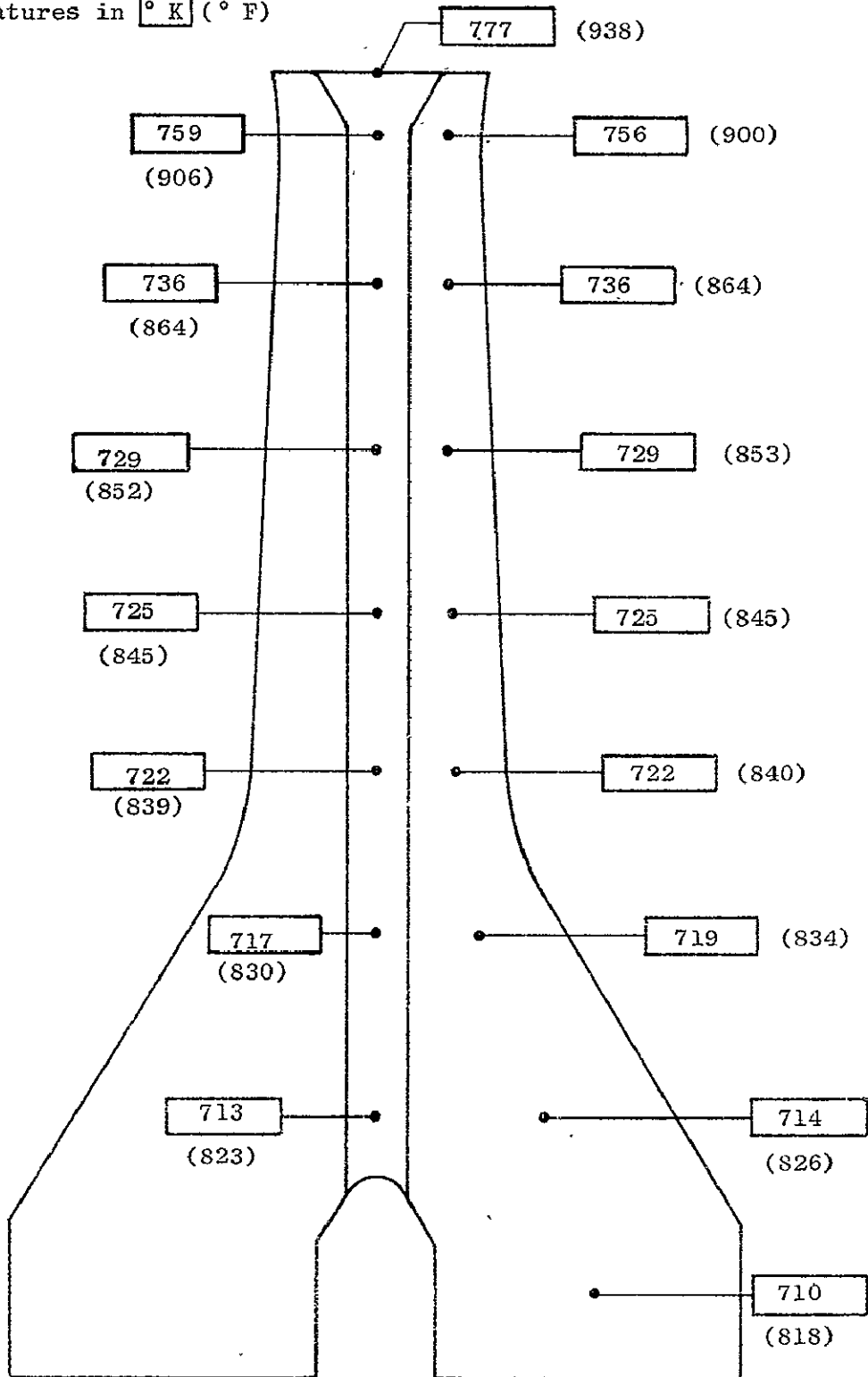


Figure 53. Design Disk Metal Temperatures at Cruise Conditions.

Standard Day  
Temperatures in  $^{\circ}\text{K}$  ( $^{\circ}\text{F}$ )

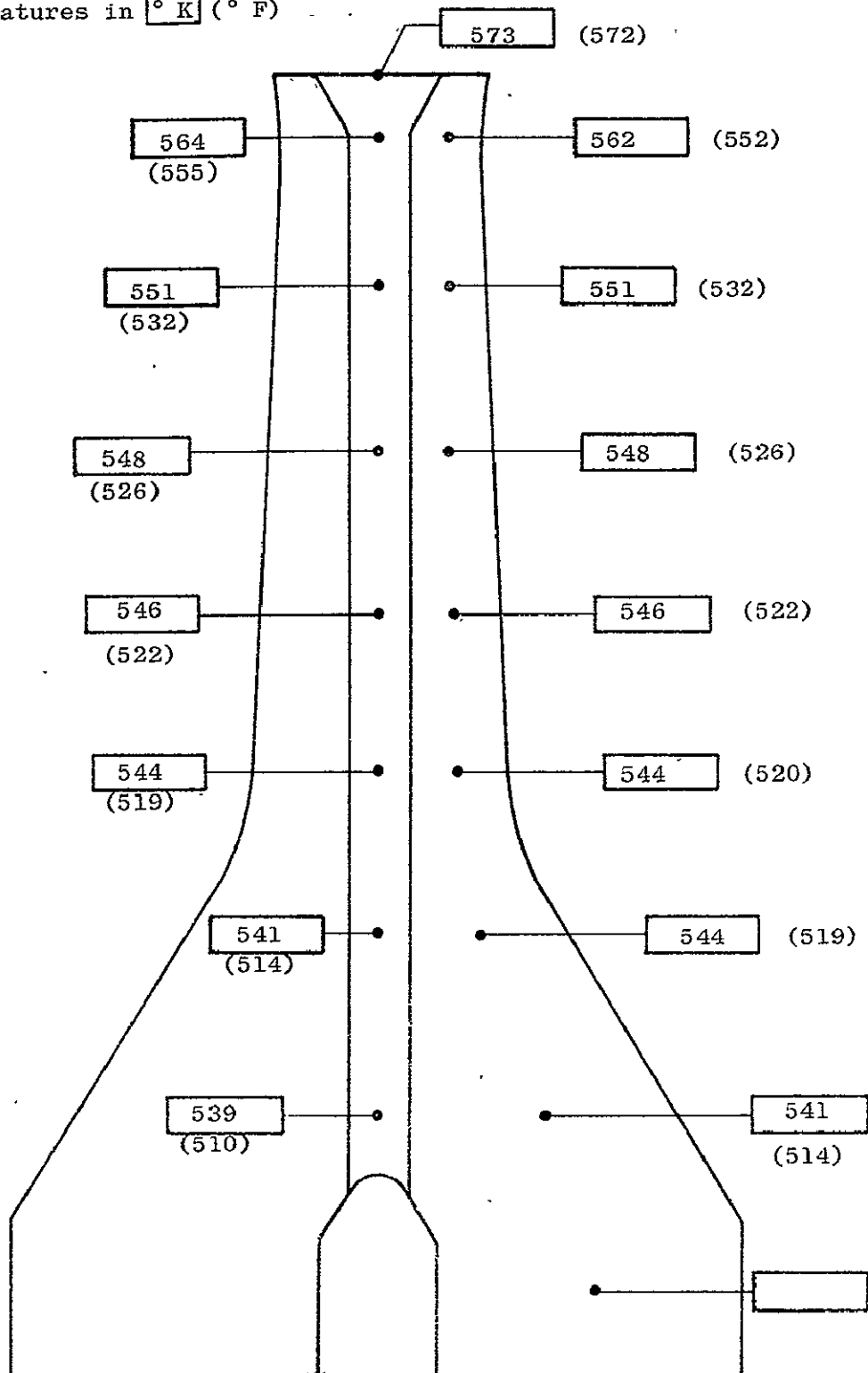


Figure 54. Design Disk Metal Temperatures at Flight Idle Conditions.

Standard Day  
 Temperatures in  $^{\circ}\text{K}$  ( $^{\circ}\text{F}$ )

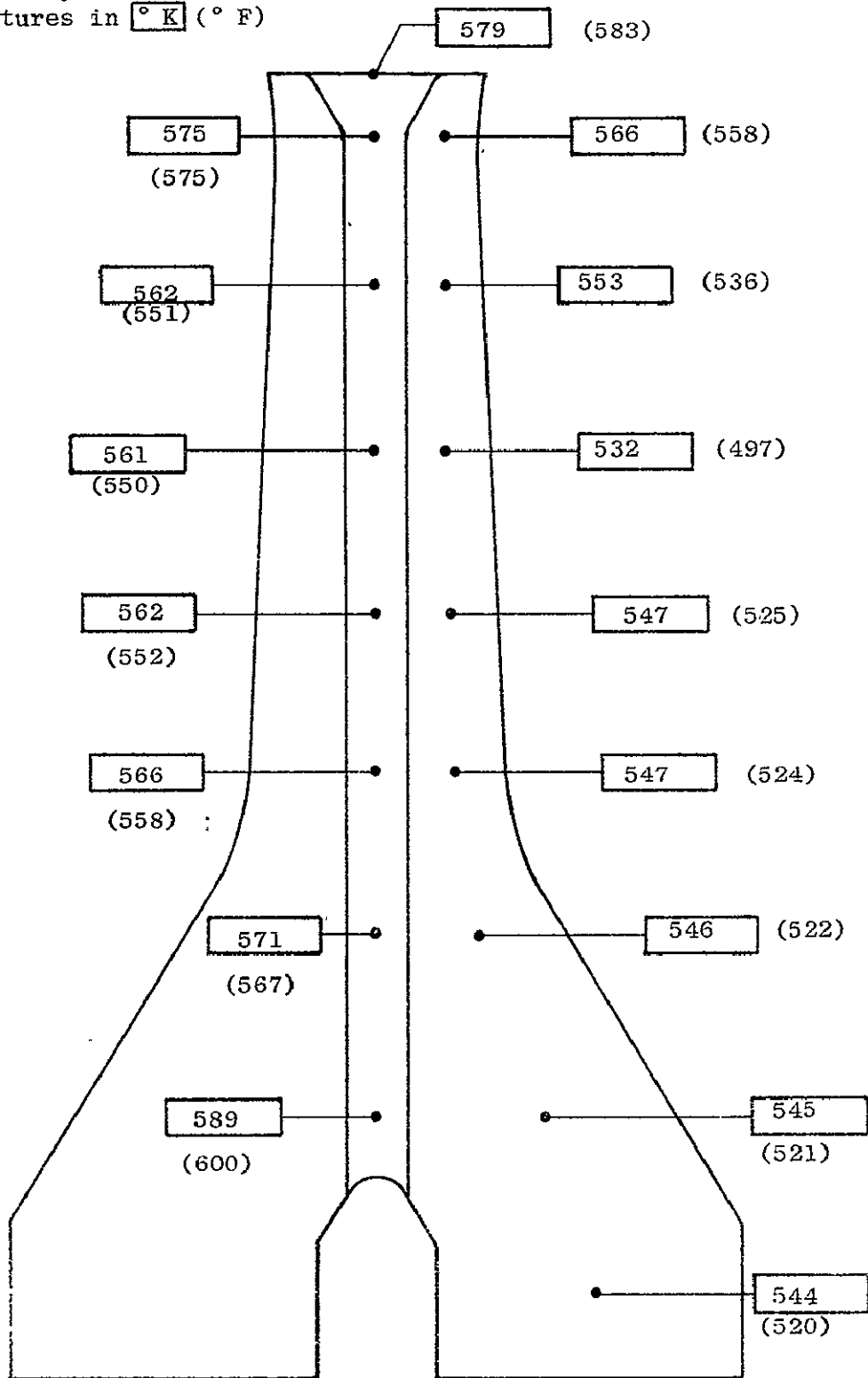


Figure 55. Design Disk Metal Temperatures at Thrust Reverse Conditions.

Table XVII. Temperature Comparison: Standard Disk Versus Advanced Standard Disk Versus Design Disk.

	Flight Condition					
	Takeoff 1	Takeoff 2	Max. Climb	Cruise	Flight Idle	Thrust Reverse
	Standard Day Temperatures in ° K (° F)					
Bore (a)	581 (585)	700 (800)	769 (925)	712 (822)	551 (531)	553 (535)
(b)	563 (553)	681 (766)	769 (924)	714 (825)	556 (540)	558 (544)
(c)	579 (583)	685 (773)	768 (922)	708 (815)	540 (512)	544 (519)
Web* (a)	576 (578)	700 (800)	783 (950)	728 (850)	565 (557)	566 (559)
(b)	560 (548)	681 (766)	783 (950)	729 (853)	571 (568)	573 (571)
(c)	551 (532)	670 (746)	779 (943)	719 (835)	544 (519)	546 (523)
Rim (a)	754 (897)	824 (1023)	803 (986)	742 (875)	554 (538)	590 (602)
(b)	737 (866)	818 (1013)	803 (985)	742 (875)	554 (538)	585 (593)
(c)	726 (846)	839 (1050)	839 (1050)	777 (938)	573 (572)	579 (583)

(a) Standard Disk

(b) Advanced Standard Disk

(c) Design Disk

\* R = 168.9 mm (6.65 in.)

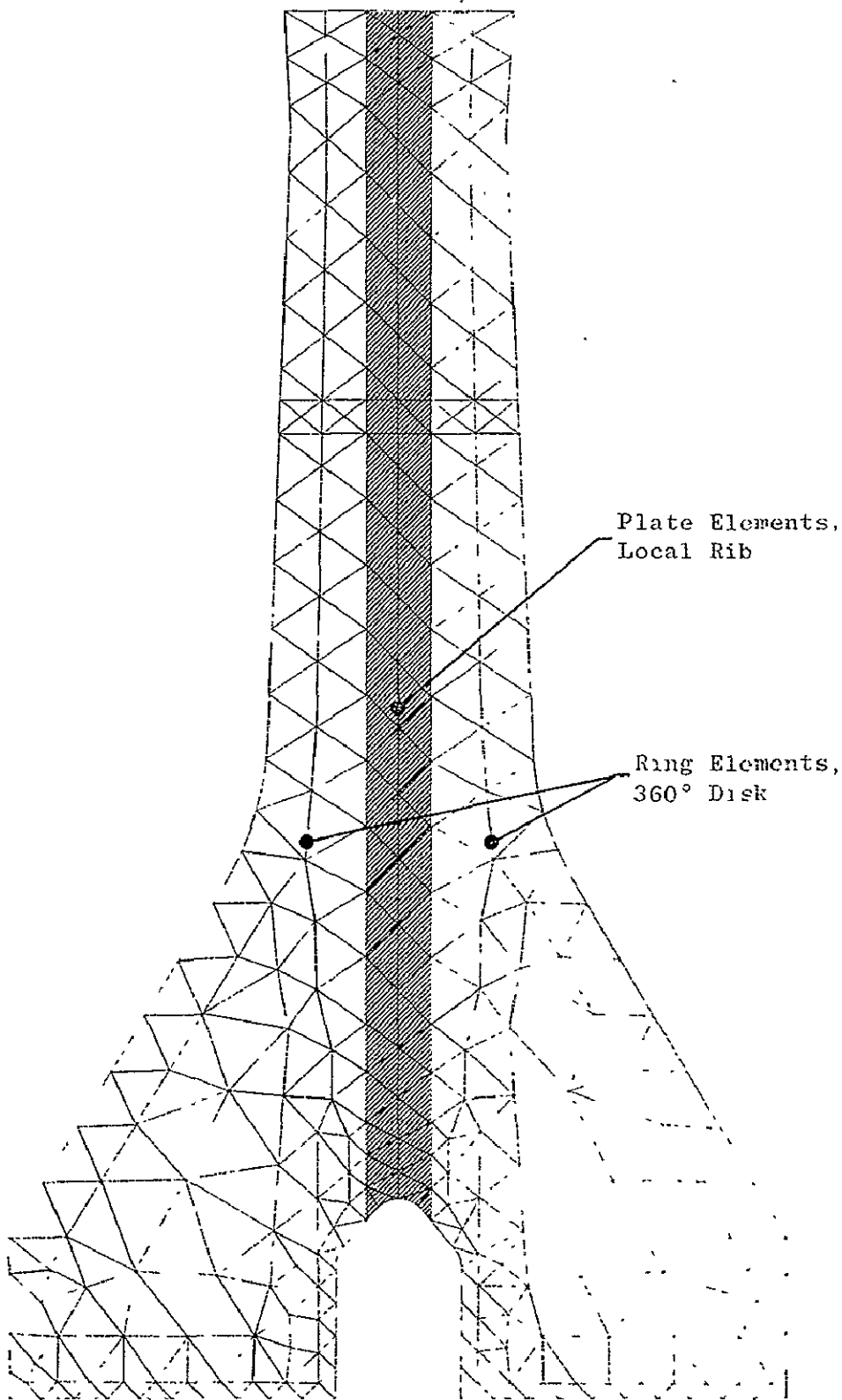


Figure 56. Initial Design Disk ROTOR Model.

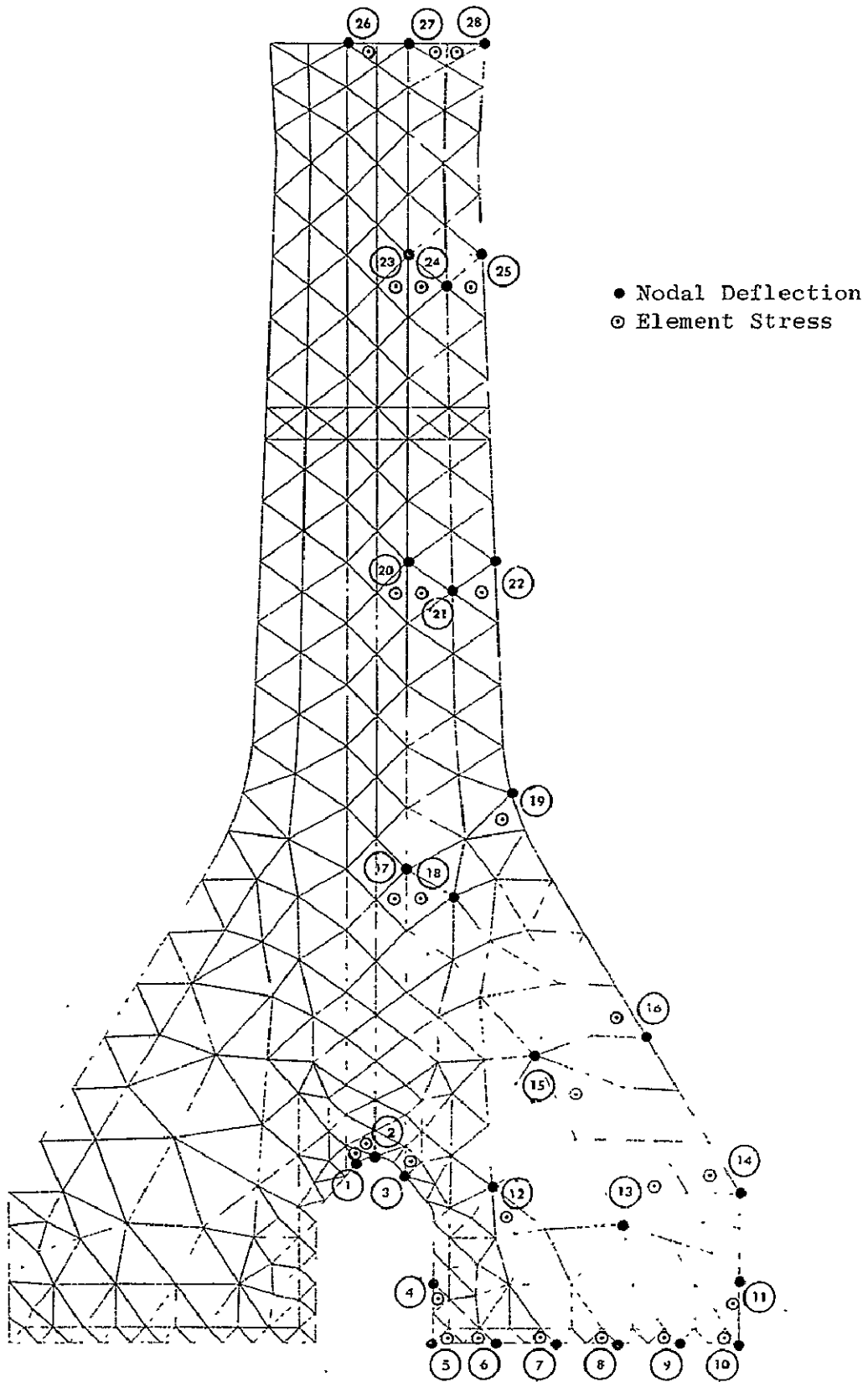


Figure 57. Initial Design Disk Stress and Deflection Locations.

Table XVIII. Initial Design Disk Stress and Deflection Distribution at Takeoff 1 Conditions.

Location	Radial Stress		Tangential Stress		Radial Deflection	
	MPa	ksi	MPa	ksi	mm	in.
1	-55	-8	-	-	0.71	0.028
2	-41	-6	-	-	0.74	0.029
3	131	19	724	105	0.71	0.028
4	159	23	696	101	0.66	0.026
5	110	16	676	98	0.61	0.024
6	28	4	641	93	0.64	0.025
7	7	1	655	95	0.61	0.024
8	0	0	662	96	0.61	0.024
9	-7	-1	676	98	0.61	0.024
10	0	0	696	101	0.61	0.024
11	34	5	689	100	0.64	0.025
12	165	24	710	103	0.71	0.028
13	103	15	662	96	0.66	0.026
14	55	8	648	94	0.69	0.027
15	517	75	607	88	0.74	0.029
16	172	25	593	86	0.74	0.029
17	248	36	-	-	0.89	0.035
18	448	65	621	90	0.86	0.034
19	648	94	600	87	0.89	0.035
20	372	54	-	-	1.14	0.045
21	524	76	483	70	1.12	0.044
22	538	78	490	71	1.14	0.045
23	317	46	-	-	1.42	0.056
24	448	65	407	59	1.40	0.055
25	441	64	407	59	1.42	0.056
26	179	26	-	-	1.65	0.065
27	338	49	62	9	1.65	0.065
28	372	54	97	14	1.65	0.065

Table XIX. Initial Design Disk Stress and Deflection  
Distribution at Takeoff 2 Conditions.

Location	Radial Stress		Tangential Stress		Radial Deflection	
	MPa	ksi	MPa	ksi	mm	in.
1	55	-8	-	-	0.89	0.035
2	55	-8	-	-	0.89	0.035
3	138	20	758	110	0.89	0.035
4	165	24	689	100	0.81	0.032
5	103	15	648	94	0.76	0.030
6	28	4	621	90	0.76	0.030
7	7	1	627	91	0.76	0.030
8	7	1	641	93	0.74	0.029
9	-7	-1	662	96	0.74	0.029
10	0	0	683	99	0.74	0.029
11	34	5	683	99	0.79	0.031
12	172	25	724	105	0.86	0.034
13	97	14	683	99	0.81	0.032
14	48	7	669	97	0.84	0.033
15	262	38	752	109	0.94	0.037
16	145	21	586	85	0.91	0.036
17	269	39	-	-	1.12	0.044
18	655	95	552	80	1.09	0.043
19	462	67	586	85	1.19	0.047
20	372	54	-	-	1.50	0.059
21	517	75	427	62	1.45	0.057
22	530	77	427	62	1.50	0.059
23	324	47	-	-	1.88	0.074
24	434	63	352	51	1.83	0.072
25	427	62	352	51	1.88	0.074
26	172	25	-	-	2.16	0.085
27	324	47	48	7	2.16	0.085
28	352	51	76	11	2.16	0.085

Table XX. Initial Design Disk Stress and Deflection Distribution at Maximum Climb Conditions.

Location	Radial Stress		Tangential Stress		Radial Deflection	
	MPa	ksi	MPa	ksi	mm	in.
1	-55	-8	-	-	1.09	0.043
2	-41	-6	-	-	1.09	0.043
3	110	16	600	87	1.07	0.042
4	152	22	724	105	0.97	0.038
5	117	17	758	110	0.91	0.036
6	34	5	731	106	0.91	0.036
7	14	2	731	106	0.89	0.035
8	7	1	724	105	0.89	0.035
9	7	1	717	104	0.86	0.034
10	7	1	710	103	0.86	0.034
11	41	6	662	96	0.91	0.036
12	159	23	641	93	1.07	0.042
13	124	18	565	82	0.99	0.039
14	69	10	531	77	1.02	0.040
15	207	30	552	80	1.19	0.047
16	214	31	490	71	1.17	0.046
17	186	27	-	-	1.42	0.056
18	359	52	531	77	1.40	0.055
19	558	81	572	83	1.50	0.059
20	296	43	-	-	1.83	0.072
21	455	66	496	72	1.78	0.070
22	462	67	503	73	1.83	0.072
23	248	36	-	-	2.24	0.088
24	386	56	434	63	2.21	0.087
25	393	57	434	63	2.24	0.088
26	131	19	-	-	2.51	0.099
27	296	43	269	39	2.54	0.100
28	400	58	441	64	2.51	0.099

Table XXI. Initial Design Disk Stress and Deflection Distribution at Cruise Conditions.

Location	Radial Stress		Tangential Stress		Radial Deflection	
	MPa	ksi	MPa	ksi	mm	in.
1	-	-	-	-	0.97	0.038
2	-48	-7	-	-	0.97	0.038
3	-41	-6	-	-	0.94	0.037
4	138	20	676	98	0.84	0.033
5	110	16	710	103	0.79	0.031
6	34	5	683	99	0.79	0.031
7	14	2	683	99	0.79	0.031
8	7	1	676	98	0.79	0.031
9	7	1	669	97	0.76	0.030
10	7	1	655	95	0.76	0.030
11	34	5	607	88	0.81	0.032
12	145	21	586	85	0.94	0.037
13	117	17	517	75	0.86	0.034
14	69	10	476	69	0.89	0.035
15	186	27	490	71	1.04	0.041
16	207	30	448	65	1.04	0.041
17	165	24	-	-	1.24	0.049
18	324	47	496	72	1.22	0.048
19	510	74	531	77	1.32	0.052
20	269	39	-	-	1.60	0.063
21	421	61	469	68	1.57	0.062
22	427	62	469	68	1.60	0.063
23	234	34	-	-	1.96	0.077
24	359	52	407	59	1.93	0.076
25	365	53	407	59	1.96	0.077
26	124	18	-	-	2.21	0.087
27	283	41	248	36	2.21	0.087
28	303	44	269	39	2.21	0.087

Table XXII. Initial Design Disk Stress and Deflection Distribution at Flight Idle Conditions.

Location	Radial Stress		Tangential Stress		Radial Deflection	
	MPa	ksi	MPa	ksi	mm	in.
1	-34	-5	-	-	0.56	0.022
2	-28	-4	-	-	0.58	0.023
3	69	10	359	52	0.56	0.022
4	90	13	441	64	0.51	0.020
5	69	10	469	68	0.48	0.019
6	21	3	448	65	0.48	0.019
7	7	1	448	65	0.46	0.018
8	7	1	448	65	0.46	0.018
9	7	1	441	64	0.46	0.018
10	7	1	434	63	0.46	0.018
11	28	4	400	58	0.48	0.019
12	90	13	386	56	0.53	0.021
13	83	12	338	49	0.51	0.020
14	48	7	317	46	0.51	0.020
15	124	18	324	47	0.61	0.024
16	138	20	303	44	0.61	0.024
17	110	16	-	-	0.74	0.029
18	214	31	338	49	0.71	0.028
19	338	49	365	53	0.76	0.030
20	179	26	-	-	0.91	0.036
21	276	40	317	46	0.91	0.036
22	283	41	324	47	0.94	0.037
23	152	22	-	-	1.14	0.045
24	241	35	283	41	1.12	0.044
25	241	35	283	41	1.14	0.045
26	76	11	-	-	1.27	0.050
27	186	27	193	28	1.27	0.050
28	200	29	207	30	1.27	0.050

Table XXIII. Initial Design Disk Stress and Deflection Distribution at Thrust Reverse Conditions.

Location	Radial Stress		Tangential Stress		Radial Deflection	
	MPa	ksi	MPa	ksi	mm	in.
1	-48	-7	-	-	0.69	0.027
2	-34	-5	-	-	0.69	0.027
3	103	15	558	81	0.69	0.027
4	152	22	689	100	0.61	0.024
5	117	17	717	104	0.58	0.023
6	34	5	689	100	0.58	0.023
7	14	2	689	100	0.58	0.023
8	7	1	689	100	0.58	0.023
9	7	1	683	99	0.56	0.022
10	7	1	676	98	0.56	0.022
11	34	5	627	91	0.58	0.023
12	145	21	607	88	0.66	0.026
13	124	18	538	78	0.64	0.025
14	69	10	503	73	0.61	0.024
15	193	28	517	75	0.71	0.028
16	214	31	476	69	0.71	0.028
17	172	25	-	-	0.86	0.034
18	345	50	531	77	0.86	0.034
19	531	77	572	83	0.89	0.035
20	276	40	-	-	1.07	0.042
21	441	64	503	73	1.07	0.042
22	455	66	510	74	1.09	0.043
23	241	35	-	-	1.30	0.051
24	386	56	462	67	1.27	0.050
25	455	66	510	74	1.30	0.051
26	131	19	-	-	1.45	0.057
27	310	45	331	48	1.45	0.057
28	331	48	352	51	1.47	0.058





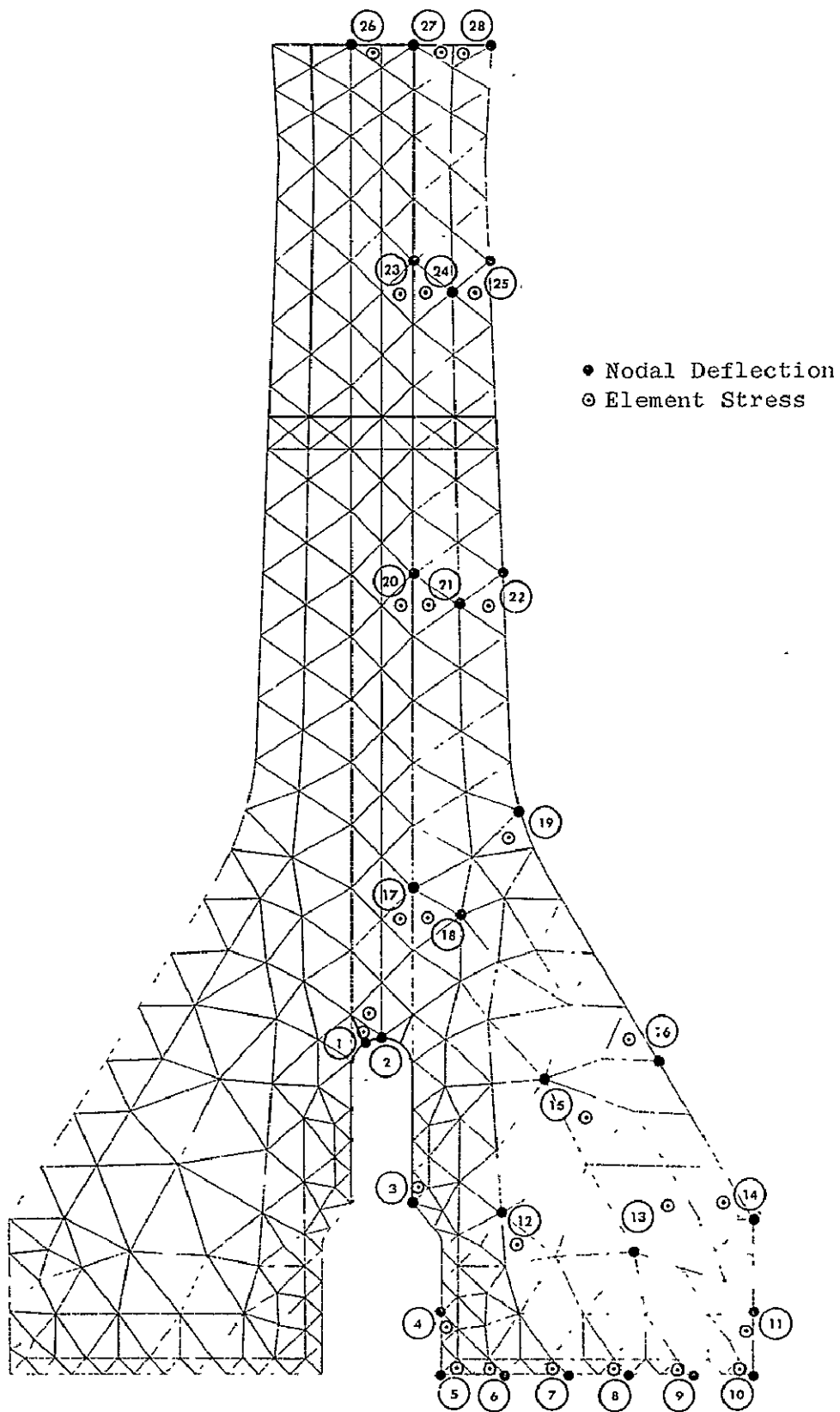


Figure 59. Improved (High Rib) Design Disk Stress and Deflection Locations.

Table XXIV. Improved (High Rib) Design Disk Stress and Deflection Distribution at Maximum Climb Conditions.

Location	Radial Stress		Tangential Stress		Radial Deflection	
	MPa	ksi	MPa	ksi	mm	in.
1	-	-	-	-	-	-
2	41	6	-	-	1.24	0.049
3	83	12	-	-	1.27	0.050
4	152	22	717	104	0.97	0.038
5	117	17	752	109	0.89	0.035
6	41	6	717	104	0.91	0.036
7	14	2	724	105	0.89	0.035
8	7	1	724	105	0.89	0.035
9	7	1	717	104	0.89	0.034
10	7	1	703	102	0.86	0.034
11	41	6	655	95	0.91	0.036
12	165	24	641	93	1.07	0.042
13	117	17	565	82	0.99	0.039
14	69	10	524	76	1.02	0.040
15	193	28	545	79	1.19	0.047
16	193	28	483	70	1.17	0.046
17	179	26	-	-	1.42	0.056
18	352	51	531	77	1.40	0.055
19	565	82	579	84	1.50	0.059
20	296	43	-	-	1.83	0.072
21	455	66	496	72	1.78	0.070
22	462	67	503	73	1.83	0.072
23	248	36	-	-	2.24	0.088
24	386	56	434	63	2.21	0.087
25	393	57	434	63	2.24	0.088
26	131	19	-	-	2.54	0.100
27	296	43	269	39	2.54	0.100
28	421	61	524	76	2.54	0.100

Table XXV. Improved (High Rib) Design Disk Stress and Deflection Distribution at Thrust Reverse Conditions.

Location	Radial Stress		Tangential Stress		Radial Deflection	
	MPa	ksi	MPa	ksi	mm	in.
1	34	5	-	-	0.76	0.030
2	69	10	-	-	0.76	0.030
3	159	23	586	85	0.66	0.026
4	152	22	676	98	0.61	0.024
5	124	18	710	103	0.58	0.023
6	41	6	683	99	0.58	0.023
7	14	2	683	99	0.58	0.023
8	7	1	689	100	0.58	0.023
9	7	1	683	99	0.56	0.022
10	7	1	676	98	0.56	0.022
11	34	5	627	91	0.58	0.023
12	159	23	600	87	0.66	0.026
13	117	17	531	77	0.61	0.024
14	69	10	496	72	0.61	0.024
15	179	26	510	74	0.71	0.028
16	193	28	469	68	0.71	0.028
17	159	23	-	-	0.86	0.034
18	331	48	524	76	0.84	0.033
19	538	78	572	83	0.89	0.035
20	276	40	-	-	1.07	0.042
21	434	63	503	73	1.07	0.042
22	455	66	510	74	1.09	0.043
23	241	35	-	-	1.30	0.051
24	386	56	462	67	1.27	0.050
25	393	57	462	67	1.30	0.051
26	131	19	-	-	1.45	0.057
27	310	45	331	48	1.45	0.057
28	331	48	352	51	1.47	0.058

Using the weight specific fuel consumption (SFC) derivative for an average DC10-30 aircraft flight, this extra weight translates into an increase in installed SFC of 0.29 percent. However, this value is offset by several other factors. Figure 60 shows a comparison between a twin-disk system with bore entry of the blade cooling air and an inducer cooling air entry system, for an advanced commercial turbofan engine. The inducer system concept brings the cooling air up to near wheel speed by use of turning vanes and then allows it to enter the disk through holes near the rim region. Although the delta SFC's shown are not directly applicable to the CF6-50 engine, they serve to illustrate that overall system gains are possible using blade cooling air entry at the bore of a turbine disk. An additional benefit derived from the weight required for a redundant disk design is the improvement in the life/burst performance of the system.

To verify the redundant design criteria, a plastic analysis was performed for the Design Disk using the PLADI computer program. The PLADI program uses a nonlinear stress-strain curve along with a set of finite difference equations for the model. For the elastic case, the method is direct, requiring only a single sweep through the equations to determine deflections and stresses. For the plastic case, the nonlinearities of the problem prevent a direct solution, and an iterative procedure is used to converge to true solutions on the stress-strain curve. The resulting stress distributions for the failed configuration are shown in Figure 61 for both the elastic case (assumed continued linearity of stress-strain) and the plastic case (using the appropriate stress-strain curve). As can be seen, the stress redistribution due to plastic effects drops the maximum stress value. This redistribution can be viewed as either safety margin in the design or extra weight that could be removed.

#### D. Fail-Safe Capability

An evaluation was made of the fail-safe capability of the Design Disk should one of the half-disks fail due to propagation of a critical crack from the base to the rim. The fundamental benefit of employing the Multidisk concept in the Design Disk is its structure redundancy. If one of the coupled disks would fail (i.e., sustain a bore-to-rim through crack), the remaining disk would be capable of carrying the cracked disk and preventing the release of any large disk fragments. To do this, it would be necessary for the integral ribs between disks to be able to transfer the load carried by the failed disk to the remaining disk. An analysis of this transfer capability must also account for the impulsive nature of the loading caused by the almost instantaneous breakthrough of a critical crack.

Three theories were used to analyze this problem. These are summarized in Figure 62. The ribs are assumed to act as cantilever beams fixed to the uncracked disk and subjected to end loads due to the failure of the companion disk. For this part of the analyses, it is assumed that once the load is transferred to the sound disk, it can be supported. Thus the main problem becomes: will the ribs be able to hold the failed disk to the unfailed one? Each of the three theories assumed that the rib will be able to absorb a certain strain

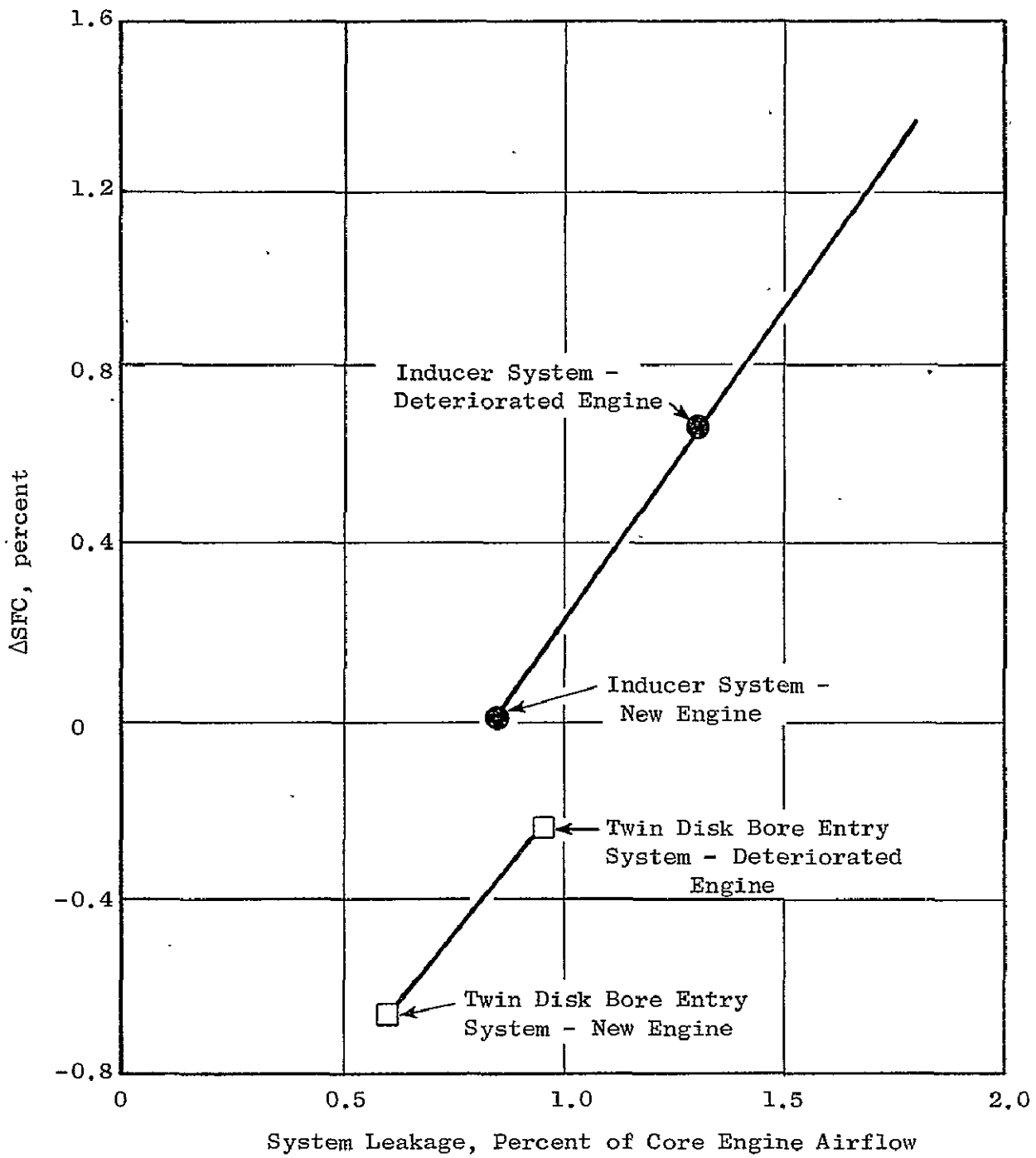


Figure 60. Blade Cooling Air System Comparison - Bore Entry Versus Inducer.

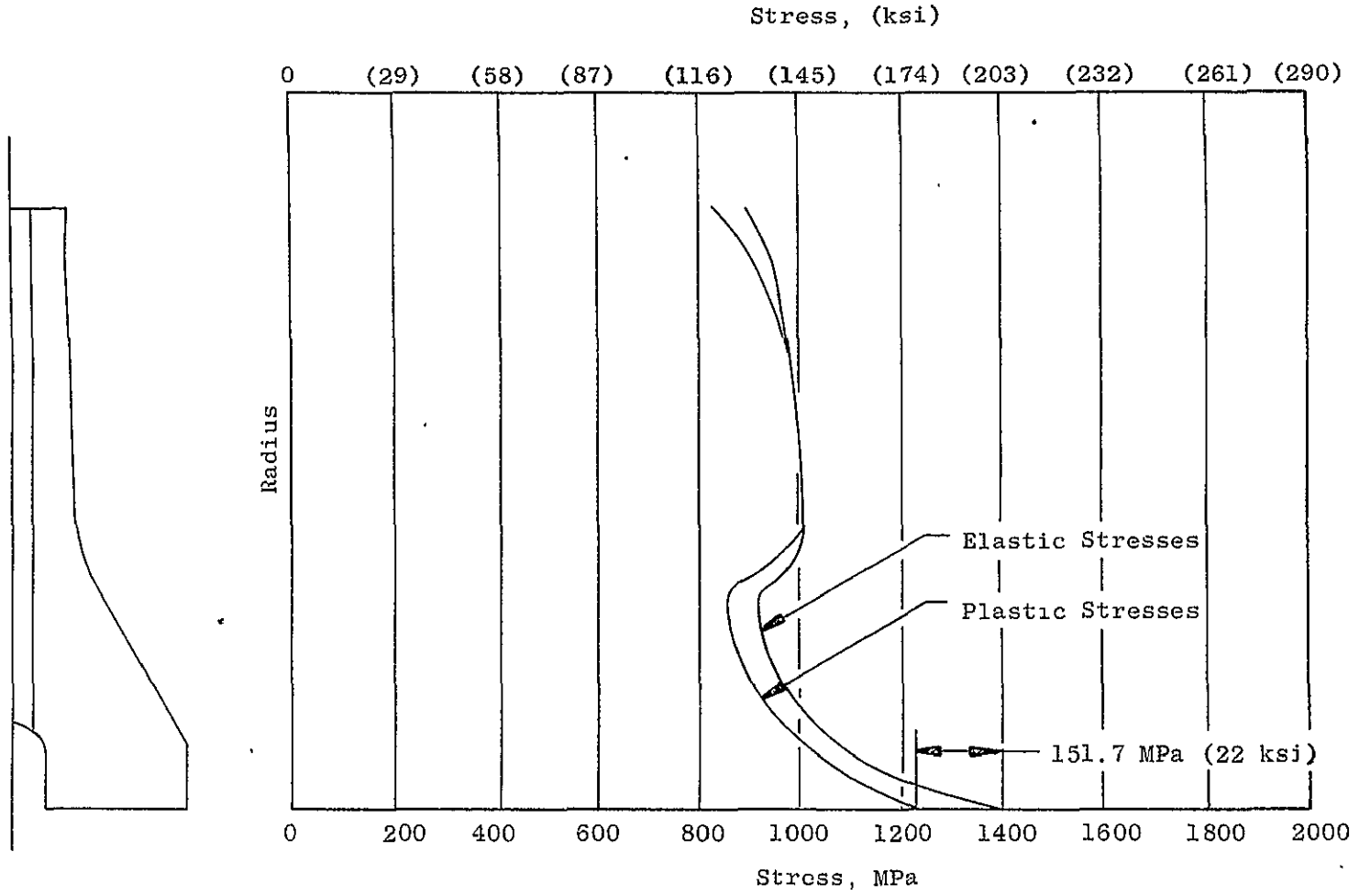
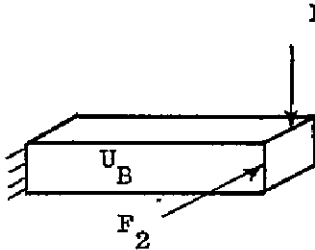
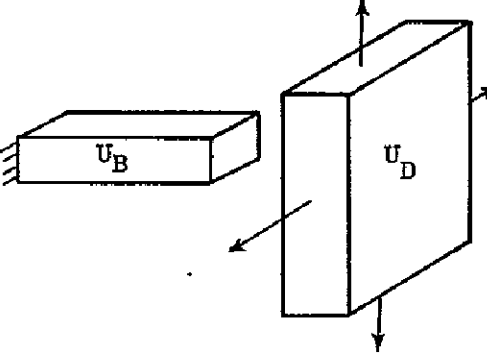
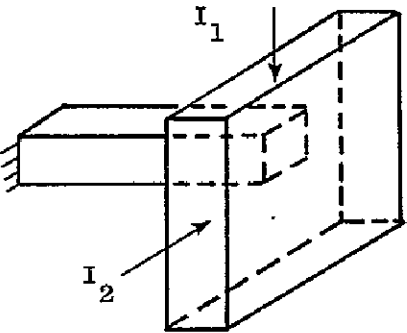


Figure 61. Design Disk Tangential Stress Distribution in Good Half with One Half Failed.

<p><u>Theory</u> Strain Energy in Beam Due to Applied Loads</p>		<p><u>Energy</u> <math>U_B</math></p>	<p><u>Criteria</u> ? <math>U_B \cong U_A</math></p>	<p><u>Result (Low Rib)</u> No Failure <math>\mu = 1.37</math></p>
<p>Strain Energy in Beam Equals Strain Energy in Disk Segment</p>		<p><math>U_B = U_D</math></p>	<p>? <math>U_B \cong U_A</math></p>	<p>No Failure <math>\mu = 25</math></p>
<p>KE in Disk Segment Due to Impulse Equals Strain Energy in Beam</p>		<p><math>U_B = KE_D</math></p>	<p>? <math>U_B \cong U_A</math></p>	<p>3 Ribs Failed</p>

KE = Kinetic Energy

$U_A$  = Energy Absorption Capability of Beam

$\mu$  = Ratio of Energy Input to  $U_A$

$U_B$  = Strain Energy in Beam

$U_D$  = Strain Energy in Disk

Note: Benefits of High Rate Loading Have Not Been Included, (i.e.,  $U_A$  is Conservative).

Figure 62. Rib Energy Calculation Methods.

ORIGINAL PAGE IS  
OF POOR QUALITY

energy as determined by the area under a uniaxial stress-strain curve at the 811° K (1000° F) selected temperature. (This follows the Mises-Hencky theory of failure under complex stress states.) If this strain energy is exceeded, the rib will fail. The theories differ in respect to how the beam (rib) strain energy is obtained.

In the first theory, (Figure 62) the beam energy ( $U_B$ ) is calculated from the linear elastic strain energy equations for a cantilever subjected to end loads. The loads are determined as the average radial and tangential forces in the failed disk prior to failure. Upon failure these forces are suddenly applied to the ribs. A computer analysis shows that the first rib away from the failure line absorbs 90 percent of the load. Roark in Reference 3 has indicated that suddenly applied loads result in twice the stress and deflection as statically applied loads, and these factors are included. (Note that the beneficial yield strength increases of impact loading have not been added in calculating  $U_A$ , the absorption capability, which introduces some conservatism). Comparing  $U_A$  to  $U_B$  shows that more energy can be absorbed than is input, so that no failure of a rib is expected, and the fail-safe criterion is met.

In the second theory, it is hypothesized that the strain energy in the beam is derived from the strain energy in the disk segment ( $U_D$ ) associated with it.  $U_D$  is calculated for the stress state in the disk at maximum conditions just prior to failure and equated to  $U_B$ . A comparison to  $U_A$  again shows no failure but indicates a much larger margin. In the first theory, essentially the entire disk energy is transmitted into one rib, while in the second theory, each rib is responsible for only a portion of the total disk energy.

The third theory is based on an analysis presented by Symonds and Bodner (Reference 4). Here the mass of the associated disk segment is considered to act as a mass on the end of a cantilever subjected to impulsive loading. The impulses are determined by assuming that the forces are applied linearly from zero to maximum in the time it takes for a crack to propagate from the bore to the rim (approximately  $1.7 \times 10^{-4}$  seconds). The kinetic energy imparted to the beam-mass system is then  $I^2/2M$ , where  $M$  is the mass of the disk segment and  $I$  is the impulse. The energy is equated to  $U_B$ . Comparison to  $U_A$  shows that one beam cannot absorb all of the kinetic energy; however, it will absorb the energy  $U_A$ . Hence, it is found that if 3 of the 80 beams (ribs) failed, all of the kinetic energy would be absorbed. Since the rest of the ribs remain intact, the fail-safe criterion is again essentially met.

#### E. Design Disk Life

The development of a new disk geometry necessitated reconsideration of critical area and defect pattern definitions relative to cyclic life and fracture considerations. A study of high stress and temperature areas and detailed investigation of stress raisers led to the identification of the following five regions as life-limiting areas:

- Bore
- Slot bottom
- Bolt hole
- Aft rabbet radius
- Rib-disk intersection

These critical locations are depicted in Figures 62 and 63.

### 1. Low Cycle Fatigue Life

Crack initiation (LCF) life for the Design Disk was calculated for the critical locations identified above.

The Design Disk geometric dissimilarities compared to the Standard and Advanced Standard Disks must be considered in assessing the relative life values.

Table XXVI summarizes the Design Disk results and compare them to previous calculations for the Standard and Advanced Standard Disks.

It was assumed that stress concentrations and distributions for the slot bottom, bolt hole, and rabbet are the same as for the Standard Disk. Actual stresses were scaled from the ROTOR runs for the Design Disk.

The Design Disk is superior in LCF life in every case, since the stresses are below those of either the Standard or Advanced Standard Disk.

### 2. Residual Life

Crack propagation lives were calculated using the methods described in Section IIB.2.

Figures 63 and 64 illustrate the assumed defect shape and locations used in the residual life studies. Figures 63 and 64(a) shows a bore defect similar to that used in the Standard and Advanced Standard Disks. A defect in this location would not produce an unstable failure in the Design Disk. Figures 63 and 64(b) show slot bottom and bolt hole defects in the same locations as those analyzed for the Standard and Advanced Standard Disks and producing identical fragments; based on test cell experience (Fragments D and E, Figure 64(b)). An additional defect is shown at the aft rabbet radius in Figure 64(b). This area was not analyzed on the Standard and Advanced Standard Disks due to the low-energy fragment patterns which would result from a failure in this location. However, on the Design Disk, the removal of the possibility of high-energy disk section fragments (Fragments A, B, and C, Figure 24) necessitated the selection of another fragment pattern for energy calculations. This latter fragment pattern consists of three post sections and the four adjacent blades and is identified as Pattern "F".

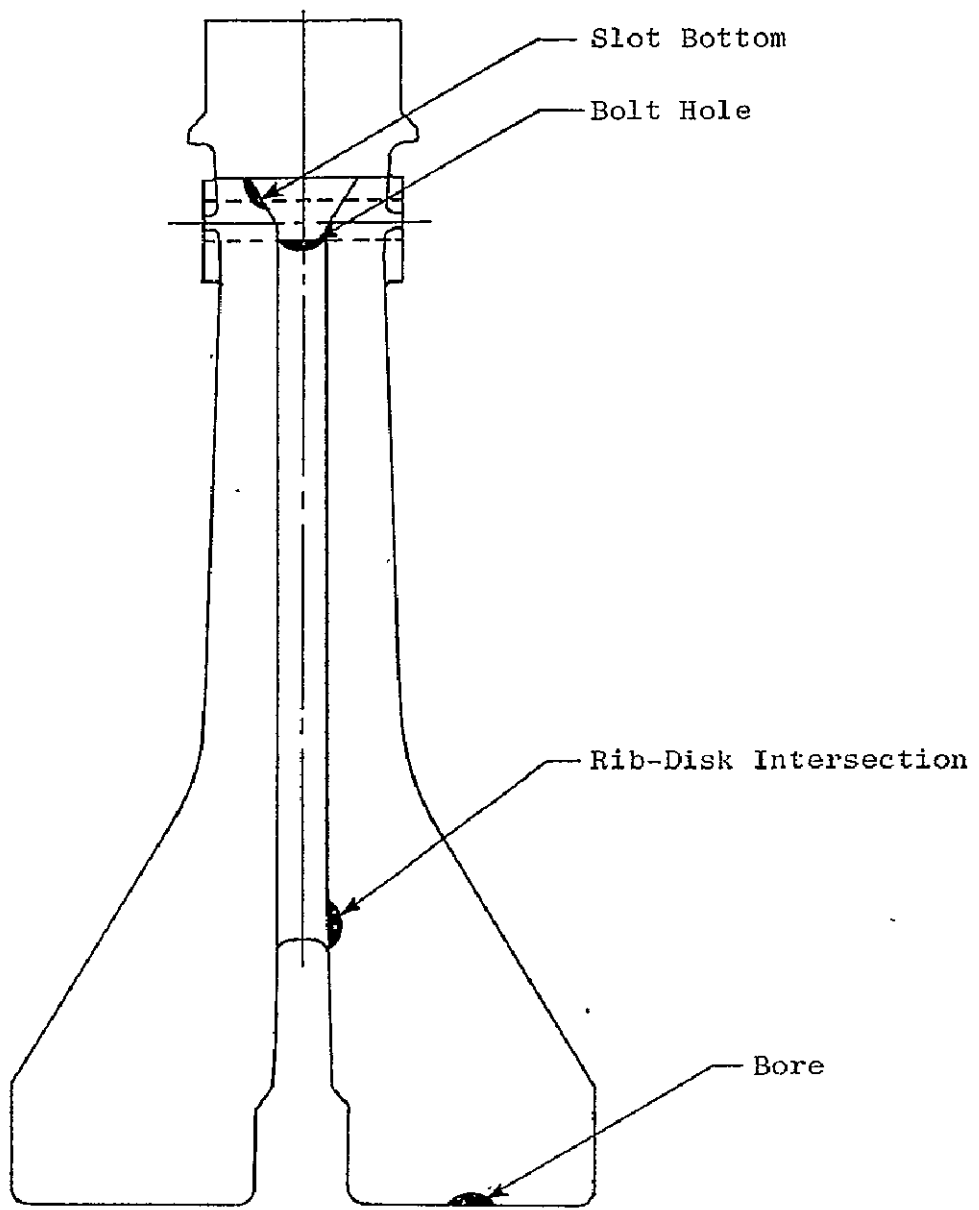
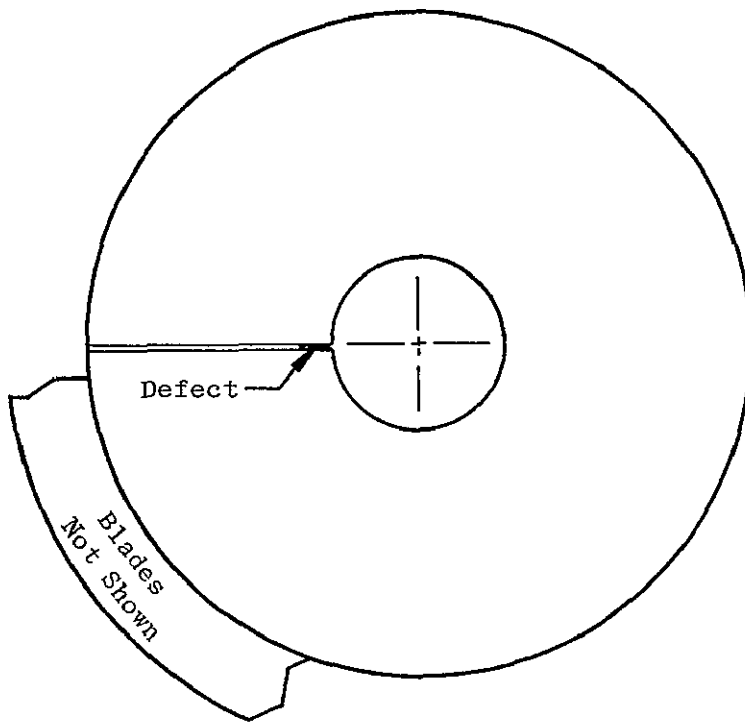
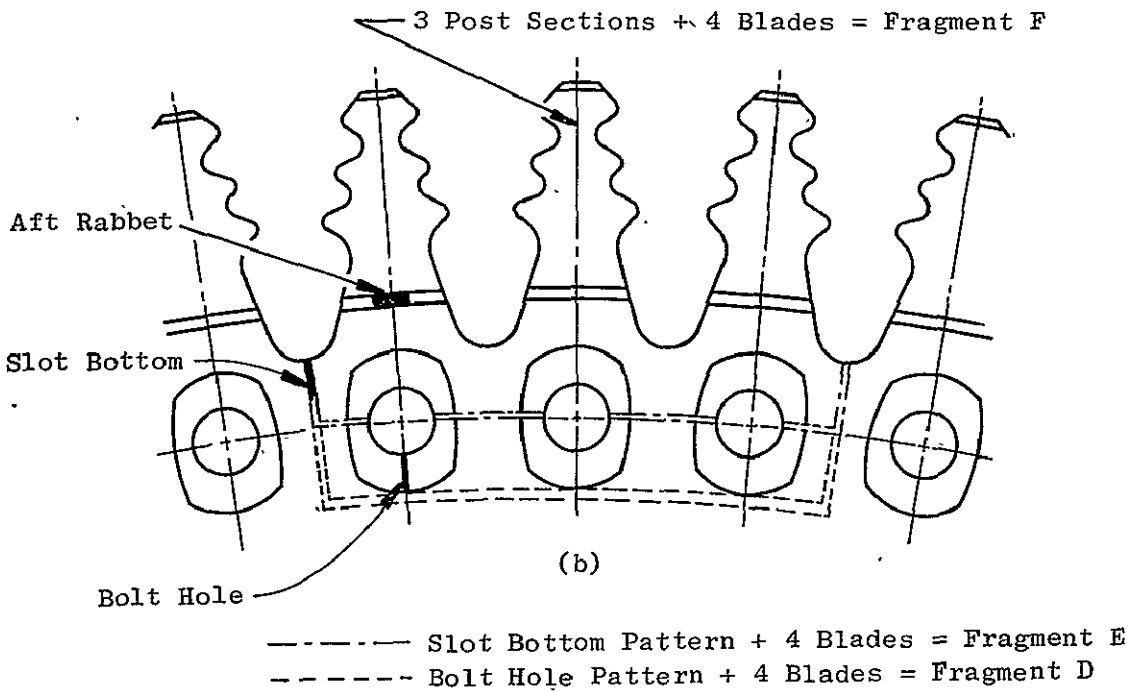


Figure 63. Design Disk Critical Locations.



(a)



(b)

Figure 64. Design Disk Critical Locations and Fragment Patterns.

Table XXVI. Low Cycle Fatigue Comparison.

(Entries in Cycles)

Location	Standard Disk (IN 718)	Advanced Standard Disk (René 95)	Design Disk (René 95)
Bore	63,000	∞	∞
Slot Bottom	$2.6 \times 10^5$	∞	∞
Bolt Hole	$4.1 \times 10^6$	∞	∞
Rabbit	-	-	∞
Rib-Disk*	-	-	∞

Table XXVII. Initial Defect Residual Life Comparison.

(Entries in Cycles)

Location	Standard Disk (IN 718)	Advanced Standard Disk (René 95)	Design Disk (René 95)
Bore	611	662	1,564
Slot Bottom	380	1,155	1,928
Bolt Hole	1,809	7,161	34,026
Rabbit	-	-	19,243
Rib-Disk*	-	-	1,673

Table XXVIII. Burst Speed Comparison.

	Burst Speed rpm	% of Maximum N <sub>2</sub> (N <sub>2</sub> = 10,613 rpm)
Standard Disk	13,345	126
Advanced Standard Disk	14,184	134
Design Disk	15,884	149

\* Rib-disk intersection region (see Figure 63).

Table XXVII summarizes the Design Disk results and compares them to the previous calculations for the Standard and Advanced Standard Disks. The Design Disk is superior to the Standard and Advanced Standard Disks in propagation results in the bore and bolt hole regions, where substantial improvement is shown. The critical areas of the Design Disk are the bore and the edges of the air passage (rib-disk intersection) in the bore region. Since neither the Standard or Advanced Standard Disks have this latter feature, no comparison is readily made.

It should be reemphasized that "failures" in the propagation sense would not result in catastrophic failure of the disk because of the inherent design features of the redundant Design Disk.

The life-limiting area of the Design Disk was identified as the rib-disk intersection (air passage edge) near the bore, and is attributed to the high stress and local stress concentration. Several design configurations and analyses were carried out relevant to extending the life in this area. The original design (schematically illustrated in Figure 65 as the "previous rib") used a circular fillet at the rib-disk interface. Based on the correlations at stress concentration factor and geometry shown in Figures 68 and 69 of Reference 5, a stress concentration factor ( $K_T$ ) of 1.45 was assumed to be operative. The life analysis resulted in a residual life in the presence of the assumed defect for rib-disk area of 1177 cycles. A change in design to the "high rib" configuration of Figure 65 was investigated and resulted in lowered nominal stresses in this area and increased residual life to 2101 cycles. A detailed finite element model of the fillet region was undertaken to study the effects of a parabolic fillet contour as suggested in Reference 5. The model of the circular and parabolic contours is illustrated in Figure 66. This analysis revealed that a better estimate of  $K_T$ , the stress concentration factor, was  $K_T = 1.9$  for the circular fillet and  $K_T = 1.6$  for the parabolic fillet. These values imply that the Reference 5 cases were not appropriate approximations to this problem. Residual lives were again calculated for the "high rib" design. Lives of 506 cycles for the circular fillet and 1673 cycles for the parabolic fillet were obtained. The final Design Disk employs the parabolic fillet and the high rib; hence, the residual life of this improved design is listed in Table XXVII.

## F. Design Disk Failure

### 1. Burst Speed

The burst speed for the Design Disk was computed (using the techniques of Section IIC.1) to be 15,884 rpm, or 149 percent of the CF6-60 hot day takeoff speed of 10,613 rpm. A comparison of burst speeds for the Standard, Advanced Standard, and Design Disks is shown in Table XXVIII.

### 2. Fragment Patterns and Energies

Based on the analysis and assumptions described below, the fragment patterns depicted in Figure 64(b) were assessed as principal fracture paths.

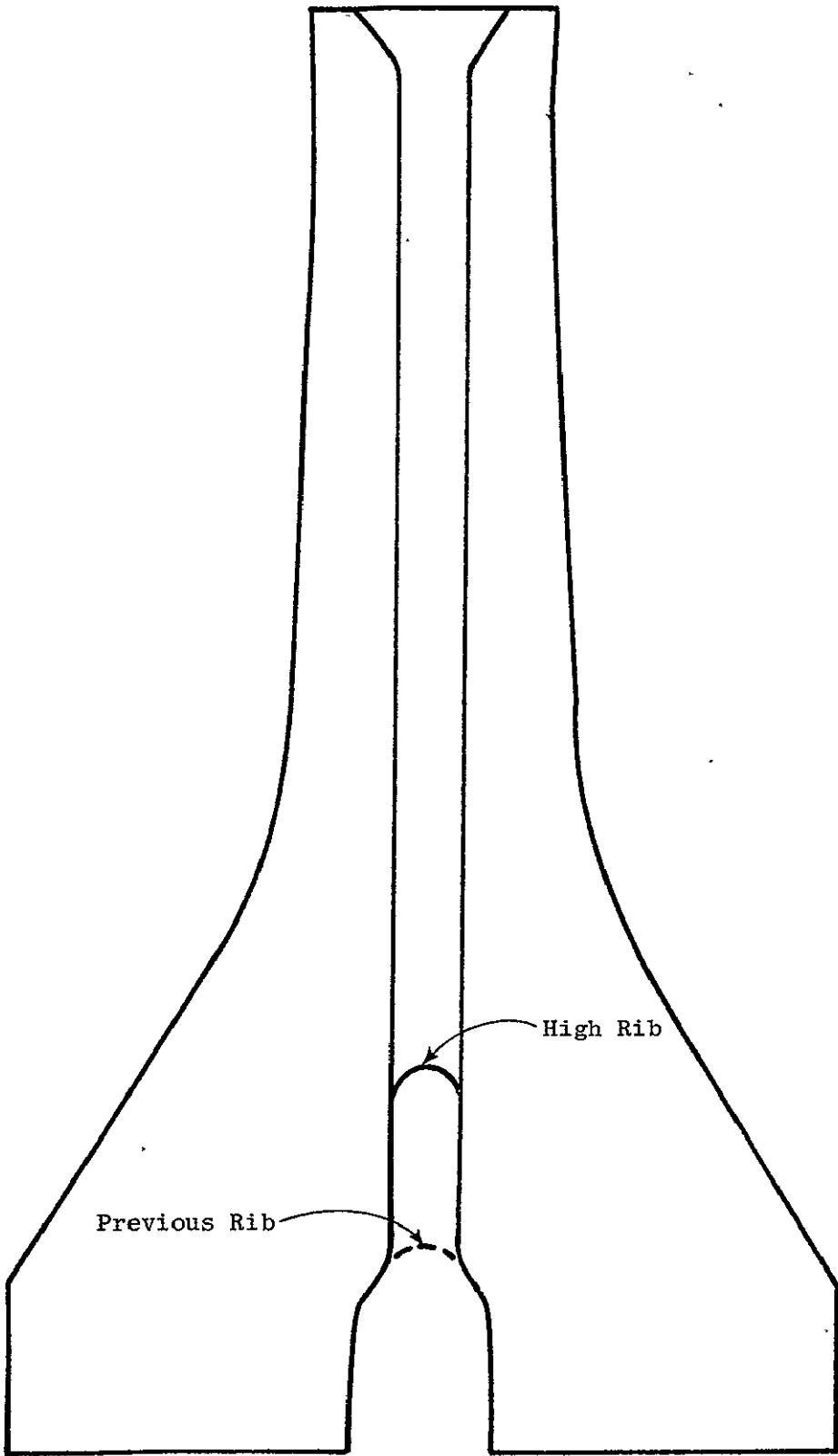


Figure 65. Design Disk High Rib Design.

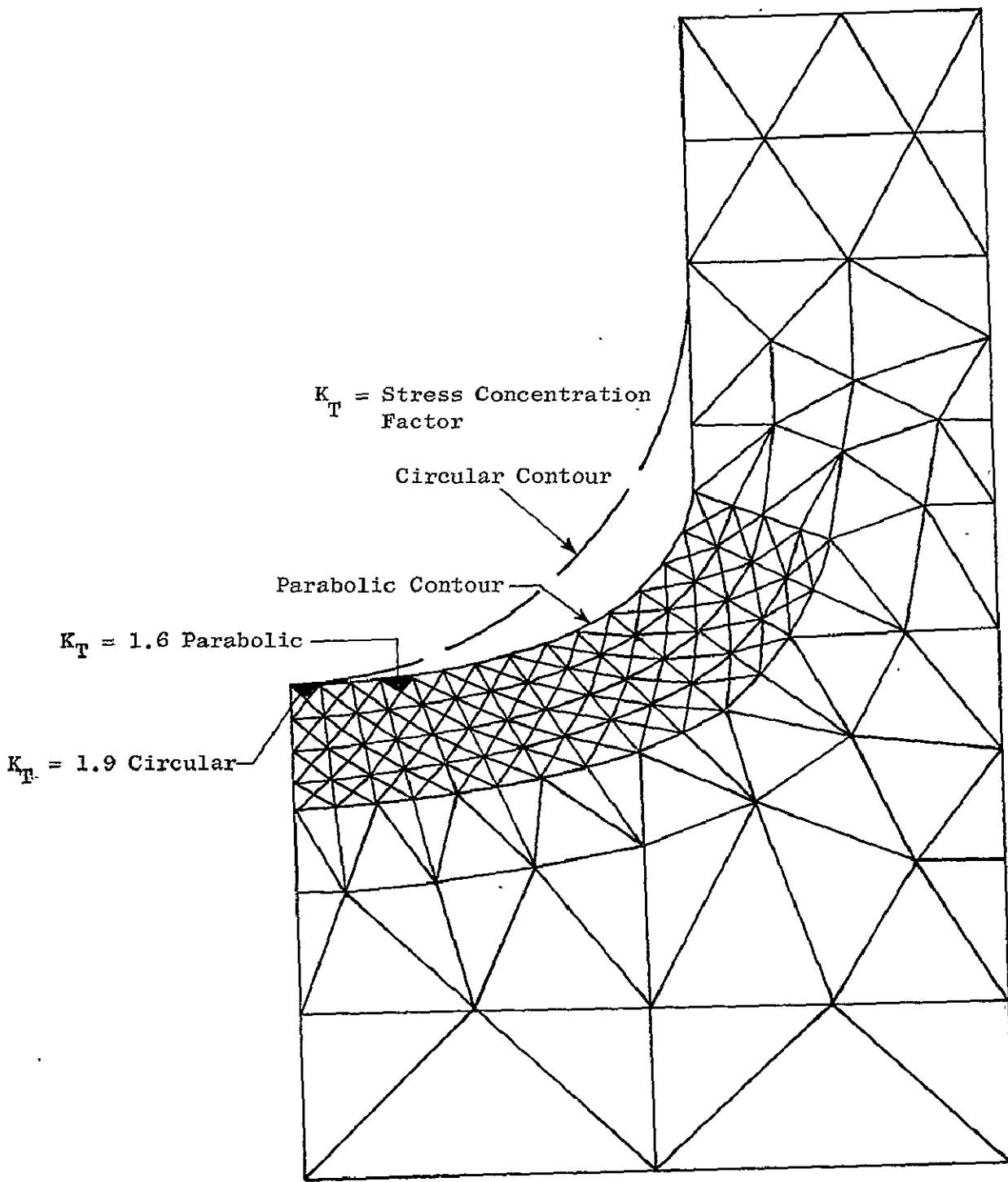


Figure 66. Finite Element Model of Rib-Disk Intersection Fillet.

- Fragments D and E: Posts and blades plus part of the disk. Result from cracks in the bolt hole or slot bottom regions.
- Fragment F: Posts and blades only. Results from crack-through of rabbet radii.

Based on previous analyses (Section II B.20), each occurrence of fragmentation would include three posts and four blades.

Two fundamental assumptions influenced these results:

1. Radial cracks would not propagate through the ribs.
2. A total loss of load-carrying capability (i.e., failure) of one disk could be tolerated by the remaining unfailed disk to the extent that the two disks or portions thereof would not separate from one another.

The first assumption requires test support and detailed analytic verification. The second assumption is reasonable based on preliminary calculations (Section II B.4).

Per the assumptions, critical crack growth from the bore to the rim would not result in fragments. Similarly, failures from cracks in the rib-disk interface regions and a bolt hole or slot bottom to bore crack would not produce fragments.

A rabbet radius crack, driven by radial stresses, would result in the loss of a post and its associated blades. As in previous studies, this would cause the secondary loss of two more posts and two more blades.

Bolt hole cracks originating at Point 1 in Figure 67 would be driven by radial stresses that exist in both disks and the rib; hence, propagation would proceed through both disks and rib until high stress caused Fragment E to tear out. Cracks from Point 2 in Figure 67 could proceed in a similar manner, since radial and tangential stresses are nearly equal. The possibility of Fragment D, therefore, must be allowed. By the same reasoning, cracks in the slot bottom might also result in a Fragment D type failure.

Thus, fragment generation would be confined to the bolt hole-slot bottom region and would result in similar small fragments consisting of blades and post sections.

Fragment energy values were calculated for the (using methods in Section II B.2) fragments depicted in Figures 64 and 67. The results are tabulated and compared to previous results for the Standard and Advanced Standard Disks in Table XXIX.

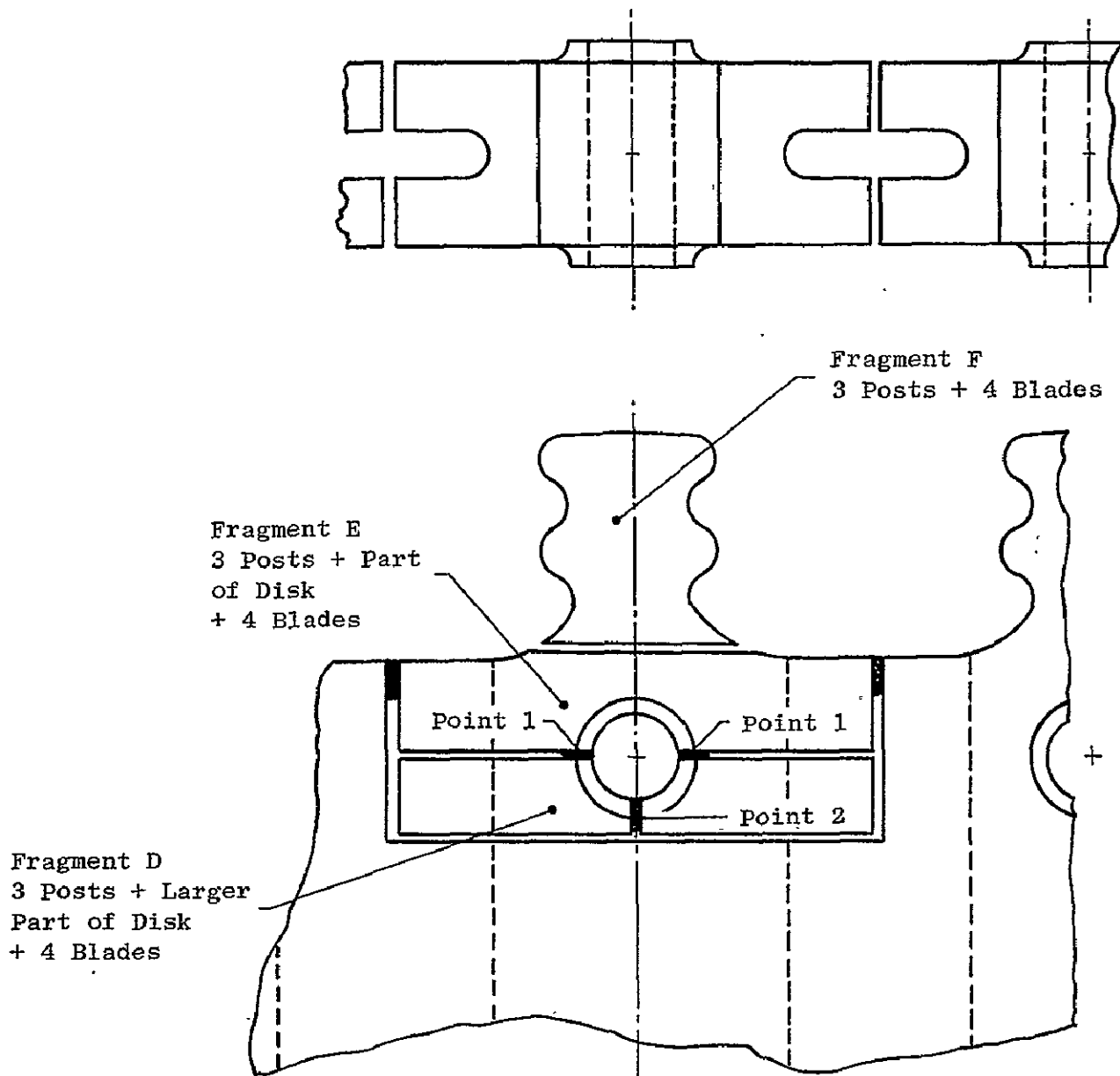


Figure 67. Design Disk Fragment Patterns.

Table XXIX. Fragment Energy Comparison: Standard Disk versus Advanced Standard Disk versus Design Disk.

Kinetic Energy Available For Penetration

Fragment Type	Standard Disk		Advanced Standard Disk		Design Disk	
	Rotational	Translational	Rotational	Translational	Rotational	Translational
	Nm (ft-lb)	Nm (ft-lb)	Nm (ft-lb)	Nm (ft-lb)	Nm (ft-lb)	Nm (ft-lb)
A (90°)	41,969 (30,955)	837,387 (617,625)	42,167 (31,101)	839,425 (619,128)	0 (0)	0 (0)
B (180°)	370,997 (273,633)	1,387,718 (1,023,528)	372,751 (274,927)	1,390,436 (1,025,533)	0 (0)	0 (0)
C (120°)	115,764 (85,383)	1,056,712 (779,391)	116,312 (85,787)	1,059,147 (781,187)	0 (0)	0 (0)
D	- -	110,290 (81,346)	- -	110,450 (81,464)	- -	115,967 (85,533)
E	- -	107,214 (79,077)	- -	107,348 (79,176)	- -	111,225 (82,035)
F	- -	- -	- -	- -	- -	103,911 (76,641)

## SECTION VIII

### RESULTS AND CONCLUSIONS

A new and novel disk design, an integral twin multidisk with bore entry of rotor cooling air, has been designed, analyzed, and compared to the existing high pressure turbine Stage 1 disk in the CF6-50 engine. The disk was found to possess infinite low cycle fatigue life and a 300 percent improvement in propagation life from a buried semielliptical defect of 26.35 x 2.12 mm (0.250 x 0.083 in.) dimensions. The energy of released fragments upon disk burst was decreased by an order of magnitude as a direct result of the design for redundancy feature of the disk. Additionally, the disk burst speed margin was increased from 126 percent for the existing disk to 149 percent for the integral multidisk. However, these life improvements resulted in a Design Disk weight that was 44.5 Kg (98 lb) heavier than the Standard Disk, with a projected increase in installed SFC of 0.29 percent.

The redundancy feature of the integral multidisk design offers the potential for increased life and safety in the operation of jet engines.

## SECTION IX

### RECOMMENDATIONS

Due to the potential advantages inherent in a redundant disk it is recommended that testing be performed to verify the assumptions made in the integral twin multidisk design. This could be accomplished on subscale model tests, primarily to ascertain the likelihood of crack propagation through an integral rib and to assess the level of impact loading on a disk rib in the event of disk failure. Then, if any deficiencies in design assumptions were found, the integral multidisk would be redesigned and subjected to full-scale disk tests. These could include cyclic spin pit testing to verify low cycle fatigue life and propagation life/burst characteristics of an initially flawed disk.

## REFERENCES

1. Wilson, E.L., "Structural Analysis of Axisymmetric Solids", AIAA Journal, Volume 3, No. 12, December 1965.
2. Kennedy, A.J., "Processes of Creep and Fatigue in Metals", John Wiley, New York, 1963.
3. Roark, R.J., "Formulas For Stress and Strain", McGraw-Hill, 1965.
4. Symonds, P.S., and Bodner, S.R., "Experimented and Theoretical Investigation of the Plastic Deformation of Cantilever Beams Subjected to Impulsive Loading, Journal of Applied Mechanics, ASME, 62-WA-63.
5. Peterson, R.E., "Stress Concentration Factors", John Wiley, New York, 1974.